Low Dimensional Polariton Systems in Subwavelength-Grating Based Microcavities

by

Bo Zhang

A dissertation submitted in partial fulfillment
of the requirements for the degree of
Doctor of Philosophy
(Physics)
in the University of Michigan
2015

Doctoral Committee:

Assistant Professor Hui Deng, Chair
Professor Stephen R. Forrest
Professor Cagliyan Kurdak
Associate Professor Jennifer P. Ogilvie
Assistant Professor Kai Sun

To my loving parents, Siping Zhang and Xiuli Li

ACKNOWLEDGEMENTS

Firstly, I must acknowledge my adviser, Assistant Professor Hui Deng, for giving me this wonderful opportunity to conduct research in our group. I thank her for her continuous mentorship, which helps me go through the past five and half years in our group. I am very grateful for her constant patience with me, especially for my first three years in the group when none of my devices worked and none of the positive results were produced. Those were difficult times for me as well as for her. I thank her for enduring this hard starting period of the research life with me. I would also like to thank her for creating opportunities to collaborate with other researchers, particularly for my projects. With Hui's help, I had the opportunity to visit our German collaborators. It was such an eye opening experience for my academic research. In addition, many thanks for her continuous financial support which enables me to fully focus on the research.

I would also like to thank my committee members: Professor Stephen Forrest, Professor Cagliyan Kurdak, Associate Professor Jennifer Ogilvie and Assistant Professor Kai Sun, for sparing their time to serve on my committee and make very useful suggestions on the this dissertation.

In the early stage of my Ph.D. research, I spent much time working in the clean room. I would like to thank Dr. Nadine Wang who was the first person introducing me to the clean room. She helped me learn the equipments and often introduced me to the right person to discuss problems based on the requirements of my research.

Many thanks to Dr. Elizabeth Covington and Dr. Robert Nidetz, who were so nice to let me work with them when no one else offered help. Robert was also the person who taught me how to operate Raith150 for e-beam lithography, which was probably the most important tool to fabricate my device. I would also like to thank Dr. Chi-Sen Lee and Dr. Yi-Kuei Wu for sharing their work experience in the clean room which greatly helped me make my own devices. Also many many thanks to the other staff members at Lurie Nanofabrication Facility.

Members of the Deng group are great colleges to work with: Dr. Paul Bierdz, Lei Zhang, Tyler Hill, Zhaorong Wang, Seonghoon Kim, Gle Leung. I would especially like to thank Paul, as we were the founding members of the group and have been through some of the difficult times together. I thank him for being there listening to me and offering me advice when things don't work well in the lab. To Zhaorong and Seonghoon who will carry on the polariton research in our group, I wish you the best!

Thank you also goes to my German research collaborators at University of Wuerzburg as well. I thank Dr. Christian Schneider's kind host while I was visiting. I thank Dr. Sven Hoefling and Professor. Martin Kamp's arrangement for the productive experiments at Wuerzburg. I am also very grateful to them for providing the high-quality sample wafers, without which none of my experiments would be possible.

Many of my Ann Arbor friends also made this Ph.D. journey an enjoyable experience. Thank you to Langechuan Liu and Lina Zhao. We meet up almost every week. They always give me so much encouragement in research and life. They also gave me much advice on job seeking and career development. Thank you to Dr. Sarah Anderson as well. The football games, TV show watching and long walk around the neighborhood with you make the life at Michigan fun and memorable. Special

thanks to Dr. Yifan Zhang, who helped recommend me for the wonderful internship opportunity. Yifan is also a very good friend since Day One here in graduate school. I would also like to thank Michelle Adan and Dr. Matthew Bales for their initiation of the job-searching group towards the end of Ph.D. life, also for their inclusion of me as an international student for many hang-out occasions. Thank you also goes to Chao Shen, Zhen Zhang and Ran Lu. They are very generous for offering comforts and conversations when my experiments do not go well in Randall. Many thanks to Hui Wang, for his constant support and encouragement throughout the years. And there are also many others I may have forgotten to mention over here.

At last but not least, I thank my parents, Siping Zhang and Xiuli Li, for their constant care, nurture and unconditional love. I would like to dedicate this thesis to my parents! This journey would not be possible without them!

TABLE OF CONTENTS

LIST OF FIGURES

Figure

CHAPTER I

Introduction

Exciton-polaritons are quasi-particles created due to the strong coupling between the semiconductor excitons and microcavity photons[1]. The matter components, excitons, feature rich interactions in semiconductor materials. Hence polaritons are good candidates for research on many body physics as well as non-linear phenomena. The major decay channel for polaritons is through the photon leakage which maintains the same energy and momentum. The measurement of these photons gives the direct information of the polariton systems. The photon component of the polaritons also enriches the system with physics of cavity quantum electrodynamics.

1.1 Two Dimensional (2D) Polariton System

As one of the important demonstration on macroscopic quantum phenomena and quantum many body physics in solid state materials, two dimensional (2D) polariton Bose-Einstein condensation (BEC) or polariton lasing has been realized and observed in many groups[2][3][4] for the past decade. Quantum degeneracy[5], 1st order[6] and 2nd order coherence[2][7][8] for this condensation/lasing have been observed. Superfluid properties along side the BEC of polariton system such as long-range transportation, vortices and Josephson oscillations[9] [10] [11] [12] have also been

achieved in relatively recent years.

Since the major decay channel for the polariton system is through the photon leakage which maintains the same energy and momentum, the measurement of these photons gives the direct information of the polariton system. By exploiting such property of the polariton systems, researches on the physics of cavity quantum electrodynamics have also been well developed both in theory[13] [14] [15] [16] and experiments [17] [18] [19].

Since polariton lasing is realized through the polariton BEC, the lasing mechanism is different from the traditional laser, where a population inversion is not required [20] [21]. Therefore polariton lasers normally have a relatively lower excitation threshold compared to the traditional semiconductor laser[22]. This promises the polariton system more device-orientated applications in addition to the scientific research. Many efforts have also been made towards a more attainable polariton laser with room temperature lasing or even electrically pumped devices. For instance, uitilizing the higher binding energies of excitons in GaN [23] [24] [25] [26] and organic semiconductor materials[27] [28] [29], polariton lasing at room temperature has been realized. Electrically pumped polariton lasers using GaAs as the active media have also been demonstrated in two groups[30] [31] in very recent years.

1.2 Lower Dimensional Polariton System

Two dimensional polariton systems have enabled people to conduct research on many remarkable physics phenomena as illustrated above. Yet many of the theoretically predicted applications of polariton systems have reached beyond two dimensional systems, such as matter-wave circuits/polariton circuits[32] [33] [34], novel

phases transition[35] [36], and lattice quantum simulators[37]. To realize these useful and promising applications, effective lower dimensional (0D or 1D) confinement, control and coupling are required.

Since a polariton consists of semiconductor excitons and cavity photons, one of the viable paths to control the polariton system is through the matter part. Mechanical potentials[38] [4], external electrical or magnetic fields[39] [40] [41], or even optical stark effects[42] for the semiconductor excitons have shown the energy tuning and local confinement abilities for a polariton system. Yet these experimental constructions for the polariton systems are far from effective as for the dimensionality control. Besides, these bulky external setups are hard to be incorporated at the level of single devices.

To have more effective polariton system controls and also avoid the complicated external field setups, we can also alter the systems from the cavity photon part. One direct and simple way to modify the photon components for the polariton system is using the optical pumping source. By using different pumping densities [43] and different pumping geometries[44] [45], locally trapped polaritons can be realized. However, these devices are still heavily relying on the external experimental equipment. Similar to controlling through exciton components, incorporating these optical schemes into a single device could be difficult.

Many experimental efforts have been invested in controlling the polariton system from the sample level. In particular, one popular way is by using different surface patterning[46] [47] [48] [49]. Effective confinement is realized by altering the cavity length with the surface metals. Instead of having the continuous dispersions in momentum space for traditional 2D polariton systems, energy gaps appear at certain critical points. Effective polariton lattices are successfully constructed and many of

the lattice physics rules are giving accurate explanations and predictions. Yet sharing the same issue with the method of using an optical pumping scheme, these devices are still using the traditional 2D systems. Accessing to an individual or isolated lower dimensional system, such as 0D and 1D, still remains challenging.

To be able to form these low dimensional polariton systems, one effective way is to embed a low-dimension aperture inside the sample before completion of the epitaxial growing [50] [51]. In this way, the polariton system is conveniently confined within the aperture. The signature discrete energy levels have been observed in these systems, which indicates effective lateral confinements. However, due to the intrinsic defects for the MBE re-growth, no polariton lasing or condensation have been observed from these samples.

In order to have the low dimensional systems and keep the polariton lasing / condensation, pillar etching used to be the most successful technique to modify the polariton systems[52] [53] [54] [55] [56]. 0D, 1D or even lattice systems with polariton lasing/condensation have been achieved. Since the sample mirrors are still using distributed Bragg reflector (DBR), it is normally several microns thick. Making these straight and tall pillars always requires long-time and accurately delivered plasma etching. The plasma bombardment is effective to sculpt the pillars yet it is damaging the active media − quantum well exciton layers as well. As a result, the exciton layer is not well protected. Besides, the energy detuning (energy difference between cavity photon and quantum well exciton) is highly location dependent. Single pillar or in-situ photon energy tuning is almost impossible due to the intrinsic limitations for all DBR based samples.

1.3 Sub-Wavelength Gratings-Based Polariton System

To overcome the limitations for all the DBR based samples, where in-situ photon tuning is impossible, and also be able to fulfill the purpose of effective low dimensional control in polariton systems, a new type of cavity which bases on mirrors utilizing sub-wavelength high contrast gratings is introduced and investigated in this thesis.

In comparison with the traditional polariton research using the thick DBR samples (several microns), the sub-wavelength gratings (SWG) are only a single thin layer (tens of nanometers) of alternatively matter-air periodic structure. Taking advantage of the high contrast of the refractive indices between air and semiconductor material, the SWG-mirrors are the same or even better quality as compared to the mirrors with DBR in terms of the reflectance and the range of the wavelenth giving high reflectivity. In addition, we can utilize the air gap below this single layer of gratings for the in-situ photon resonance tuning, since the cavity photon resonances have the one-to-one correlation with the air-gap distances. Besides, the in-plane asymmetric property of the grating structures will also add extra control for the polarization direction of the polaritons, which is another fundamental property for the light part of the systems. This type of high contrast grating (HCG) mirrors has been successfully implemented in the vertical cavity surface emitting lasers (VCSEL) [57] [58] [59] [60] [61] [62]. Many of the traits of the high contrast gratings found in these references are also beneficial for polariton research, such as resonance tunability, dimensionality control and high fabrication tolerance.

As for the low dimensional system control using the SWGs, it provides many advantages. Comparing with the surface patterning devices, we have the capability of constructing single 0D, 1D or even coupled systems directly by the gratings shape

definition in fabrication[63] [64]. We will be able to not only observe the coupling effects in lattice type structure similar to surface pattern device, but we will also still maintain the control for each individual 0D system which is impossible for the surface pattern systems. Compared to the aperture embedding samples and pillar etching samples, the active media of the exciton layer is well protected during the device fabrication since the etching is shorter and less intrusive. Besides, single polariton lasing was observed and demonstrated in this thesis.

Lastly, the SWG systems also enable us with many other properties of polaritons. Firstly, dispersion engineering can be fulfilled [65]. Since we have the flexibility to change the phase inside the cavity for photons emitted at different angles, different cavity photon resonances will appear from the device for corresponding in-plane wave-numbers. These features of SWG pose a potential for polariton dispersion engineering. Besides, the distinct coexistence of strong coupling and weak coupling in one device features bi-statbility [66]. Such properties also have the potential for spin researches [67] [68] [69] [70] in SWG microcavities for polaritons. In addition, the thin layer of SWG is also sensitive to mechanical tuning, such as small physical bending and vibration. It also has the potential to demonstrate optomechanical phenomena that theory has predicted [71].

1.4 Thesis Structure

In this thesis, I will first review the low dimensional quantum systems (Chapter II) and traditional 2D polariton research in DBR samples (Chapter III). Then I will introduce the sub-wavelength high contrast gratings, SWG/HCG, which includes the device design and fabrication (Chapter IV). Next, I will focus on a 0D polariton

system using the SWG cavity (Chapter V). The dispersion, signature energy discrete levels, unique polarization properties and the single-mode lasing phenomena will be demonstrated. Additional properties of the 0D device such as diamagnetic energy tuning and second order coherence will also be discussed (Chapter VI).Following the work of the 0D SWG polariton systems, I will also demonstrate some of my work in the coupled 0D systems and even 1D systems using SWG structures (Chapter VII). The potential engineering and dimensionality control will be illustrated. Lastly, some of the future work will be discussed (VIII).

CHAPTER II

Low Dimensional Quantum Systems

When the physics scales go down to micron- or even nano-meter realm, many new phenomena will emerge which can not be explained by using classical mechanics. As modern technology develops, many of the electronic and optical devices have gone down to these extremely small scales, thus have reached beyond the classical mechanics limit. Therefore we have entered into the quantum world. Quantum mechanics have provided fundamental framework and comprehension for physics at this regime. In this chapter, some basic quantum mechanics examples with low dimensions will be discussed.

2.1 One Dimensional Quantum Wells

2.1.1 One Dimensional Quantum Wells with Infinite Potential

One of the simplest examples that we can observe the quantum phenomena is by using the model of one dimensional quantum well. Assume there is a infinite potential quantum well as shown in the figure. The potential can be described using the following equations:

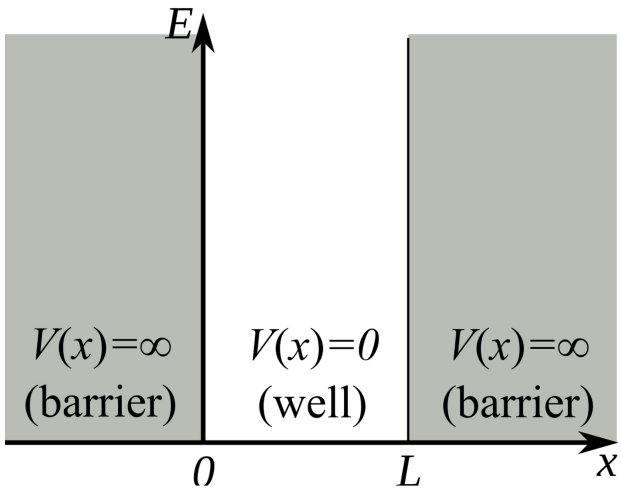

Figure 2.1: Potential diagram for a one dimensional quantum well

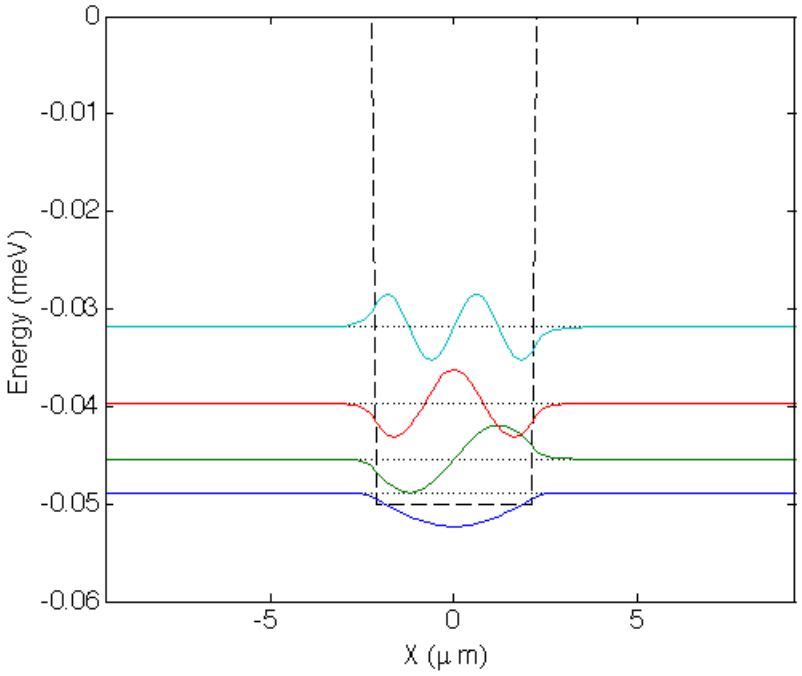

Figure 2.2: The first four energy levels and corresponding wave functions for a 1D finite potential well. The dashed line is indicating the potential height and position.

$$V(x) = \begin{cases} +\infty & x > L \\ 0 & 0 < x < L \\ +\infty & x < 0 \end{cases} \tag{2.1}$$

Use Schrodinger's equation for static states in this one dimensional case:

$$[-\frac{\hbar^2}{2m}\nabla^2 + V(x)]\Psi(x) = E\Psi(x) \tag{2.2}$$

By matching the continuous boundary conditions at $x = 0$ and $x = L$, we can simply find the analytical solutions for this 1D infinite quantum well problems:

$$E_n = \frac{n^2\pi^2\hbar^2}{8mL^2} \tag{2.3}$$

where n is the discretized energy level number and n is also an integer number. The corresponding wave functions for all these energy levels are shown in the following:

$$\Psi(x) = \begin{cases} 0 & x > L \\ \sqrt{\frac{2}{L}}sin(\frac{n\pi}{L}x) & 0 < x < L \\ 0 & x < 0 \end{cases} \tag{2.4}$$

Even though this is a simple quantum box case and is not a true reflection of real cases in the actual physical devices, it still provides useful in-depth understanding of

the scale trends. For example, if we take a look at Equation 2.3, the energy levels of the 1D quantum well, the energy levels' spacing for $n+1$ and n can be derived as:

$$\Delta E = \frac{\pi^2\hbar^2}{8mL^2}[(n+1)^2 - n^2] \tag{2.5}$$

$$\Delta E = \frac{\pi^2\hbar^2}{8mL^2}(2n+1) \tag{2.6}$$

So the energy levels' spacings have become larger as the energy level goes up, which we could easily observe in many of the real quantum devices.

Another important feature worth pointing out from the solution of this 1D quantum well (Equation 2.3) case is that, the energy levels' spacing has the inverse proportional relation with the quantum well dimension L. So as the dimension of the device decreases, the energy spacing of the energy levels will increase.

2.1.2 One Dimensional Quantum Well with Harmonic Potential

Another important and simple quantum well example is with harmonic potential. The potential shape is a parabolic function of the position x. It is also one of the few quantum systems which can have a simple and analytical solution.

Similar to the infinite quantum well solution, we apply the harmonic potential to Equation 2.2. The harmonic potential is with parabolic shape of $V(x) = \frac{1}{2}\hbar\omega^2 x^2$. The wavefuntion solutions are shown here:

$$\Psi(x) = \frac{1}{\sqrt{2^n n!}}(\frac{m\omega}{\pi\hbar})^{1/4} exp(-\frac{m\omega x^2}{2\hbar}) H_n(\sqrt{\frac{m\omega}{\hbar}}x), \quad where\, n = 1, 2, \ldots\ldots \tag{2.7}$$

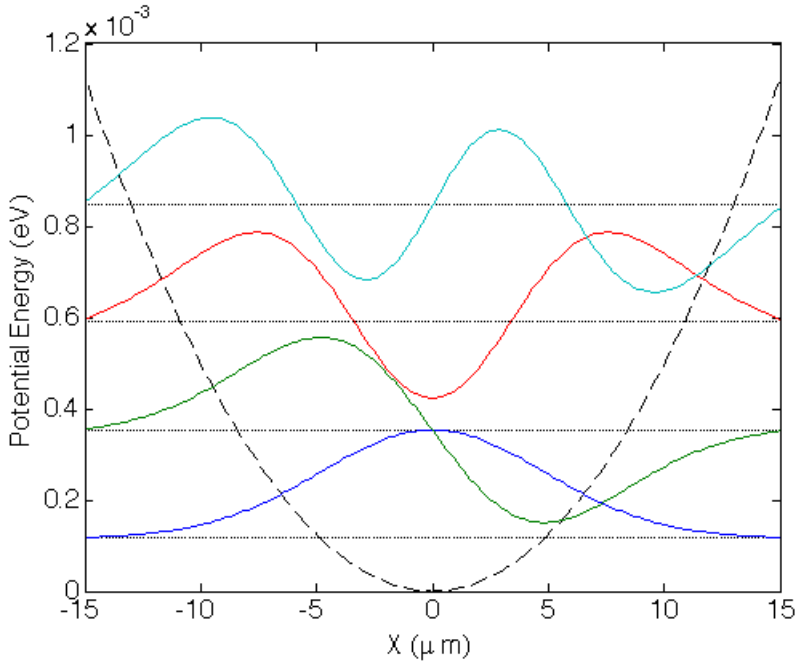

Figure 2.3: An example of quantum well with harmonic potential, energy and wavefuction solutions for the first four levels

The energy solutions are:

$$E_n = \hbar\omega(n + \frac{1}{2}),\ where\ n = 1, 2, \ldots \tag{2.8}$$

As can be seen from the energy solutions, the energy spacing is equal for the harmonic potential, which is $\hbar\omega$.

One example using harmonic potential is shown above in Figure 2.3. The harmonic potential trapped effective photon mass is 1.38×10^{-5} of electron mass, the harmonic potential is with $\hbar\omega = 22.5\mu eV$.

2.1.3 One Dimensional Quantum Well with Finite Potential

Continuing with the 1D quantum well case, the finite potential well problem has very similar potential structure. To make the problem slightly easier and solutions symmetric, I shift the potential to the left by $L/2$, but the width of the potential still maintains at L. The potential for this problem is shown in the following:

$$V(x) = \begin{cases} 0 & x > L/2 \\ -V_0 & -L/2 < x < L/2 \\ 0 & x < -L/2 \end{cases} \tag{2.9}$$

We can use the similar solving method by applying this potential to the Schrodinger's Equation 2.2 and applying to the continuous boundary conditions at $x = -L/2$ and $x = L/2$. We can not get analytical expression for the energy levels. However, we can use numerical method to get the solution for the energies. The wavefuntions for this potential well in three different regions without showing explicitly the values for the wave-number k (since it is dependent on the energy solution) are shown in the following:

$$V(x) = \begin{cases} \Psi_1(x) = Ce^{-\alpha x} + De^{\alpha x} & x > L/2 \\ \Psi_2(x) = Asin(kx) + Bcos(kx) & -L/2 < x < L/2 \\ \Psi_3(x) = Fe^{-\alpha x} + Ge^{\alpha x} & x < -L/2 \end{cases} \tag{2.10}$$

where α and wave number k are depending on the numerical solution for the energy and the coefficients A, B, C, D, F, G are dependent on the normalization.

One example using the finite quantum well wavefuntion solution is shown in the following figure. The parameters I am using are true reflection of the photons in an

actual optoelectronic device I will later discuss in the later chapter. The effective mass of the photon is m_{ph} is 1.38×10^{-5} of the electron mass m_e; the quantum well width is $5\mu m$; and the potential V_0 is $0.05meV$. The numerical solution of the lowest four discretized energy levels and corresponding wave functions for this finite quantum well are shown in the following figure.

In Figure 2.1.1 for the finite potential well solution, we can still observe the similar energy level trends as in the infinite potential wells. The energy spacings are more sparse as the energy levels increase. One example of these kind of potentials is shown in the following figure:

2.2 Array of One Dimensional Potential Wells

If we put several one dimensional potential wells in an array along the x direction, then we form an array of one dimensional potential wells.

In Figure 2.2, each individual potential well is with V_0 of $0.05meV$ and the potential width is $5\mu m$. For the two-well array, the separation of the two potential centers is $10\mu m$ and the separation is $7.5\mu m$ for the three potential wells example. If we still consider the photon case with effective mass of 1.38×10^{-5} of the electron mass. The wavefuntion solution can be well expressed in the following figure. We are still using the first four energies an examples.

As can be seen from the solution, in Figure 2.5, the first and second, the third and fourth energy states are nearly degenerate. In the left well, they have complete overlapping wavefuction; and in the right well, they have wavefuctions with phase difference of π.

If we move the two potential well closer, the degeneracy will be lifted. This phenomena is illustrated in the next example, where we have the right edge of the

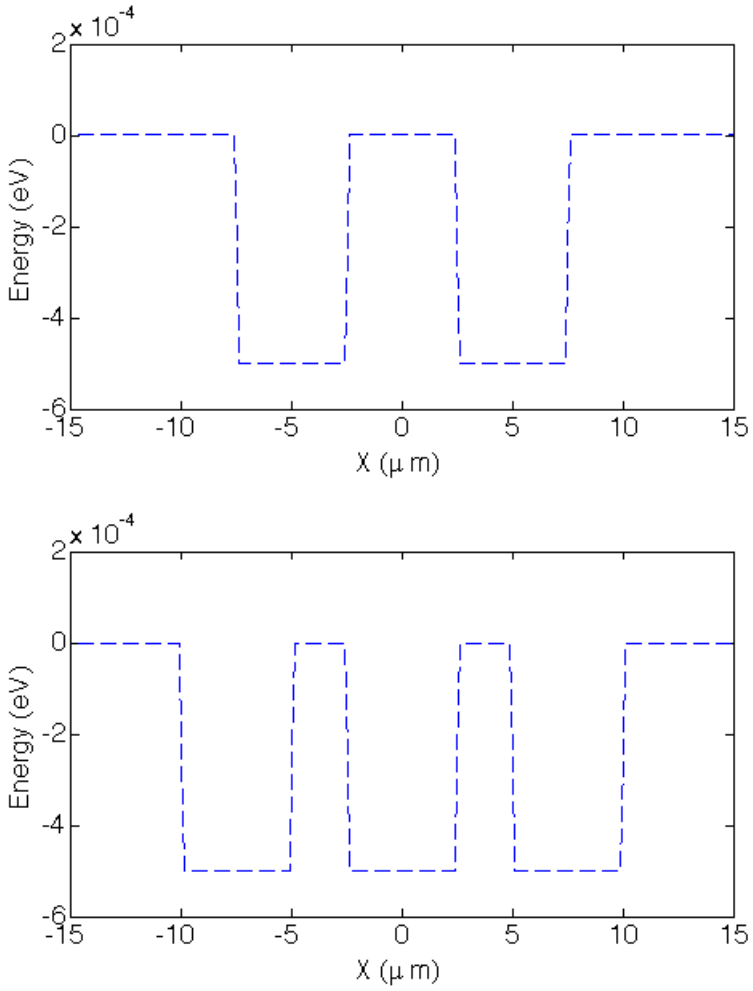

Figure 2.4: Two examples of array of one dimensional potential, with finite potential two quantum wells and three quantum wells separately

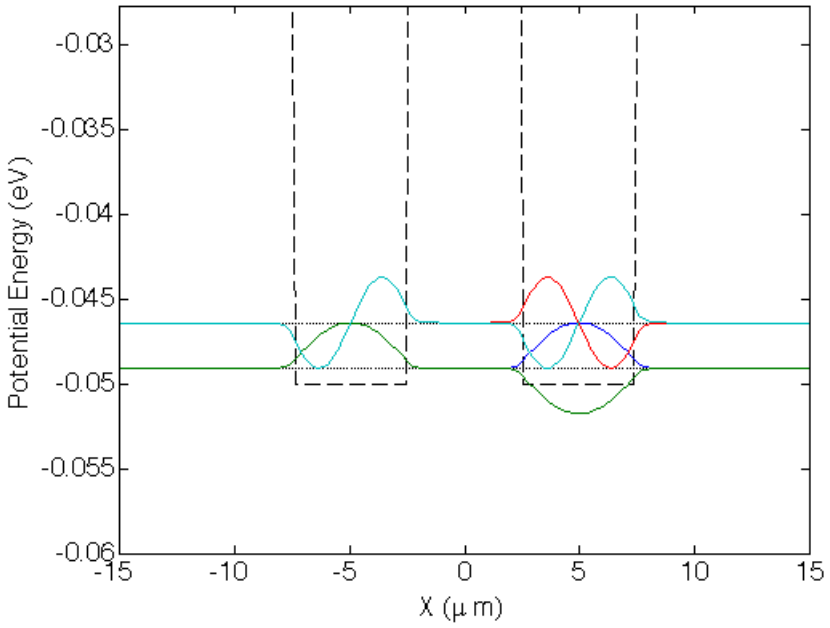

Figure 2.5: Two potential quantum well array solution

left potential is with distance of $0.2\mu m$ away from the left edge of the right potential well. At the same time, we keep the rest of the parameters exactly the same as the previous example. The wavefuction solutions are shown in the following figure.

As can be seen in Figure 2.6, the wavefuctions for the first and second, and for the third and fourth are not overlapping any more. The energies for the first and second, and for the third and fourth are not the same anymore. (The energy difference between the first and second states are not observable due to the calculation resolution.) If we look closer at the space between the two wells, the first and third state wavefuctions are not dropping to zero. It seems that there is connection between the two wells through these wave functions. In this situation, we say the two quantum wells are coupled. We also call these phenomena quantum tunneling. The lifting of the degeneracy is also due to the coupling of these two quantum wells.

From these two examples, we can see quantum tunneling or quantum well coupling

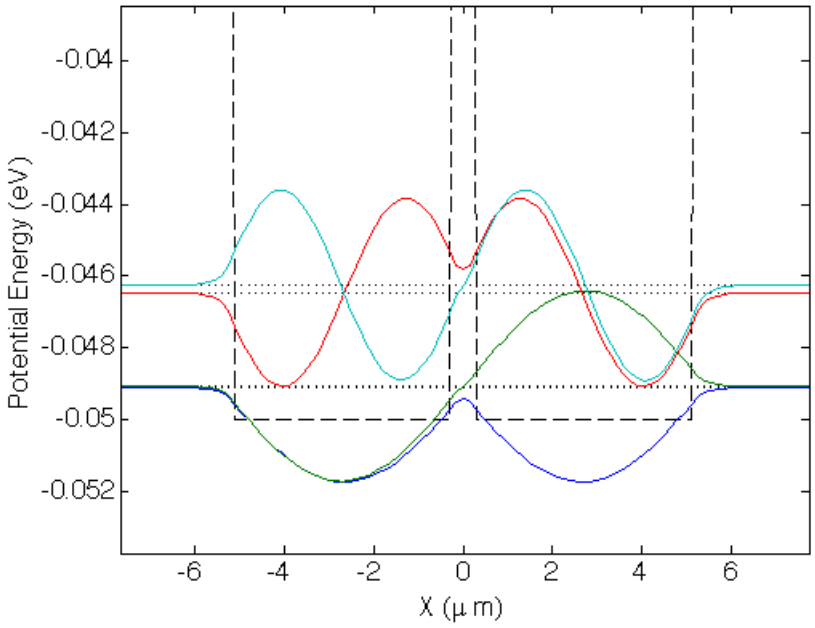

Figure 2.6: Two potential quantum well array solution

is depending on the distance between these two quantum wells. It also depends on the height of the quantum well, V_0.

If we extend the numbers of the coupled quantum wells' number to infinite, the original degenerate quantum levels will expand to a band, while still maintaining the energy difference between the two energy levels. The band gap, which is the evergy difference between the lower energy edge of the higher band and the upper edge of the lower energy band, is depending on the coupling strength between each pair of the quantum wells. This is also the idea of the one dimensional photonic crystal.

2.3 Two Dimensional Quantum Boxes

For the two dimensional quantum box problem, we can just di-sect the problem into two one-dimensional quantum well problems along both directions of x and y. For each of the direction, the energy levels are exactly following the same formula of

the one-dimensional quantum well case.

The energy solution for the two dimensional quantum well case is presented in the following:

$$E_{n_x,n_y} = \frac{\pi^2\hbar^2}{8mL^2}(n_x^2 + n_y^2) \tag{2.11}$$

Based on Equation 2.11, for a square quantum box, the ground state for this two dimensional quantum box is when n_x and n_y both equal to 1, (n_x, n_y)=(1, 1). The second energy or the first excited energy will experience degeneracy since both sides of the quantum box have the exact same dimension. So the states of (1, 2) and (2, 1) are completely degenerate. The second excited state is (2, 2), no degenerate. The energy levels can be calculated for this square quantum box so on and so forth.

CHAPTER III

Microcavity Polaritons

Semiconductor microcavity polaritons are quasi-particles formed by strong coupling of semiconductor excitons and microcavity photons. The unique half-light-half-matter property makes microcavity polaritons an excellent medium for research on light-matter interactions.

3.1 Excitons

In intrinsic semiconductor materials, there are valence bands and conduction bands for electron states, which are formed due to the periodic crystal structure. The energy difference at the bottom edge of the conduction band to the top edge of the valence band is called energy gap. For an unexcited semiconductor material, the valence band is filled with electrons up to the top band edge and the conduction band is empty.

An exciton is a bound state between the excited electron and a hole formed by the Coulomb interaction in semiconductors[72]. An exciton can be formed in an optical excitation process. When a photon is absorbed with approximately the energy of the energy gap, one electron on the top of the valence band will be excited to the conduction band and leave a positively charged vacancy, which we call a hole in

the valence band. This negatively charged electron and positively charged hole will form an electron hole pair due to the Coulomb attraction. This attractive Coulomb interaction will lower the energy of the electron-hole pair. As a result the exciton energy is smaller than the energy gap. In GaAs material, the typical band gap is ∼1.5eV at 10K and the attractive Coulomb energy is called the binding energy, which is on the orders of 10meV. This optical process can be described by using Fermi's golden rule in the following equation:

$$W_{cv} = \frac{2\pi}{\hbar} \sum\nolimits_{f,i} | < f|\hat{H}|i > |^2 \delta(E_f - Ei - \hbar\omega) \tag{3.1}$$

where i and f are the initial state and final state of the electron, H is Hamiltonian for the dipole interaction, E_i and E_f are the intial and final states' energies, and $\hbar\omega$ is the photon energy.

The formation of exciton is illustrated in the schematic Figure 3.1.

Semiconductor excitons have finite life times, usually on the order of *ns*. When one exciton decays, the electron in conduction band falls back to valence band and emits a photon at the same time.

3.2 Semiconductor Microcavity

An optical microcavity is a structure consisting of two highly reflective mirrors positioned face to face to confine photons with certain energies. The trapped photon energy is called the resonance for this optical cavity and is usually determined by the distance of the two mirrors for the cavity. This distance is half of the wavelength of the desired cavity resonance.

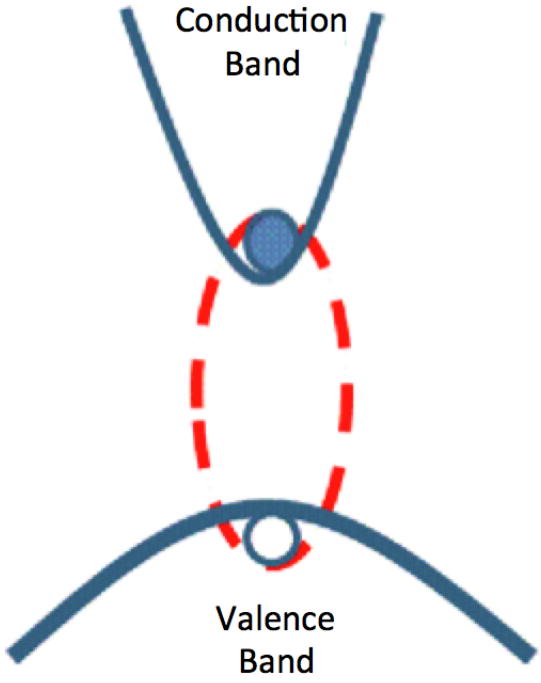

Figure 3.1: An electron-hole pair or exciton is formed in a direct bandgap semiconductor

To form a semiconductor high reflective mirror, we use distributed Bragg reflectors (DBR). A typical DBR structure is composed of alternating high and low refraction index material layers, each with an optical thickness of $\lambda/4$. The DBRs reflectivity can be expressed in the following equation:

$$R = |\frac{n_o n_2^{2N} - n_t n_1^{2N}}{n_0 n_2^{2N} + n_t n_1^{2N}}|^2 \tag{3.2}$$

where n_0 is the refractive index for the light incident media, n_1 and n_2 are the refractive indexes for the two alternating semiconductor materials, n_t is the refractive index for the termination media . N is the number of the paris of the alternating high and low index layers. The DBR reflector can also have very high reflectivity for a broader range of wavelengths around the cavity resonance. The range of these

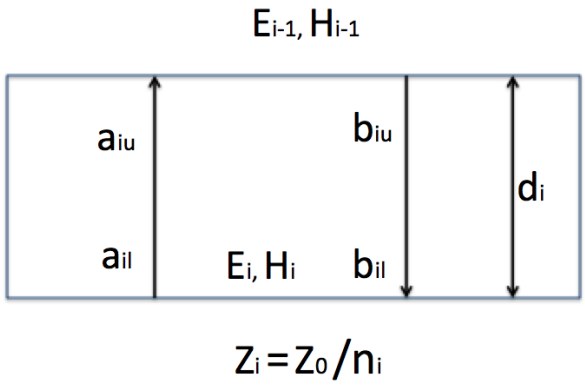

Figure 3.2: Single layer structure for light propagation described by using transfer matrix.

wavelengths is called the stop-band for the DBR.

To simulate the reflection spectrum of DBR, we can use the transfer matrix method. Transfer-matrix method is a very efficient way to trace the optical wave through a layered medium. The method is based on Maxwell's equations and the continuous boundary conditions at the interface of the different materials medium. Transfer matrices are also efficient ways to trace the propagation of light in multiple different layers with different refractive indexes. For a stacked material system, transfer-matrix method also gives simple and accurate expression of system's reflectivity and transmission.

In Figure 3.2, the electric field component and magnetic field component of the light wave inside this ith layer is related to the corresponding field components in the $(i-1)th$ layer. This relation based on Maxwell's equations and continuous conditions at the boundary can be described as:

$$\begin{pmatrix} E_{i-1} \\ H_{i-1} \end{pmatrix} = M_i \begin{pmatrix} E_i \\ H_i \end{pmatrix} \tag{3.3}$$

where i is the dummy indices noting the number of the stratified material layer. In Figure 3.2, the superscripts u and l are indicating the upper and lower interfaces. The electric field and magnetic field components can be described in the following equation:

$$\begin{aligned} E_i &= a_{il} + b_{il} \\ H_i &= \frac{(a_{il} - b_{il})}{z_i} \end{aligned} \tag{3.4}$$

Also based on the phase differences due to the light propagation, for E_{i-1} and H_{i-1} can be described in the following:

$$\begin{aligned} E_{i-1} &= a_{iu} + b_{iu} \\ E_{i-1} &= a_{il}exp(-ik_i d_i) + b_{il}exp(ik_i d_i) \\ H_{i-1} &= \frac{a_{il}exp(-ik_i d_i) - b_{il}exp(ik_i d_i)}{Z_i} \end{aligned} \tag{3.5}$$

Obtain the expressions for a_{il} b_{il},

$$\begin{aligned} a_{il} &= \frac{E_i + Z_i H_i}{2} \\ b_i &= \frac{E_i - Z_i H_i}{2} \end{aligned} \tag{3.6}$$

Based on previous equations, Equations: 3.4 3.5 and 3.6, we can derived the expression for E_{i-1} and also H_{i-1},

$$
\begin{aligned}
E_{i-1} &= \frac{E_i + Z_i H_i}{2} exp(-k_i d_i) + \frac{E_i - Z_i H_i}{2} exp(k_i d_i) \\
E_{i-1} &= E_i cos(k_i d_i) - i Z_i H_i sin(k_i d_i) \\
H_{i-1} &= \frac{E_i + Z_i H_i}{2 Z_i} exp(-i k_i d_i) - \frac{E_i - Z_i H_i}{2 Z_i} exp(i k_i d_i) \\
H_{i-1} &= -\frac{i}{Z_i} sin(k_i d_i) + H_i cos(k_i d_i)
\end{aligned} \tag{3.7}
$$

Hence,

$$
\begin{aligned}
E_{i-1} &= [cos(k_i d_i)] E_i + [-i Z_i sin(k_i d_i)] H_i \\
H_{i-1} &= [-i \frac{sin(k_i d_i)}{Z_i}] E_i + [cos(k_i d_i)] H_i
\end{aligned} \tag{3.8}
$$

If we express Equation 3.8 in a matrix form:

$$
\begin{pmatrix} E_{i-1} \\ H_{i-1} \end{pmatrix} = \begin{pmatrix} cos(k_i d_i) & -i Z_i sin(k_i d_i) \\ -i \frac{sin(k_i d_i)}{Z_i} & cos(k_i d_i) \end{pmatrix} \begin{pmatrix} E_i \\ H_i \end{pmatrix} \tag{3.9}
$$

If we compare Equation 3.9 and Equation 3.4, we can easily get

$$
M_i = \begin{pmatrix} cos(k_i d_i) & -i Z_i sin(k_i d_i) \\ -i \frac{sin(k_i d_i)}{Z_i} & cos(k_i d_i) \end{pmatrix} \tag{3.10}
$$

For a stack of stratified layer materials, the transfer matrix is just the matrix multiplication from the initial transfer matrix M_i to final transfer matrix M_f:

$$
M_{total} = M_1 M_2 \ldots\ldots M_{final} \tag{3.11}
$$

One important feature about a optical structure is the reflectivity. We can use the transfer matrix method to derive the reflectivity for the stacked optical structure. The total transfer matrix can also be expressed explicitly:

$$M_{total} = \begin{pmatrix} m_{11} & m_{12} \\ m_{21} & m_{22} \end{pmatrix} \tag{3.12}$$

The reflectivity is just the ratio of b/a, so this quantity for a N layer structures can be derived in the following:

$$R = |\frac{Z_{N+1}m_{11} + m_{12} - Z_1 Z_{N+1} m_{21} - Z_1 m_{22}}{Z_{N+1}m_{11} + m_{12} + Z_1 Z_{N+1} m_{21} + Z_1 m_{22}}|^2 \tag{3.13}$$

By using the transfer matrix method, the reflection spectrum of the DBR can be simulated. The following Figure 3.3 presents the simulation results for the reflectivity of an example DBR reflector.

In the example simulation Figure 3.3, the central wavelength for the stop-band is 790 nm. The refractive indexes n_1 and n_2 are refractive indexes for materials of $Al_{0.15}GaAs$ and $AlAs$. The number of the DBR paris N is 30.

Still using the transfer matrix method, we can also calculate the reflection spectrum for a DBR-DBR cavity as shown in the following figure:

For this 15 pairs of DBR sandwiched microcavity, the corresponding reflection spectrum is simulated,

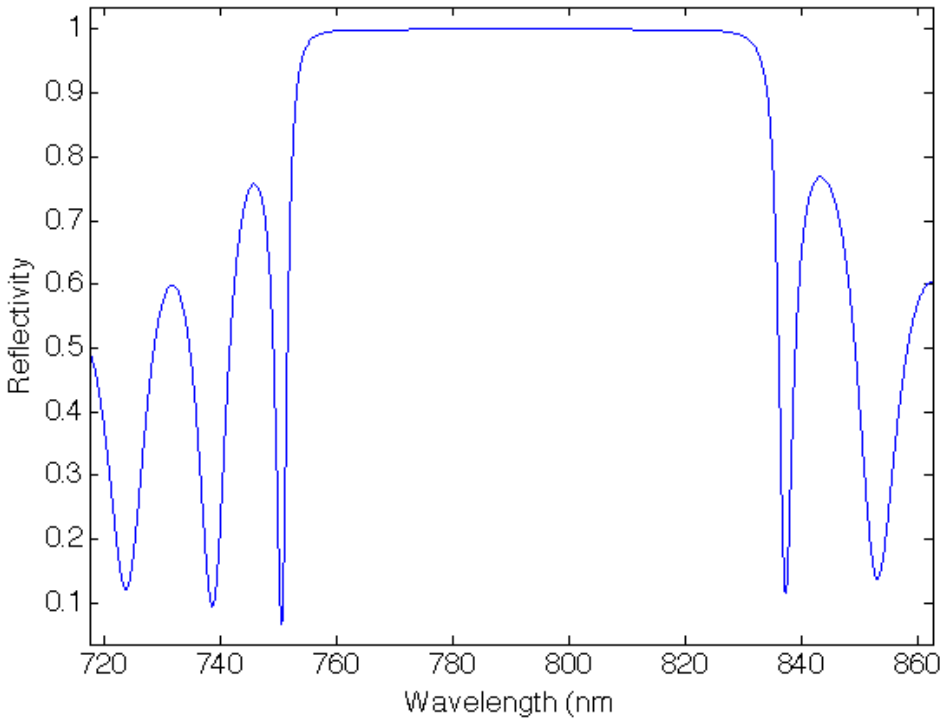

Figure 3.3: An example of DBR reflectivity by transfer matrix simulation

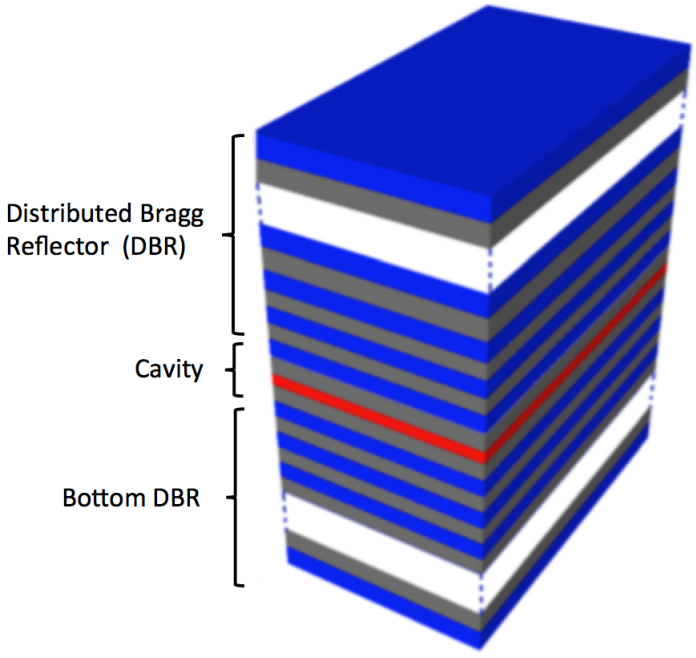

Figure 3.4: DBR - DBR microcavity sturcture

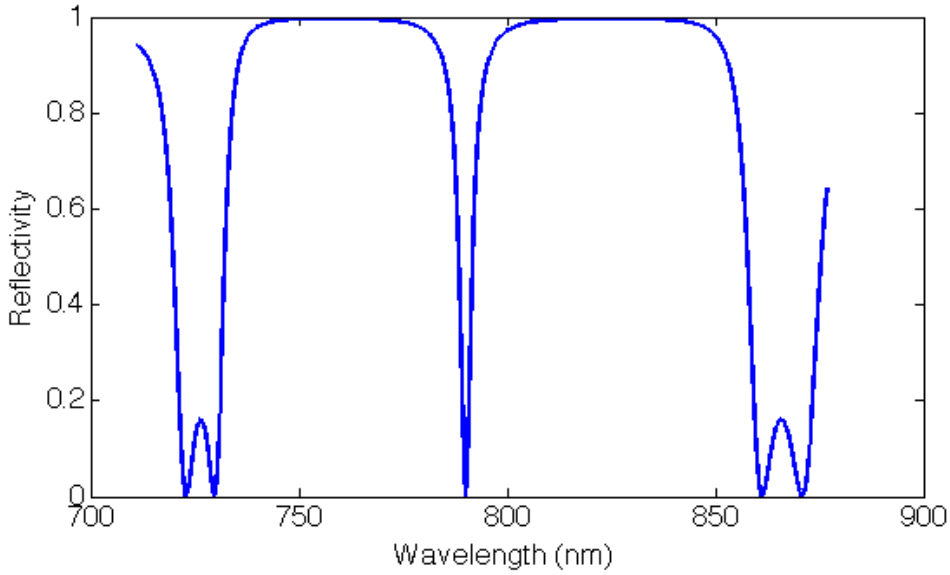

Figure 3.5: An example of DBR cavity resonance in reflectivity spectrum by transfer matrix simulation

One important characteristic parameter for the DBR cavity is the quality factor Q which is defined as:

$$Q = \frac{\lambda}{\Delta\lambda} \approx \frac{\pi(R_1 R_2)^{1/4}}{1-(R_1 R_2)^{1/2}} \tag{3.14}$$

where λ is the cavity resonant wavelength, $\Delta\lambda$ is the line width of the cavity resonance. In the Figure 3.5, it is giving an example using two 15 pairs of DBR on top and bottom to bandwidth a half $\lambda = 790\ nm$ cavity. From the transfer matrix simulation, the line width of the cavity resonance is approximately 4 nm. Hence the quality for this micro cavity is approximately 200.

Based on the quality factor equation, increasing the number of pairs of the alternating layers can increase the reflectivity of the mirrors. Increasing the contrast of the refractive indexes between two alternating material can increase the mirrors

reflectivity as well as expand the width of the stop-band. Based on the quality factor Q equation, both of these methods will increase the quality factor for the DBR cavity.

For a planar DBR cavity, the dispersion relation of a microcavity photon can be derived. If we define the z-direction as the microcavity photon confined direction, the photon is not confined along the perpendicular plane to the z-direction. The cavity photon energy can be written in the following form:

$$E_{cav} = \frac{\hbar c}{n_c}\sqrt{k_\perp^2 + k_\parallel^2} \tag{3.15}$$

where the vertical wave-number $k_\perp = 2\pi n_c/\lambda$. There is also one to one correspondence between the in-plane wave-number and the light incident angle. Based on the microcavity photon energy equation, one example of a microcavity photon relation is depicted in the figure below with cavity resonance at wavelength of $802nm$ or energy of 1.546eV,

When $k_{//}$ is much smaller than $k_\perp$, we can make the parabolic approximation for the microcavity photon dispersion. The dispersion will be:

$$E_{cav} = \frac{\hbar c}{n_c k_\perp}(1 + \frac{k_\parallel^2}{2k_\perp^2}) \tag{3.16}$$

$$= E_{cav}(k_\parallel = 0) + \frac{\hbar^2 k_\parallel^2}{2(2\pi\hbar/\lambda c)} \tag{3.17}$$

$$= E_{cav0} + \frac{\hbar^2 k_\parallel^2}{2m_{cav}} \tag{3.18}$$

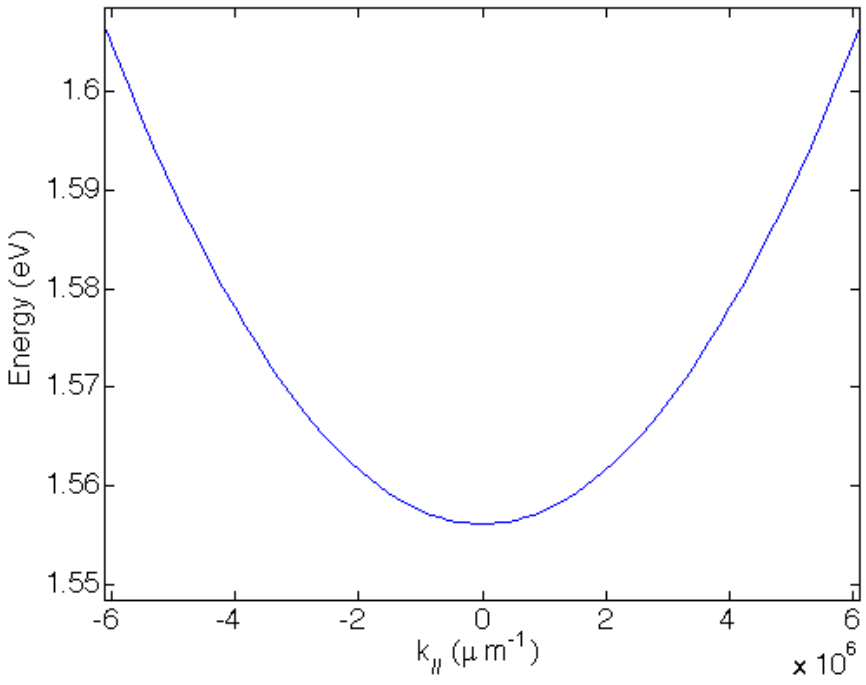

Figure 3.6: An example of microcavity photon dispersion

Therefore we can have a good estimation about the effective mass of the microcavity photon, which is:

$$m^*_{cav} = \frac{2\pi\hbar}{\lambda c} n_c^2 \tag{3.19}$$

For an 800nm resonance microcavity with a refractive index of 3.5, the effective mass of the corresponding microcavity photon is 3.7×10^{-5}that of electron mass. So the effective mass of the microcavity photon is extremely small.

3.3 Microcavity Polaritons

If we place the quantum wells at the antinodes of the semiconductor microcavity, strong interactions between the quantum well excitons and cavity photons are ex-

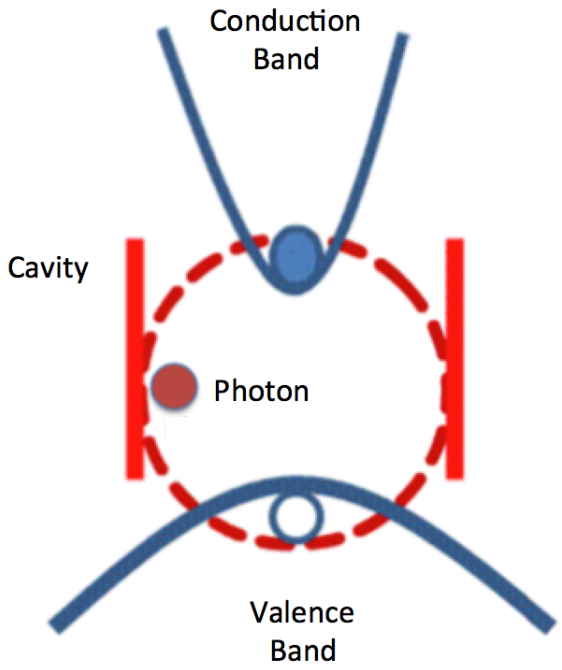

Figure 3.7: Polariton formation scheme

pected. If the interaction is strong enough that the energy exchanging rate is faster than the decay rate of the cavity photons and quantum well excitons, new eigen-states can be created. Thus, we call these new eigen-states microcavity polarities. These new eigen-states were firstly observed in experiments by Weisbuch etc in 1992 [73].

Using similar illustration as in Figure 3.1, the formation of this new quasi-particle, polariton, is illustrated in the following Figure 3.3,

This energy exchanging process and emerging of the new eigen-states, polaritons, can be described in the following Hamiltonian under rotating wave approximation:

$$\hat{H}_{total} = \hat{H}_{exciton} + \hat{H}_{cavity} + \hat{H}_{interaction} \tag{3.20}$$

This Hamiltonian equation can also be expressed explicitly in the matrix format:

$$\hat{H}_{total} = \begin{pmatrix} E_{exciton} & 2\hbar\Omega \\ 2\hbar\Omega & E_{cavity} \end{pmatrix} \tag{3.21}$$

After diaganolization of the matrix, the solutions for the Haimiltion, which are the new eigen-states or polariton states can be expressed in the following equation. We also call these two polariton states upper-polariton and lower polariton

$$E_{UP,LP} = \frac{1}{2}[E_{exciton} + E_{cavity} \pm \sqrt{4\hbar^2\Omega^2 + (E_{exciton} - E_{cavity})^2}] \tag{3.22}$$

E_{cavity} and $E_{exciton}$ are the cavity resonant energy and quantum well exciton energy. $2\hbar\Omega$ represents the interaction strength between the cavity photons and quantum well excitons. $E_{UP} - E_{LP} = 2\hbar\Omega$, the energy difference between upper polariton (UP) and lower polariton (LP). This energy is also known as the 'Rabi Splitting' energy. The energy difference between the exciton energy and cavity photon energy, $E_{cavity} - E_{exciton}$ is often called detuning. When detuning is negative, we have cavity photon-like LP and exciton-like UP at lower $k_{\|}$; when detuning is positive, we have photon-like UP and exciton-like LP at lower $k_{\|}$. When detuning is zero, in both UP and LP, the photon and exciton components are exactly at half. Different fractions of photons and excitons in UP and LP will generate different dispersion relations. Based on Equation 3.22, the calculated results of negative, zero and positive detuning are illustrated.

In Figure 3.3, the calculations are using, $E_{exciton} = 1.551eV$, Rabi Splitting at $2\hbar\Omega = 10meV$, both positive and negative detuning are at $\Delta E = 5meV$. The blue

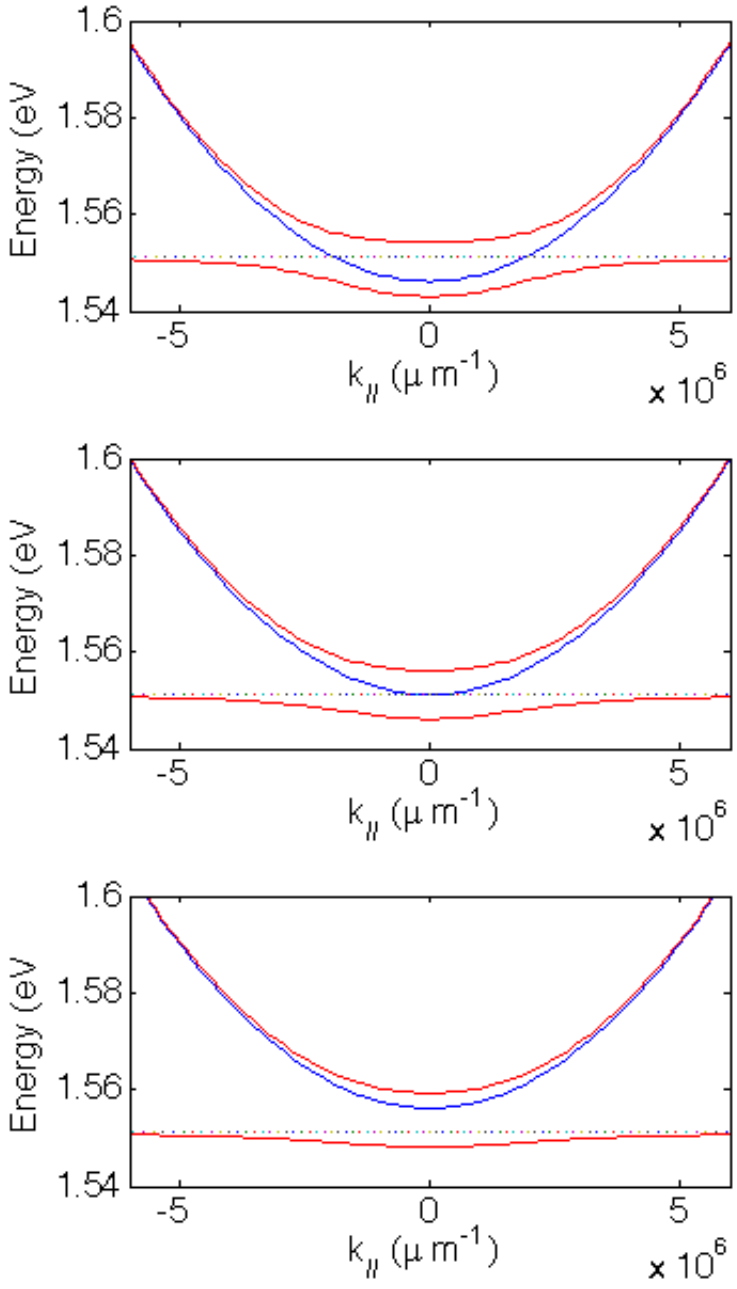

Figure 3.8: UP and LP dispersion relation at three different detuning energy

lines are indicating the dispersion relations for the cavity photons, the dotted lines are indicating the quantum well exciton energies and the red lines are indicating the dispersion relations for the UPs and LPs in all three figures.

The effective masses for UP and LP are defined in the following equations:

$$\frac{1}{m^*_{UP}} = \frac{|C|^2}{m_{exc}} + \frac{|X|^2}{m_{cav}} \tag{3.23}$$

$$\frac{1}{m^*_{LP}} = \frac{|X|^2}{m_{exc}} + \frac{|C|^2}{m_{cav}} \tag{3.24}$$

where m_{exc} and m_{can} are the effective masses for quantum well excitons and cavity photons. C and X are the photon and exciton fractions. The different effective masses for UP and LP can also be seen from these three different detuning cases in Figure 3.3, we can observe the curvature changes at low $k_{\|}$. These dispersion relations capture the variation of the effective masses for polaritions. Generally speaking, the effective mass of the exciton is usually 10^5 times of the effective mass of the cavity photon. As can be seen, even for a zero detuning $E_{cavity} - E_{exciton} = 0$, half-exciton-half-photon polartion, the effective mass of the polariton is taking majorly from the effective mass of the cavity photon. Therefore, this kind of polariton effective mass is very small.

CHAPTER IV

Subwavelength High Contrast Gratings

4.1 Subwavelength Gratings

A set of gratings is an optical component with a periodic structure that splits and diffracts light into several beams traveling in different directions. A typical group of the optical gratings is illustrated in the Figure 4.1.

The period of the gratings is d. The light is incident from angle θ_i and the diffraction angle is θ_m, where m is the diffraction level. The relation between the incident light and diffraction light follows the grating equation, which is:

$$d\left(sin(\theta_i) + sin(\theta_m)\right) = m\lambda \tag{4.1}$$

λ is the wavelength of the incident light. From Equation 4.1, we see that if $\lambda > d$ and we want to maintain the equality in real numbers, the only possible solution is let $m = 0$. Then $sin(\theta_i) = -sin(\theta_m)$. We only have zeroth order of diffraction which is just the reflection. Therefore, for a sub wavelength grating, where the period of the grating is smaller than the wavelength, we have very strong reflection of the incident light. By using this property of the sub-wavelength gratings, we can

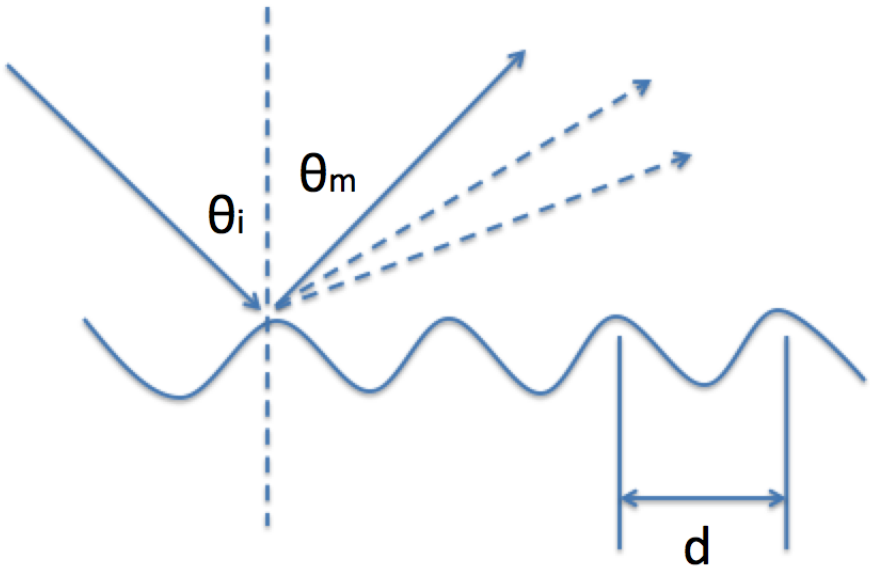

Figure 4.1: A schematic of a typical set of diffraction gratings

use these gratings as very high quality mirrors. The high contrast gratings we will introduce here are also utilizing this property of the sub-wavelength gratings.

4.2 High Contrast Gratings

4.2.1 General Properties of High Contrast Gratings

A high contrast grating is a single layer with periodic structures, where the refractive index of the grating materials has very large contrast compared to the surrounding material. A schematic of a typical rectangular shaped gratings is shown in Figure 4.2

The period of the grating is Λ; the length of the space between the grating bar is a; the thickness of the single layer of the gratings is t. The ratio of the grating bars width $(\Lambda - a)/\Lambda$ is called the gratings' duty cycle. For future discussion convenience,

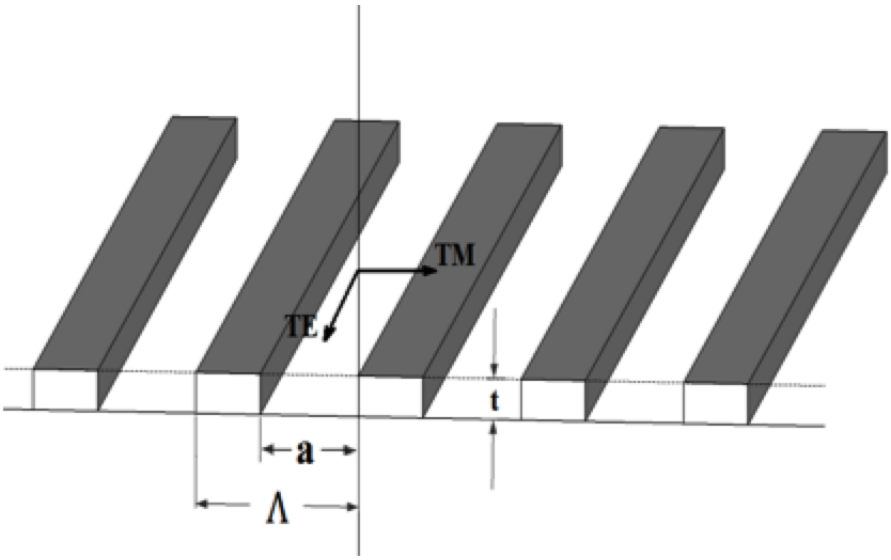

Figure 4.2: A schematic of high contrast gratings (HCG)

we also define the TE polarization as the direction when the electric field of the incident light is along the grating bars, and TM polarization as the direction when the electric field is perpendicular to the bars direction.

One of the important features of the HCG is that it can provide very high reflectivity from just a single layer as compared with traditional DBR with 20 - 30 times thicker of material. Meanwhile, the range of the wavelength for high reflectivity (stop-band) for HCG-DBR cavity is wider in comparison with a traditional DBR-DBR cavity. Another important feature for the HCG is that it can also provide polarization selectivity by providing very high reflection for one polarization and minimize the other due to the intrinsic symmetry-breaking structure. Hence the HCG is a very good candidate for a very good quality microcavity. These three good features are also shown in the following figures of examples

A typical HCG-DBR cavity drawing in in Figure 4.3, where sub wavelength grating

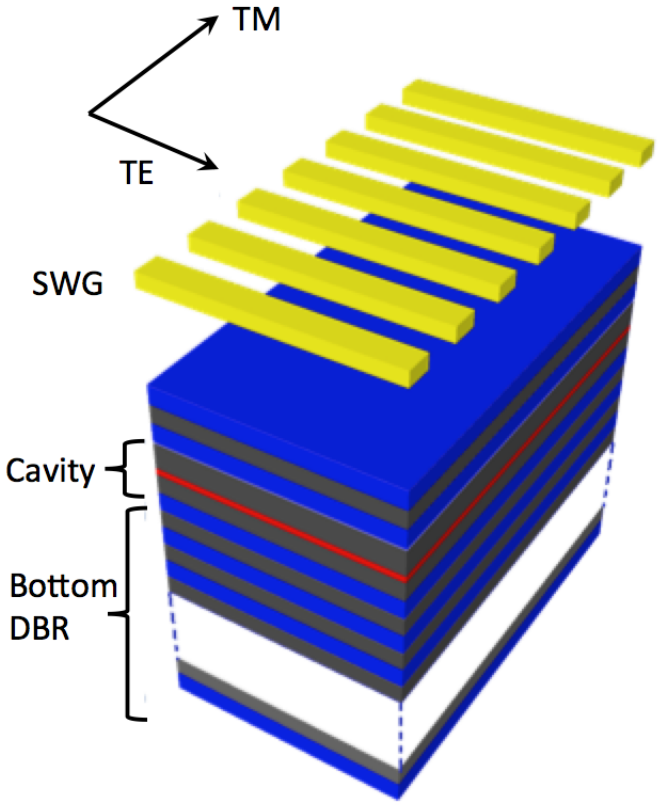

Figure 4.3: An HCG - DBR cavity drawing

(SWG) is just the HCG. The reason to keep the top several layers of the DBR is to prevent the over etching issue for fabrication purposes.

For this kind of HCG-DBR cavity, the broader range of the stop band feature is shown in the example in Figure 4.4

Also for the cavity Q factor comparing in terms of the thickness of the devices for HCG-DBR cavity and the traditional DBR-DBR cavity, calculation results are shown in Figure 4.5. HCG-DBR has a comparable Q value of very good quality as that of a very thick DBR-DBR cavity.

Finally, the polarization control can be optimized for certain gratings design by tuning the period, duty cycle and thickness of the gratings. This is shown in Figure

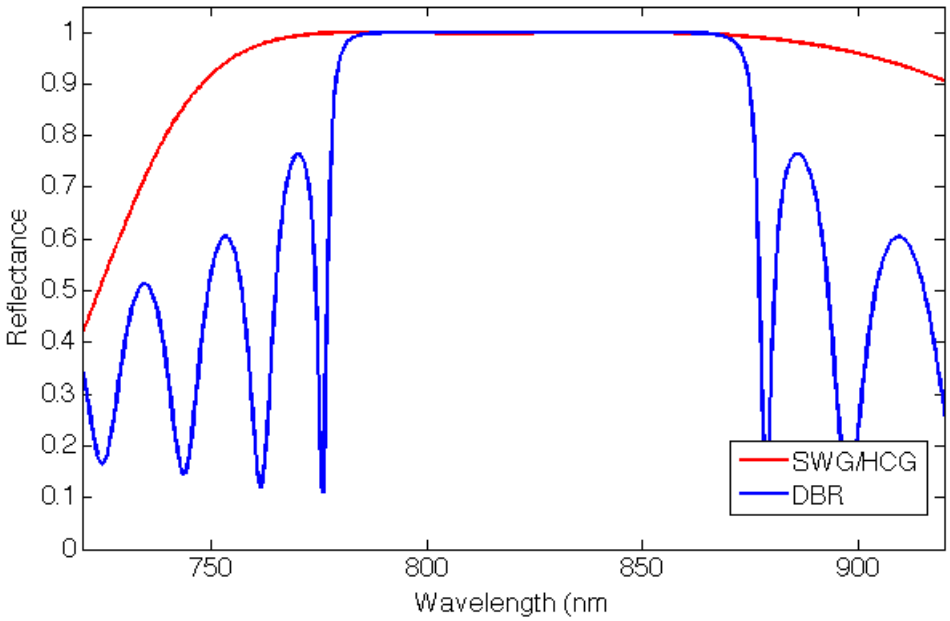

Figure 4.4: Reflection spectra calculated for SWG/HCG-DBR cavity and DBR-DBR cavity

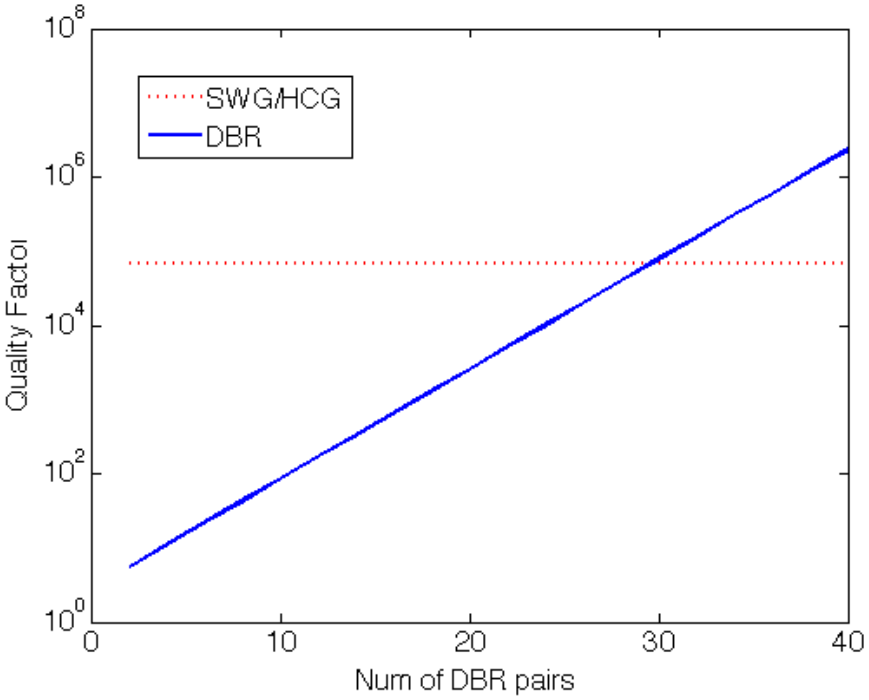

Figure 4.5: SWG/HCG - DBR cavity and DBR-DBR cavity Q value comparison

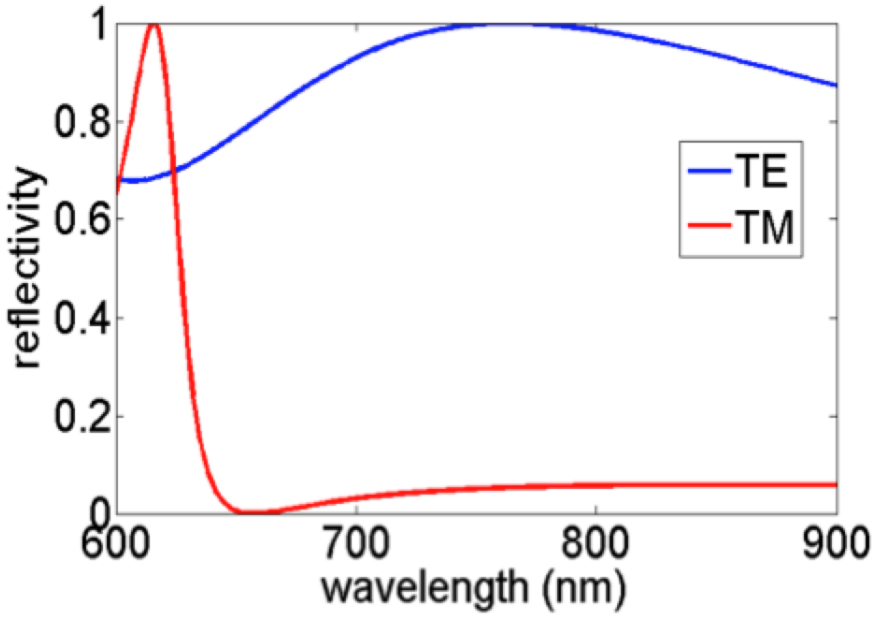

Figure 4.6: Reflection spectra for two polarizations TE and TM, calculated for a certain design of HCG optimized for TE polarization

4.6, where we have a sample design which is optimized for very high reflectivity for TE polarization and the at the same time, the reflectivity of TM polarization remains very low for over $200nm$ wavelength range.

4.2.2 Subwavelength HCG-DBR Cavity Design and Optimization

One desired properties for the HCG-DBR cavity is that the high reflectance is resistant to relatively large angle, which means the HCG has large incident angle tolerance. Here in this section for the HCG-DBR cavity design, we will take the large angle tolerance into consideration. We will also focus on $Al_{0.15}GaAs$ as the grating layer material since that is the material we use for all of the research devices.

The energy vs. in-plane momentum dispersion of a planar cavity is governed by the angular dependence of the cavity mirrorss reflection phase. This is shown by the round-trip phase condition for the cavity resonance:

$$\Phi_1(\omega, k_{//}) + \Phi_2(\omega, k_{//}) - 2dk_{c\perp} = 2m\pi \tag{4.2}$$

Here ω is the angular frequency of the resonance, $k_{//}$ and $k_{c\perp}$ are the in-plane and longitudinal wavenumbers in the cavity layer, respectively, d is the distance between the two cavity mirrors, and m is an integer. The first two terms Φ_1 and Φ_2 are the reflection phases of the two cavity mirrors. Equation 4.2 uniquely determines the dispersion relation $\omega(k_{//})$.

A conventional DBR-DBR cavity exhibits a rigid quadratic dispersion because the DBR's reflection phase is close to π over a wide range of $k_{//}$. Let $\Phi_1(\omega, k_{//}) \approx \Phi_2(\omega, k_{//}) \approx \pi$, using $k_{c\perp} = \sqrt{((n_c\omega)^2 - k_{//}^2)}$, for small $k_{//}$, we obtain a quadratic dispersion:

$$\omega(k_{//}) \approx \omega_0[1 + \frac{k_{//}^2}{2(n_c\omega_0/c)^2}] \tag{4.3}$$

Here $\omega_0 = \omega(k_{//} = 0)$ and n_c is the refraction index of the cavity. For an $AlAs$ cavity, $k_{//}^2/(n_c\omega_0 c)^2 < 0.1$ is satisfied up to an incident angle $\theta_0 = 44$ in vacuum. The curvature of the quadratic dispersion is determined by n_c and ω_0, with no additional tuning available.

In contrast, an HCGs reflection phase can have a stronger and more complicated angular dependence, enabling dispersion engineering. Reflection from the periodic hCG structure is produced by scattering between the lateral modes inside the SWG and Floquet-form diffraction modes outside. The lateral modes of an HCG can be

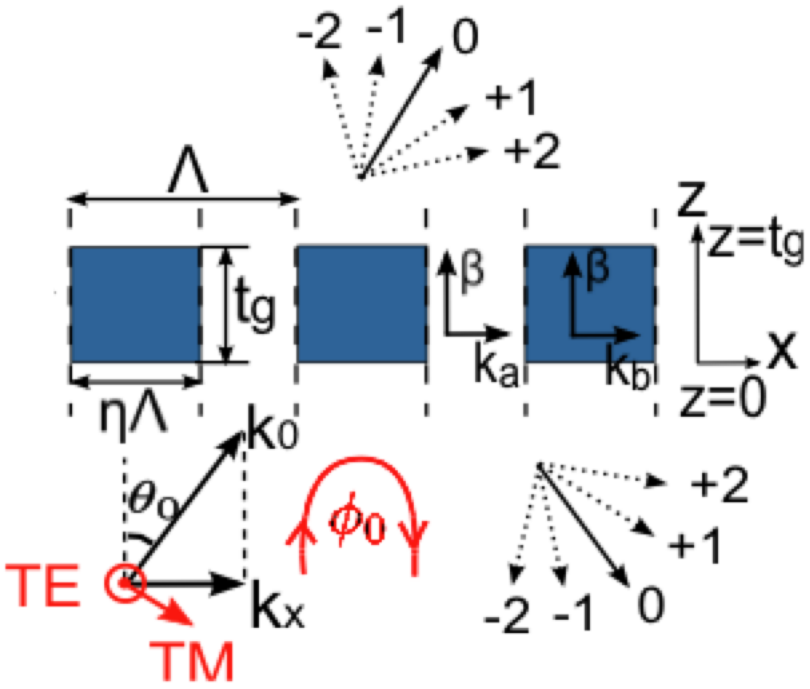

Figure 4.7: Schematic of an HCG structure for optimization

analyzed using waveguide- array (WGA) modes, which was introduced in to explain intuitively the high reflectance of the HCG at normal incidence. Below we generalize the work in and derive the WGA modes in HCGs of arbitrary thickness in the general case of oblique incidence. We show that, due to symmetry properties of the grating, the dispersion of the WGA-modes could shift considerably with the incidence angle, leading to large changes in the reflection phase.

We treat the HCG as a waveguide array with z-axis as the propagation direction shown in Figure 4.7. It is periodic in the x-direction and translationally invariant in the y-direction. We focus the discussion on the case of an incident plane wave propagating in the x-z plane with an oblique angle θ_0 from z-direction. For a WGA mode with transverse-magnetic (TM) polarization as labeled in 4.7, the lateral mode profile H(x) and propagation constant β are determined by an eigenvalue equation,

$$(\frac{\partial^2}{\partial x^2} + n^2(x)\frac{\omega^2}{c^2})H(x) = \beta^2 H(x) \tag{4.4}$$

where n(x) is the refractive index profile. Because of the periodicity of n(x), the eigenmode can be expressed in a Bloch-wave form,

$$H(x) = exp(ik_x x)u_n(x) \tag{4.5}$$

where $exp(ik_x x)$ is the Bloch phase factor, where the wavenumber k_x is determined by the incident wave in- plane wavenumber $k_x = \omega/csin(\theta_0)$. $u_n(x)$ is a periodic function, where the subscript n denotes the discrete mode number. Given ω and θ_0, we can solve for the eigenvalues β_n^2 and obtain the $\omega - \beta$ dispersion of WGA-modes through:

$$2n_b^2 k_a k_b(cos(k_a a)cos(k_b b) - cos(k_x \Lambda)) - (n_b^4 k_a^2 + k_b^2)sin(k_a a)sin(k_b b) = 0 \tag{4.6}$$

where n_b is the refractive index of the grating bar; a and b are the widths of the air and bar regions; $k_{a,b}$ is the transverse wavenumber in air or bar region, determined by $k_{a,b} = \sqrt{(n_{a,b}\omega/c)^2 - \beta^2}$. An example of a WGA mode dispersion is shown in Figure 4.8.

In the case of normal incidence (blue lines), the incident wave matches the reflection symmetry of the grating about the center of the grating bars. Correspond-

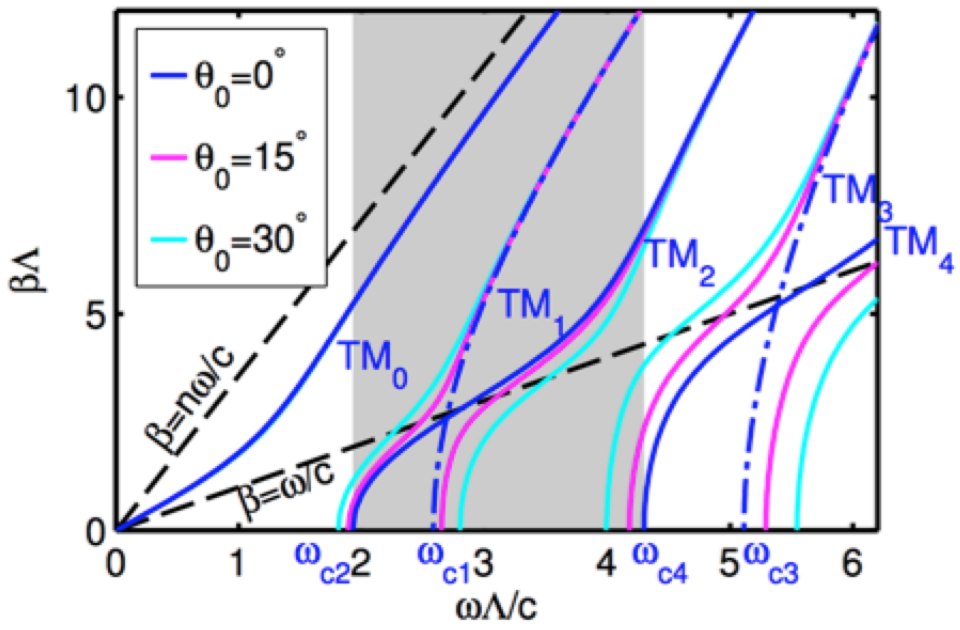

Figure 4.8: The $\beta - \omega$ dispersions of the TM WGA-modes in an HCG with a duty cycle $\eta = 65\%$, for incidence angles of 0 degree, 15 degree and 30 degree.

ingly, $TM_{0,2,4,...}$ modes have the same symmetry and thus can be excited, while the $TM_{1,3,5,...}$ modes have the odd symmetry and thus cannot be excited.

In the case of oblique-angle incidence, the incident plane waves no longer has the reflection symmetry, and thus the odd-order modes can also be excited. Avoided crossings between the odd-order and even-order modes lead to significant shift of the mode dispersions, as illustrated in Figure 4.8.

Reflection from an HCG with finite thickness t_g can be understood as resulting from interference of WGA modes reflected from both the top and bottom HCG-air interfaces. For a given WGA, for example the WGA used in Figure 4.8, we can visualize the dependence of the reflection on t_g using $t_g-\omega$ maps of the reflectance and reflection phase, as shown in Figure 4.9. For each of the WGA mode in Figure 4.8, the HCG forms a Fabry- Perot resonator when the approximated round-trip phase condition $\beta t_g = m\pi$ is satisfied, where m is an integer. We mark the corresponding $t_g - \omega$ values in Figure 4.9with white dashed and dash-dotted lines for the TM_0 and TM_2 modes, respectively. The reflectance is nearly zero around these lines and the reflection phase changes by π across the lines, which are signatures of Fabry- Perot resonances. Naturally, high reflectance region exist only between these lines, when two WGA modes co-exist and produce nearly perfect destructive-interference at the output plane of HCG.

At oblique angles, the appearance of the odd-order WGA modes leads to large shifts of the WGA modes, which manifests as large shifts of the reflectance and phase patterns on the $t_g - \omega$ maps. An example is shown in Figure 4.9(c)-(d) for $\theta_0 = 30$. Consistent with the $\beta - \omega$ diagram (Figure 4.8), the Fabry-Perot resonance lines originated from the TM_0 mode barely move, while those from the TM_2 mode move toward lower frequencies. The high reflectance regions, as well as the phase in these

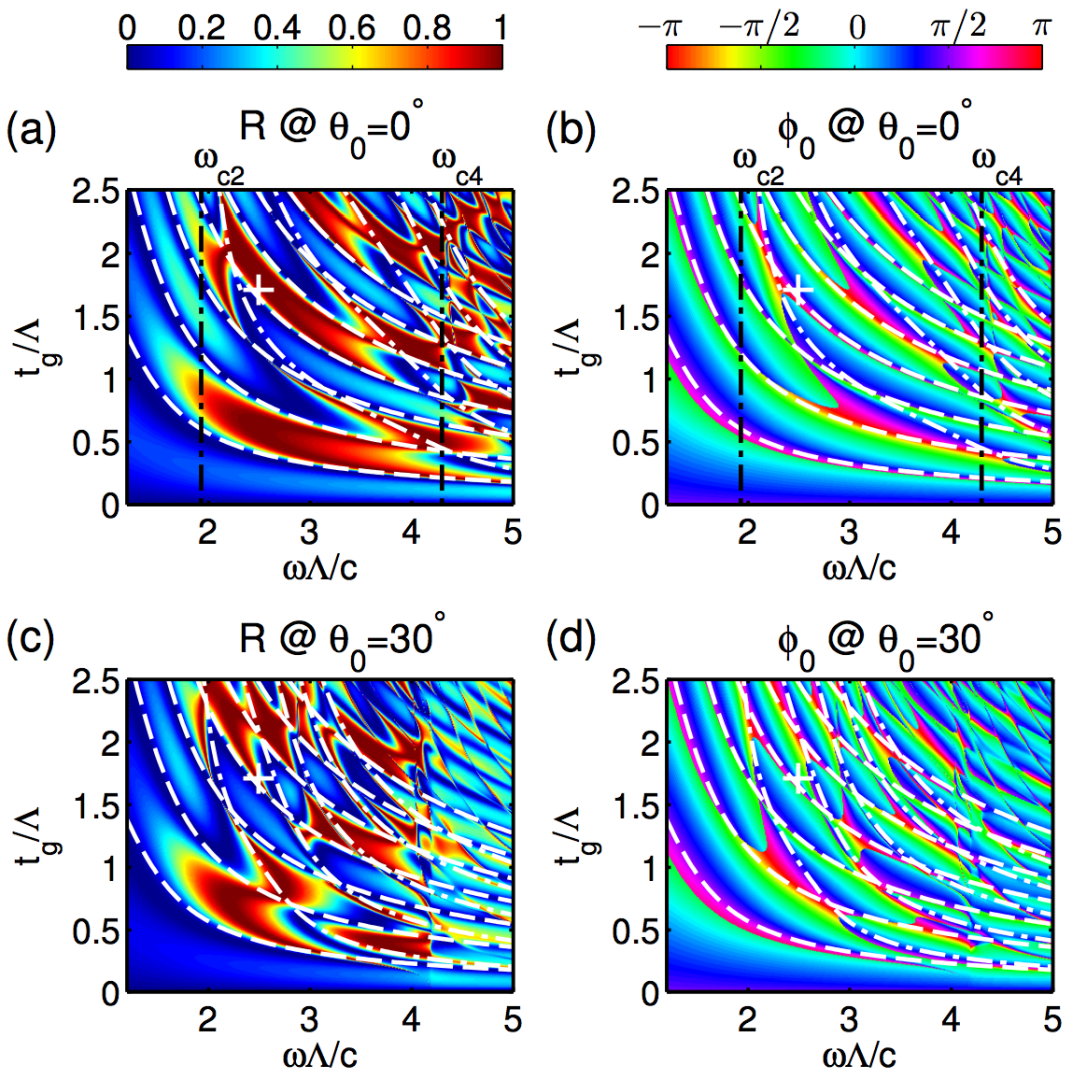

Figure 4.9: $t_g - \omega$ maps of the reflectance ((a) and (c)) and reflection phase ((b) and (d)) of a SWG with $\eta = 65\%$ for the TM polarization, under normal incidence ((a) and (b)) and $\theta_0 = 30$ degree oblique incidence ((b) and (d)). The black dash- dotted lines in (a) and (b) show the dual-mode regime defined by ω_{c2} and ω_{c4} obtained in Figure 4.8. The dispersions of the dual WGA modes are plotted as the two sets of white dashed and dash-dotted lines in all four figures, using the approximated Fabry-Perot resonance condition of $\beta t_g = \pi$. These lines overlap well with the zero-reflectance (blue) stripes in (a) and (c). Broadband high-reflectance regions (red) can be found between those lines. Each point on the figure corresponds to one SWG design. An example is marked by the white + symbol, which has a phase shift of 0.4π over 30 degree while maintaining high-reflectance (> 0.995).

regions, move with those grid lines. For a certain HCG in the high-reflectance region, for example the point marked by a white star in Figure 4.9, the reflection phase could become very different at oblique incidence angles.

4.3 Device Fabrication

To fabricate the sub-wavelength high contrast gratings, the process includes pattern definition by using electron beam (e-beam) lithography, reactive ion etching or dry etching, selective wet chemical etching and critical point drying. The fabrication process is illustrated in the flow chart in Figure 4.10.

4.3.1 Electron Beam Lithography

Electron beam lithography is using high speed electrons to do patterning at nanometer scale with programmed electromagnetic field. It has been developed for tens of years and became a standard nano-device processing steps in semiconductor device research[74]. It is also the very first step of the fabrication for our sub-wavelength high contrast grating devices. As shown in the fabrication flow in Figure 4.10, it begins with the e-beam resist coating. Even though this is a very simple and straightforward step, it has significant impact on the quality of the pattern drawing. Since we are also using the resist as the etching mask, the thickness of the e-beam resist can not be too thin. Otherwise, we jeopardize of damaging the surface of the gratings which could eventually lead to poor quality of the device.

The ebeam machine to fulfill the patterning task is Raith-150. There are several parameters we have considered here in order to have grating patterns with relatively good quality (grating edge wiggling $<$ 10nm, required from tolerance simulation by design). So to reach this resolution, we used high voltage, small aperture and

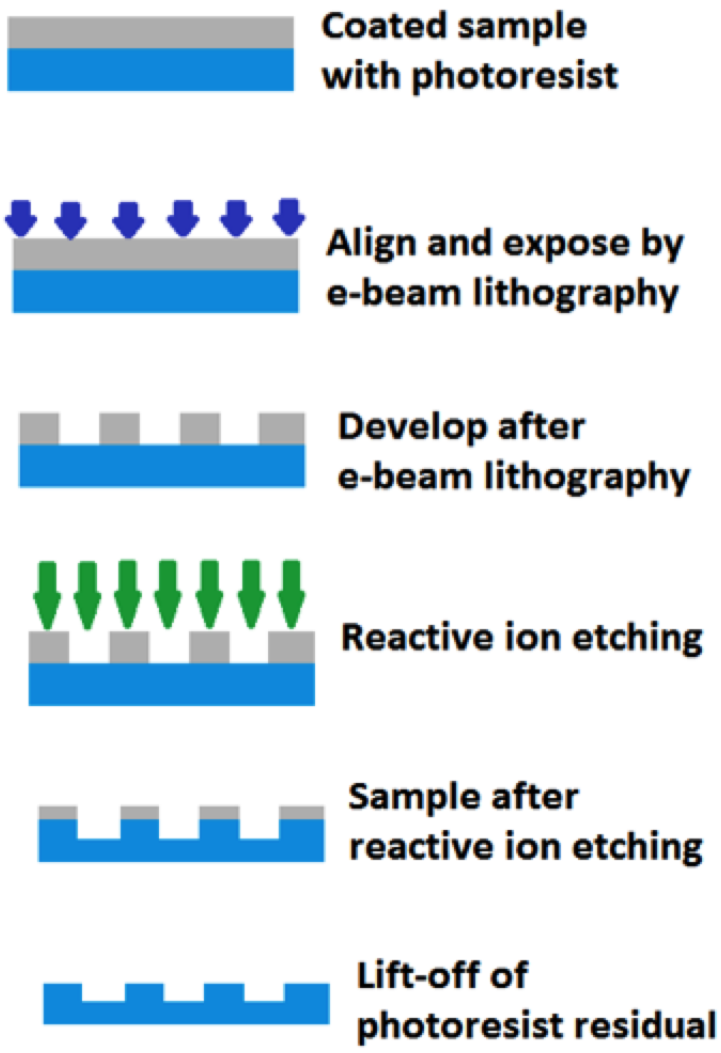

Figure 4.10: Fabrication flow

relatively appropriate working distance. Higher voltage is for faster speed of the electrons, so the wavelength of the electrons will be shorter. The aperture and working distance are not straightforward to tune. In principle, we should have used smaller working distance F, and larger aperture D. So the value of (F/D) is small, which determines the imaging resolution in classic Gaussian optics. However there is another important issue we have to consider is the electrons' trajectory in the beam resists. One is forward scattering and the other is the reflective scattering. Too much of these two scatterings will decrease the resolution of the patterning. In practice, we did use relatively small working distance to have good resolution. At the same time, we also use a bit smaller aperture to compensate the enhanced forward and back-forward scattering due to the smaller working distance. After several iterations of optimization for the ebeam patterning process, the final recipe we used for the pattern by Raith-150 is, voltage = 20MV, working distance F= 6 μm and aperture D= 7.5 μm. The patterning results are shown together with the photoresist optimization in Figures 4.11, 4.12, and 4.13.

There are two types of the e-beam resist I have developed to fabricate the devices. One is the poly-methyl methacrylate (PMMA), which is the traditional e-beam resist; the other is the high quality, very electron sensitive, newly developed ZEP-520 from Zeon Corp.

To maintain enough e-beam patterning resolution using PMMA, I used PMMA A4; to have a thick enough etching mask, I also used $200nm$ of the PMMA. For a testing sample after dry etching, a typical testing results after the dry etching process is shown in Figure 4.11 and Figure 4.12. As can be seen, even though the grating pattern has enough resolution, the e-beam resist mask has minimum residual from the cross-section view. This will possibly damage the edges of the gratings due to the

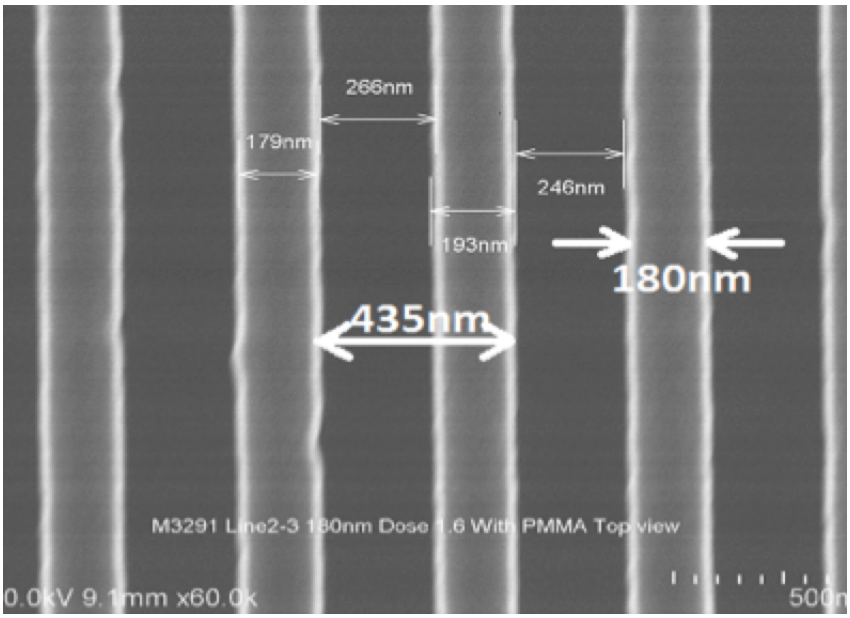

Figure 4.11: A testing sample after e-beam lithography and dry etching using PMMA. View from the top.

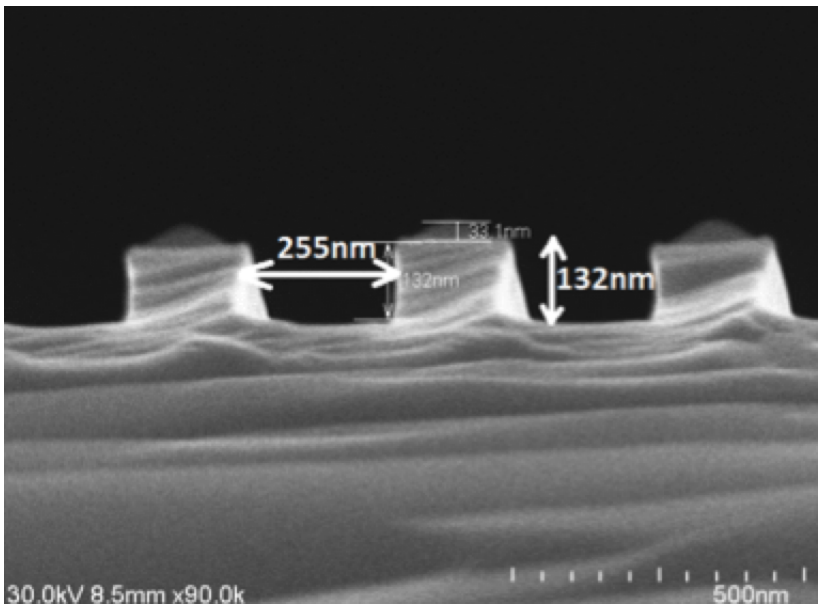

Figure 4.12: A testing sample after e-beam lithography and dry etching using PMMA. Cross section view.

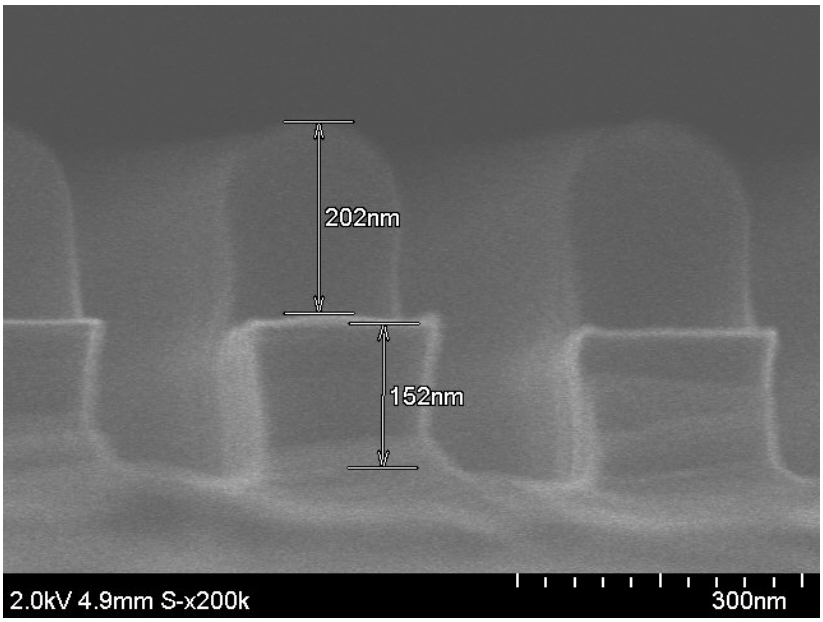

Figure 4.13: A testing sample after e-beam lithography and dry etching using ZEP. Cross section view.

dry etching variation. However, this can not be improved by just simply increase the thickness of the e-beam resist, as a thicker e-beam resist will reduce the patterning resolution.

To solve this problem, ZEP-520a has been used to replace PMMA A4 as the e-beam resist. It is highly sensitive to the electrons even with very high thickness, which gives enough patterning resolution and also behaves as an excellent dry etching mask.

As can be seen from Figure 4.13, grating patterns with similar period and duty-cycle have been fabricated. After using the same dry etching recipe for the testing sample, we still have significant amount of the ZEP e-beam resist on top the grating patterns in comparison with the testing sample using PMMA A4. By using ZEP as the e-beam resist and etching mask, we still have the desired resolution for the grating patterning; at the same time, the grating material underneath has been well protected.

The recipe for ZEP e-beam patterning is: 2500 RPM spin-on rate, which will give 450 nm thickness for patterning. After spun on ZEP, 180 C baking for 3 - 5 min to dry and bake out the chemical resolution. For this thickness of ZEP, the central dose for the dose matrix is targeting at 50 $\mu C/mm^2$, which is 4 -5 times less compared to PMMA A4. Right after the e-beam patterning, we use Xylene as developing solution for about 2 min. To strip off the ZEP e-beam resist, PRS-2000 can be used for 10 -20 min (The cleaning results might be better if PRS-2000 solution is heated up).

4.3.2 Reactive Ion Etching

Reactive Ion Etching or dry etching is the immediate step after e-beam patterning. Dry etching is the step to transfer the pattern on e-beam resist to the actual sample. It is using the plasma ions under directional voltage to bombard the surface of the material. For the part which is exposed, the bombardment will take effect; for the part which is protected by the etching mask (for our process, it is the e-beam resist), the bombardment will be shielded. So in this way, the patterns on the mask/e-beam-resist will be transferred to the first layer of the sample.

The dry etching process is taking advantage of the physical reaction of the bombardment as well as the chemical etching process. So different semiconductor material will be utilizing different chemical ions. For GaAs and AlAs material, the effective chemical etchant is Cl. The Cl ions not only bombard the surface of the unprotected sample, they also have the active chemical reaction with Ga an Al components in the material. So the dry etching process is very effective.

To control the etching rate of the dry etching process, there are several parameters we can control. The most important one is the voltage between two panels. This voltage controls the electrical field inside the etching chamber, therefore has great

impact on the ions' acceleration and speed. Another parameter is the voltage to trigger the plasma inside the chamber. It is usually around a few hundreds of volts. To incorporate the plasma igniting voltage, a proper rate of the chemical flow should be considered at the same time. Finally, the temperature should also be controlled while etching. Temperature normally wouldn't affect the behavior of the etchant, yet it plays an important role for the e-beam etching mask. At relatively high temperature (e.g. 50C), the organic e-beam resist will become relatively soft so it will not be protecting the material below very well and the etching rate for the e-beam resist is very high. At lower temperatures (e.g. 5C), the e-beam resist tends to be very hard and behave as a very good etching mask. If all the parameters collaborate well, it will take a few minutes to etch through several hundreds of nanometers of the GaAs or AlAs material.

The recipe for GaAs material I used for the final device is presented here. The chemical flow rates are: Cl_2 is 1 sccm, BCl_3 is 4 sccm and Ar is 8 sccm. The voltage between the charged panel is 40 V, and the voltage for the plasma triggering is 250 V. Finally the etching temperature is at 5 C.

4.3.3 Selective Wet Chemical Etching

The final step for the device fabrication is the wet chemical etching with high selectivity. During this process, the sacrificial layer beneath the gratings will be etched away selectively. As a result the gratins will be only surrounded by air, so the very high contrast gratings will be formed. This process is illustrated in the following sketch with actual sample structure after e-beam and dry etching patterning.

There are several chemical etchant which could reach the goal of the selectively etch Al rich $Al_{>0.5}GaAs$ material while have minimum effect on Ga rich $Al_{<0.5}GaAs$

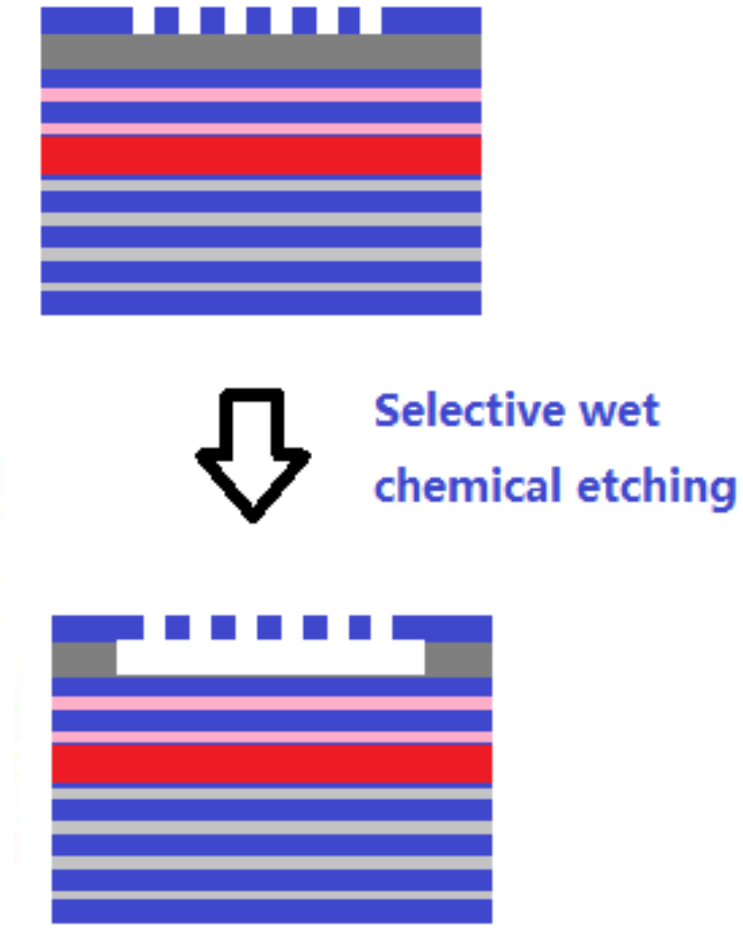

Figure 4.14: Wet chemical etching

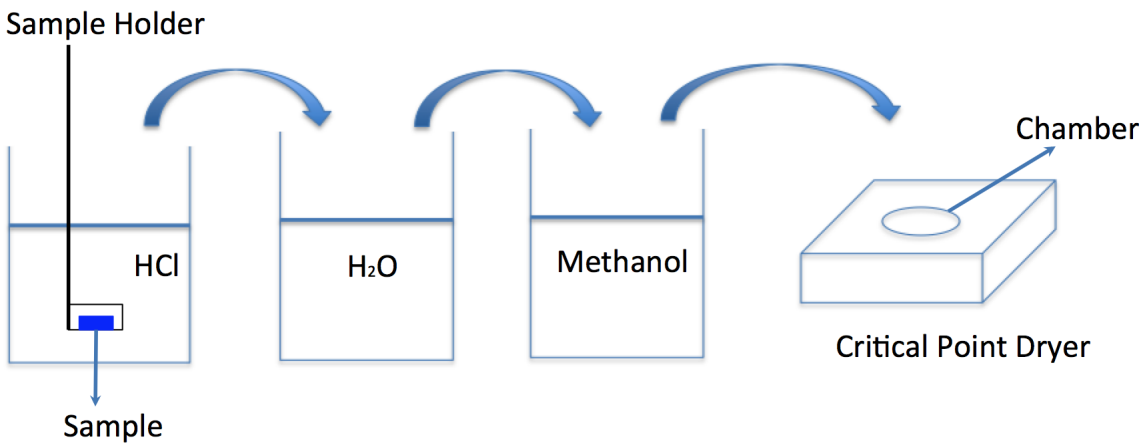

Figure 4.15: Process after wet etching, sample transfer and critical point drying

material. For example, HF and HCl are both good choices to fulfill this task. Even though HF is very good candidate to do the selective etching, the selectivity and etching rate are both very high. It is very hard to control during the fabrication process, especially we only need to etch away a few hundred nanometers $Al_{0.85}GaAs$ material.

The final etchant for our sample is HCl. It has very gentle etching rate, so that we can have a good control of the etching time. Also the selectivity is comparable with HF, at 500:1 of AlAl over GaAs. So for 400nm $Al_{0.85}GaAs$ sacrificial material etching, I immerse the sample in HCl for 30 seconds.

After the wet chemical etching, we have to use the critical point dryer to release the patterns as we can not directly take the sample out for N_2 gas blowing to dry. The air-suspending gratings is very fragile. The liquid surface tension will buckle or crash the gratings during the gas-blowing process. Therefore we have to use the critical point dryer for the drying process. The sample cleaning/rinsing and solution buffering process after the wet chemical etching is shown in Figure 4.15.

We also designed the sample holder based on the sample size. The sample holder

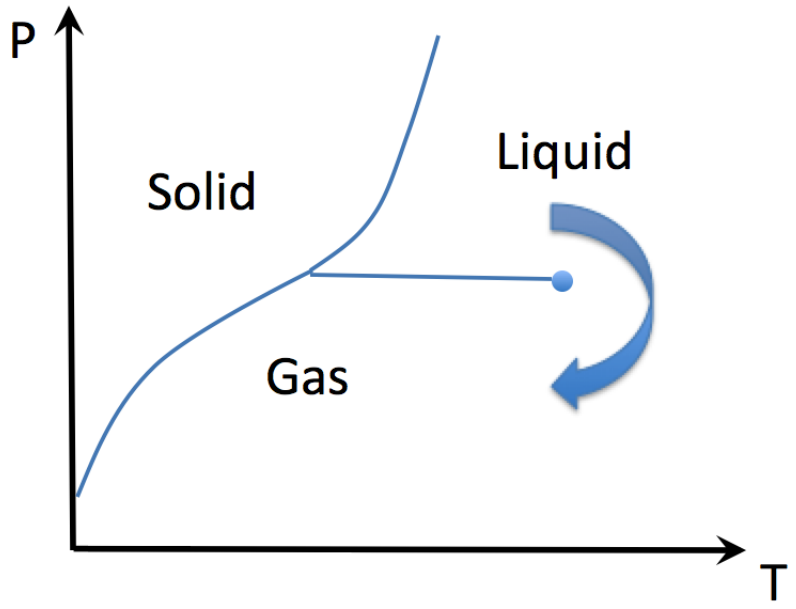

Figure 4.16: Process after wet etching, sample transfer and critical point drying

pocket is not too deep, so during the rinsing process, it will not carry over too much residual etchant. During the whole rinsing process, the sample should be immersed in liquid at all time.

After the wet etching step in HCl, the sample first goes through the de-ionized water to rinse out the HCl. Then we move the sample into methanol which is the starting liquid in critical point dryer to rinse out all the residual water during the cleaning process. Afterwards, we continue to use the same sample holder to move the sample from methanol beaker to the chamber of the critical point dryer. The arrows in Figure 4.15 is indicating the transferring steps during this pattern release process.

Finally, when the sample is fully immersed in the critical point dryer's chamber, the liquid CO_2 will completely replace the starting solution of methanol inside the chamber. Then the dryer goes to relatively high temperature and high pressure as

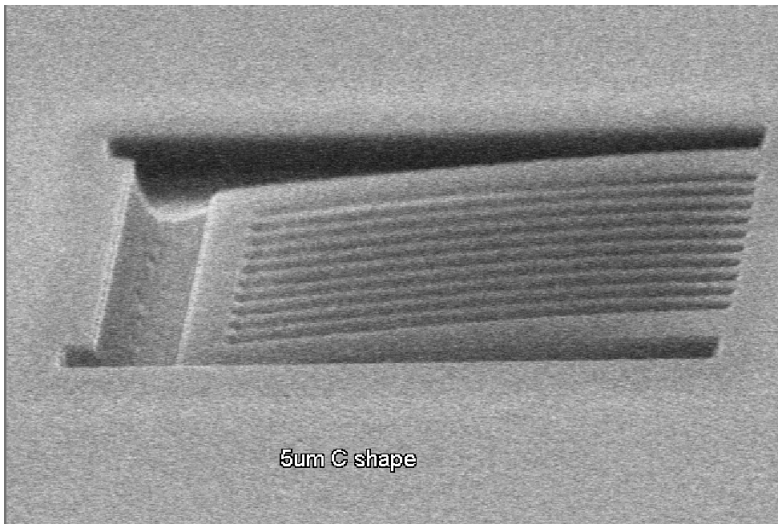

Figure 4.17: An SEM image showing a group of gratings collapse to the bottom after wet etching

programmed around the critical point of CO_2, where the liquid and gas phase can not be distinguished to completely dry out the sample. In this way, the sample does not need to experience the tension due to the liquid drying. This process is illustrated in Figure 4.16.

Even though the gratings should not experience any abrupt phase change in the critical point dryer, a little residual of the methanol or water due to incomplete replacement inside the chamber could cause the damage to the gratings. Since the grating layer is also very thin, the gratings may not be strong enough to support themselves. As a result, we could observe many buckling cases even by using critical point drying.

Two examples are shown for a buckling case in Figure 4.17 as compared to a successful clean case in Figure 4.18. In Figure 4.17, the 5 μm $\times$ 5 μm grating layer complete collapses to the bottom. In Figure 4.18, a 10 μm wide grating layer is suspending. From this cut cross-section view, the air gap between the grating layer and the top of the protection layer is clearly seen. We also notice the protection

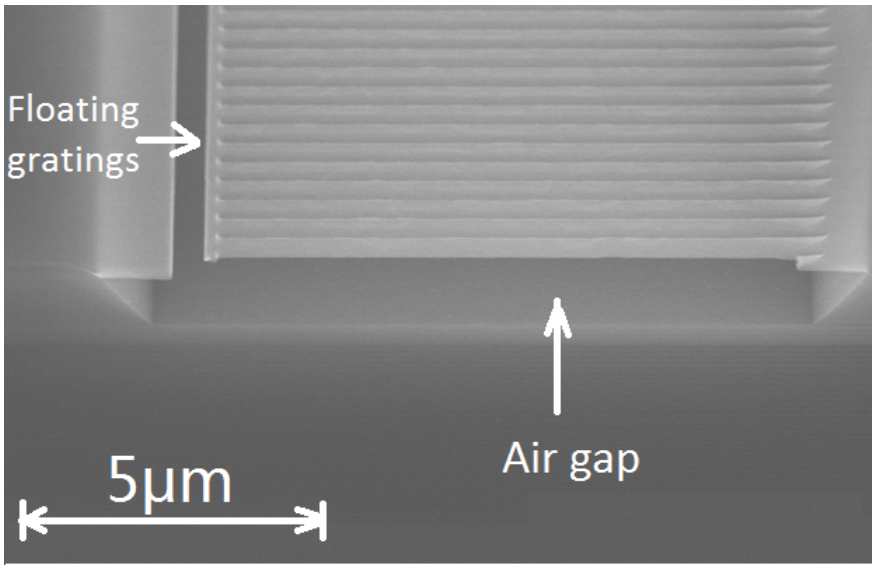

Figure 4.18: An SEM image showing a successful air-suspending group of gratings

layer thickness does not change much at the etching region compared to the planar region. This indicates a very high selectivity during the wet etching process.

CHAPTER V

Zero Dimensional SWG Polariton Device

5.1 Introduction

Foundational work on 2D polariton systems has inspired theoretical schemes for polariton-based quantum circuits, quantum light sources and novel quantum phases. Experimental implementation of these schemes requires the control, confinement and coupling of polariton systems, which remain challenging in conventional microcavity structures.

Important features of a versatile experimental platform based on polaritons include: first, well-defined zero-dimensional (0D) polaritons as building blocks of a coupled system; second, the establishment (i.e., survival) of a non-equilibrium quantum phase in each 0D polariton cell, typically manifested as polariton lasing; third, controllable coupling among the 0D cells; fourth, individual addressability and control of each cell.

In conventional polariton cavities, the thick mirrors, consisting of distributed Bragg reflectors (DBRs), make it difficult for the polaritons to be confined or controlled beyond the perturbative regime. Most existing methods for controlling polaritons lead to a weak modulation potential that modifies the systems properties without reducing its dimensionality from 2D to 0D. Examples include weak con-

finement of excitons via mechanical strain[4] and periodic modulation of the optical modes via surface patterning[46] [75]. Advanced techniques have been developed to embed apertures inside the cavity,[51] [76] which have led to 0D polariton cells, but polariton lasing has not been reported thus far. Alternatively, 0D polariton systems have also been produced via direct etching of the vertical cavity into pillars.

Using this method, two groups have recently achieved polariton lasing in pillars,[52] [77] [41] thus satisfying the first two requirements. However, this approach requires destructive plasma etching throughout the 4- to 6- μm-tall cavity structure as well as the active media layers, which preludes coupling between separate pillars. It is also unclear whether further control of the polariton modes in each pillar would be possible.

In this chapter, a polariton system in an unconventional cavity that can fulfill all four requirements is demonstrated.

5.2 Device Structure

The new cavity structure replaces the top DBR with a slab of photonic crystal (PC) Figure 5.1, which enables confinement and control of the polariton modes by design. At the same time, there is no destructive interface in the active media layers or the main cavity layers; hence, coupling among multiple low-dimensional polariton cells is unhindered. Using this cavity system, we demonstrate 0D polariton lasing at a chosen polarization. The schematic is shown in Figure 5.1 (a).

Before the nano-patterning for the device, the molecular beam epitaxy grown GaAs wafer is with the layer by layer structure as following: 30 pairs of bottom DBR, an $AlAs$ $\lambda/2$ cavity layer, 2.5 pairs of top DBR consisting of $Al_{0.15}GaAs/AlAs$, and

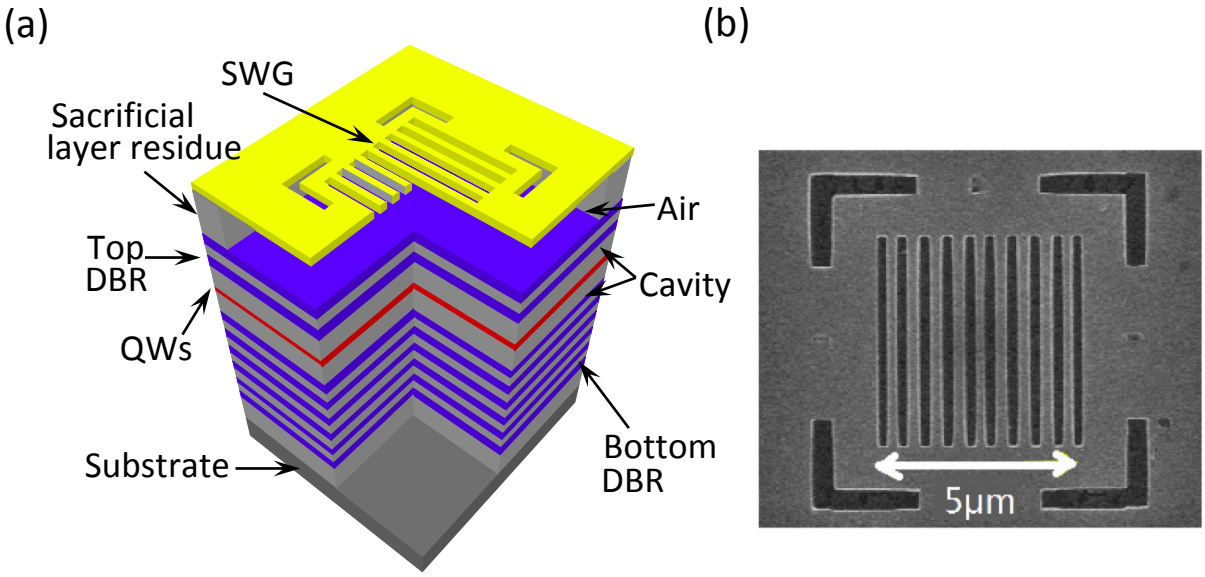

Figure 5.1: Examples of the hybrid cavity.(a)A schematic of a 0D hybrid cavity with a SWG mirror.(b)Top-view SEM image of a fabricated 0D cavity with a SWG of $5\mu \times 5\mu$ in size. 0D, zero-dimensional; SEM, scanning electron microscopy; SWG, subwavelength grating.

an $Al_{0.85}GaAs$ sacrificial layer followed by an $Al_{0.15}GaAs$ top layer. There are 12 GaAs quantum wells distributed in the three central antinodes of the cavity.

We created square gratings of $5 - 8\mu m$ in length (Figure 5.1 b) on the top layer via electron-beam lithography followed by a short plasma etching step. Hydrochloric acid chemical etching was then applied to remove the sacrificial layer, followed by critical point drying. The fabricated gratings are approximately 80 nm thick, with a period of approximately 520 nm and a duty cycle of approximately 40%, and are suspended over an air gap of approximately 300 nm. The gratings are optimized as a high-reflectance mirror for light polarized along the grating bar direction (transverse electric (TE)- polarization). Figure 5.1 (b) shows a scanning electron microscopy image of the top view of one of the devices.

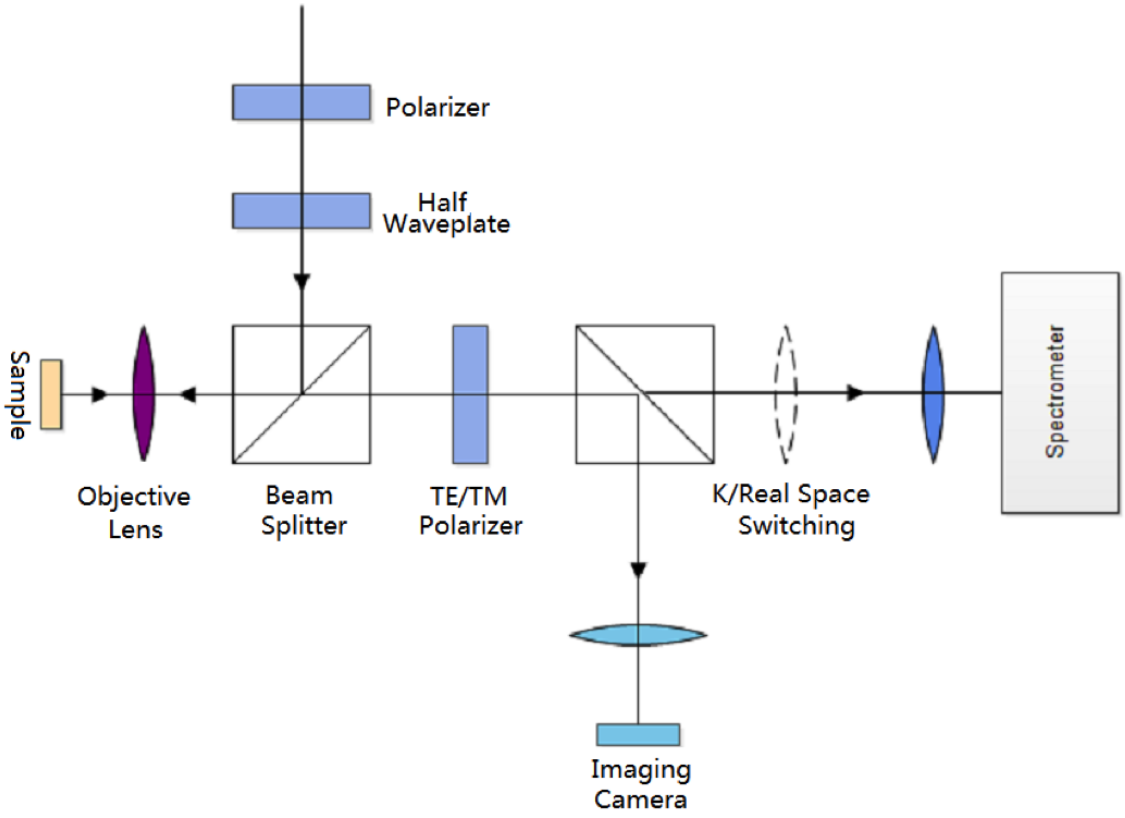

Figure 5.2: Optical characterization set-up for the device.

5.3 Optical Properties of 0D SWG Polariton Device

5.3.1 Optical Characterization Methods

Optical measurements were performed to characterize the pro- perties of the cavity system. For consistency, all data shown were taken on a device of $7.5\mu m \times 7.5\mu m$ in size. The sample was kept at 1090 K in a continuous flow liquid-helium cryostat. The optical measurement set-up in shown in the following Figure 5.2.

For the photoluminescence (PL) measurement characterization: A pulsed Ti:sapphire laser at 740nm was used as the excitation laser, with an 80-MHz repetition rate and

a 100-fs pulse duration. The laser was focused to a spot size of approximately $2\mu m$ in diameter on the device from the normal direction using an objective lens with a numerical aperture of 0.55. The photoluminescence signal was collected with same objective lens, followed by real space for Fourier space imaging optics, and then sent to a 0.5-m spectrometer with an attached nitrogen-cooled charge coupled device (CCD).

The spectrally resolved real space and Fourier space distributions were measured by selecting a strip across the center of the Fourier space and real space distributions using the spectrometers entrance slit. The resolution of the measurements was limited by the charge-coupled device pixel size to $0.3\mu m^{-1}$ for Fourier space imaging and by the diffraction limit to 0.4 mm for real space imaging.

For the reflection measurement characterization, we are using a similar set-up. Tthe same Ti:sapphire pulsed laser with 100 - fs pulse duration was focused on the device. Instead of using the wavelength of $740nm$, we use central wavelength of 800nm with spectrally line width of 15nm. Similarly, the signal collected by the objective lens was directed into the spectrometer in momentum space. As for the reference reflection, we replace the sample with a dielectric mirror at the exact same position. Dividing the signal intensity from the device by the reference reflection from the mirror, we will get the reflection property of the device.

5.3.2 Spectral Properties of 0D SWG Polariton Device

Strong coupling between the excitons and TE cavity modes was evident in the momentum space images of the emission from within the cavity, as shown in Figure 5.3 (a). Discrete lower polariton (LP) modes and a faint upper polariton (UP) branch were observed below and above the exciton energy, respectively, with dispersions

distinct from that of the cavity photon (the red solid line). In contrast, the emission from outside the hybrid cavity region shows a flat, broad exciton band at the heavy hole exciton energy of $E_{exc} = 1.551eV$ (Figure 5.3 (b)). The energies of the polariton modes can be described as follows in the rotating wave approximation:

$$E_{LP,UP}(k) = \frac{1}{2}[E_{exc}(k) + E_{cav}(k) \pm \sqrt{(E_{exc}(k) - E_{cav}(k))^2 + 4\hbar^2\Omega^2}] \tag{5.1}$$

Here, k is the in-plane wavenumber, E_{cav} is the uncoupled cavity energy and $2\hbar\Omega$ is the excitonphoton coupling strength, corresponding to LPUP splitting at zero excitonphoton detuning. Using Equation 5.1 and the measured $E_{exc}(k = 0) = 1.551eV, E_{LP}(k = 0) = 1.543eV$and $E_{UP}(k = 0) = 1.556eV$, we obtain $E_{cav}(k = 0) = 1.548eV$ and $2\hbar\Omega = 12meV$.

The discrete LP modes show full three-dimensional confinement of the polaritons. The lateral size of the hybrid cavity is determined by the size of the high-reflectance subwavelength grating (SWG). Outside the SWG, there is no cavity resonance, and the excitons are eigen-excitations. Inside the SWG region, the TE-polarized cavity modes strongly couple to the excitons, leading to laterally confined TE-polarized polariton modes. The transverse magnetic (TM)-polarized excitons remain in the weak coupling regime. Because there is not a sharp lateral boundary at which the cavity mode disappears, we phenomenologically modeled the effective confinement potential as an infinite harmonic potential. The calculated energies of the LP modes are indicated by the dashed lines in Figure 5.3 (a), which agree very well with the measured LP resonances. For comparison, the confined cavity modes (crosses) and corresponding 2D dispersions of the LP, UP and cavity modes are also shown (solid lines).

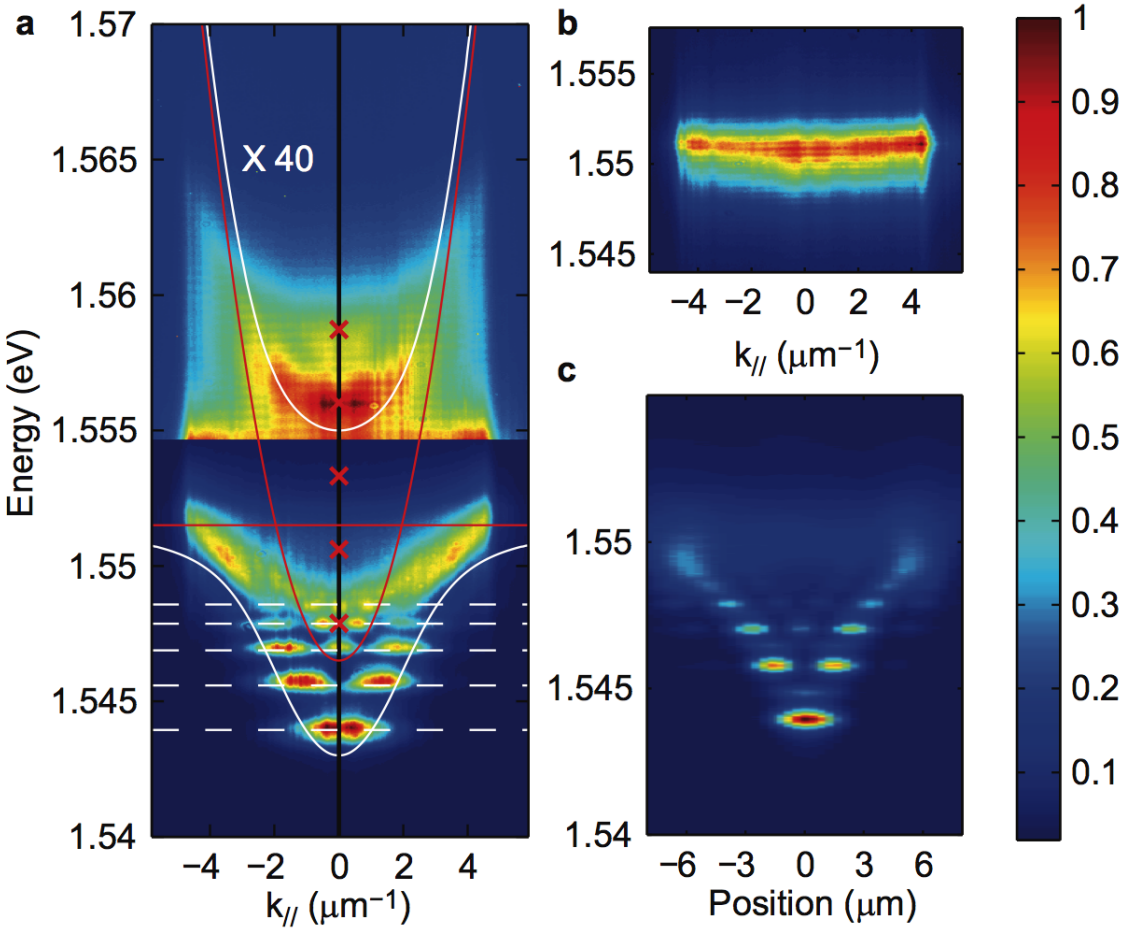

Figure 5.3: Spectral properties of a 0D polariton device.(a)Spectrally resolved momentum space image of the PL from a 0D cavity,which shows discrete LP modes and an UP mode. To clearly show the UP mode, the intensity of the upper panel is magnified by 40× compared to the lower panel. The straight red line at 1.551 eV corresponds to the independently measured exciton energy. The other solid lines are the calculated dispersions of the LP, UP and uncoupled cavity. The white dashed lines and the crosses (×) mark the position of the calculated discrete LP and cavity energies, respectively. (b) Spectrally resolved momentum space images of the exciton PL, measured from the unprocessed part next to the SWGDBR cavity. (c) Spectrally resolved real space image of the PL from the 0D cavity, showing the spatial profile of the discrete LP modes.

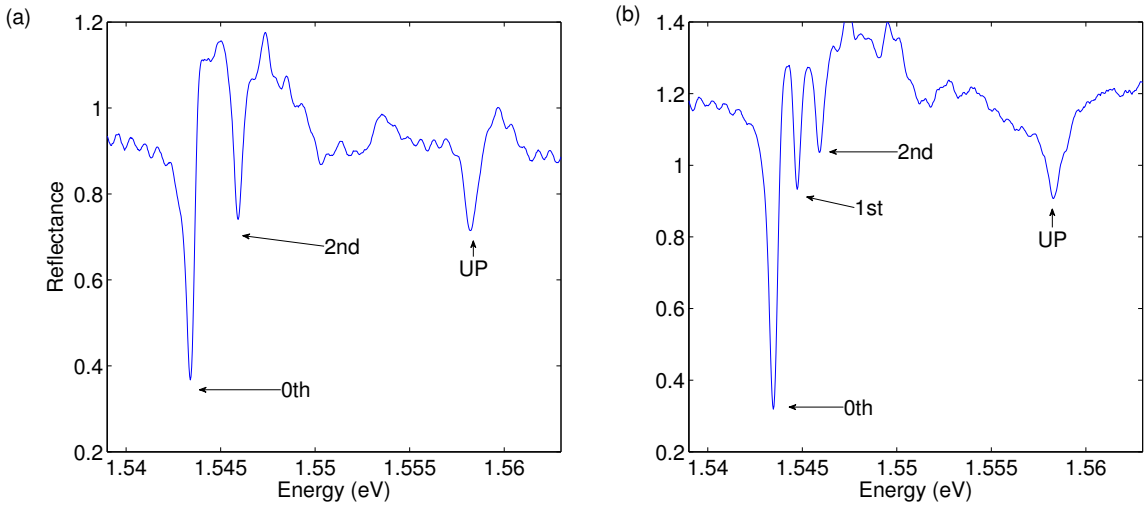

Figure 5.4: Reflectance spectra of the 0D cavity measured from (a) the normal direction and (b) 3.5 degree from the normal direction, both with an angular resolution of 0.276 degree.

The spatial profiles of the confined LP modes were also measured via spectrally resolved real space imaging, as shown in Figure 5.3(c). The four lowest LP modes are well confined within the SWG region, while the higher excited states are spread outside and form a continuous band. The variances of the k-space and x-space wavefunctions along the detected direction are $\Delta k = 0.85\mu m$ and $\Delta x = 1.01\mu m$. Their product is $\Delta x \times \Delta k = 0.86$, slightly larger than the uncertainty limit of 0.5, which may be due to the diffusion of the LPs.

The absorption spectra of the modes were obtained via reflectance measurements. The spectrum measured normal to the sample (Figure 5.4 (a)) shows the three symmetric modes with the lowest mean in-plane wavenumber: the UP ground state, the LP ground state and the second LP excited states. The spectral weights of the other polar- iton states are too small to be measured in reflectance. When measured at 3.56 from the sample normal, the first excited state of the LPs was also observed

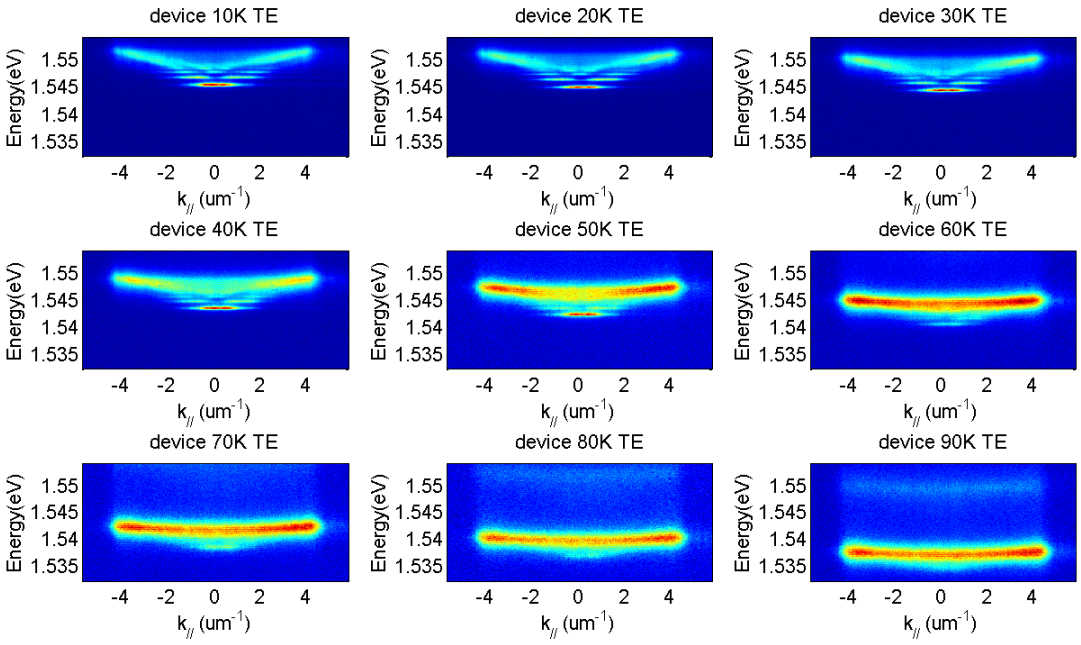

Figure 5.5: The PL signals of LP from the 0D device at temperatures from 10K to 90K

(Figure 5.4 (b)).

5.3.3 Temperature Dependence Property of 0D SWD Polariton Device

A further confirmation of the strong-coupling regime is the temperature tuning of the resonances.

The PL signals of the LP from the device and exciton from the planar part of the sample are measured at different temperatures from 10K to 90K. These measurement results are shown in Figure 5.5 and Figure 5.6.

Since we can not directly measure the cavity resonance due to the strong coupling effect between the exciton and the cavity photon, we measured the side-dips energy shift as a function of the temperature. It is an direct indicator for the cavity resonance shift due to the same shifting trend between the cavity resonance and the side-dips in

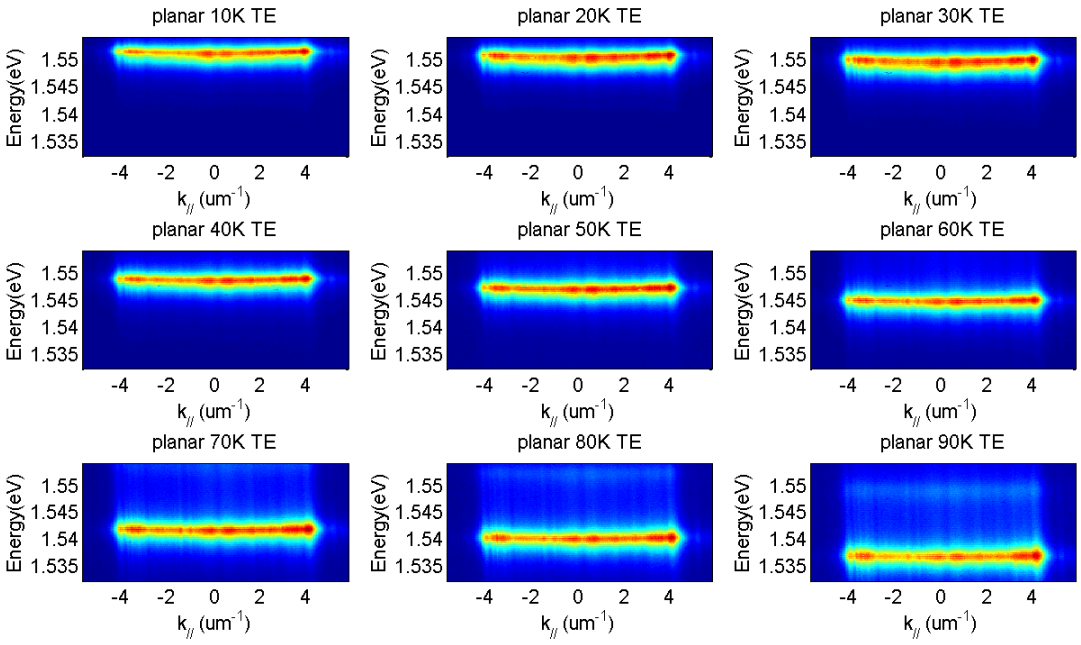

Figure 5.6: The PL signals of excitons from the planar part of the sample at temperatures from 10K to 90K

the reflection spectrum. The temperature dependent reflection measurement results are shown in Figure 5.7.

For LP energy, we use the ground state energy throughout the temperature variation from Figure 5.5; For the cavity resonance dependence, we use the energy of the cavity resonance at 10K plus the energy shifting from the side-dips at various temperatures in Figure 5.7. Also we convert the wavelength in Figure 5.7 to energy unit eV in Figure 5.8.

The summary of graph of the temperature dependence for LP, exciton and cavity resonance is shown in Figure 5.8. As the temperature increased, the LP and UP ground state energies were redshifted and were measured via k - space photoluminescence. The exciton energy was directly measured in the planar region outside the SWG. The shift of the cavity photon energy was obtained from the shift of the first low-energy side minimum of the stopband. Anticrossing of the LP and UP modes is evident.

The calculated the coupling strengths at difference temperatures are also shown in Figure 5.9. From the LP, exciton and cavity energies, we obtain a coupling strength of $2\hbar\Omega(T) \sim 10meV$ from 10 K to 80 K, showing that strong coupling persists to the liquid nitrogen temperature and higher.

5.3.4 Polarization Property of the SWG Polariton Device

Unlike planar DBRs, the grating breaks the in-plane rotational symmetry. As a result, the SWG mirrors can have high polarization selectivity. We optimized our SWG to have high reflectance for the TE mode and low reflectance for the orthogonal TM mode. Correspondingly, the polaritons are TE-polarized, while the TM- polarized excitons remain in the weak coupling regime. Figure 5.10 shows the

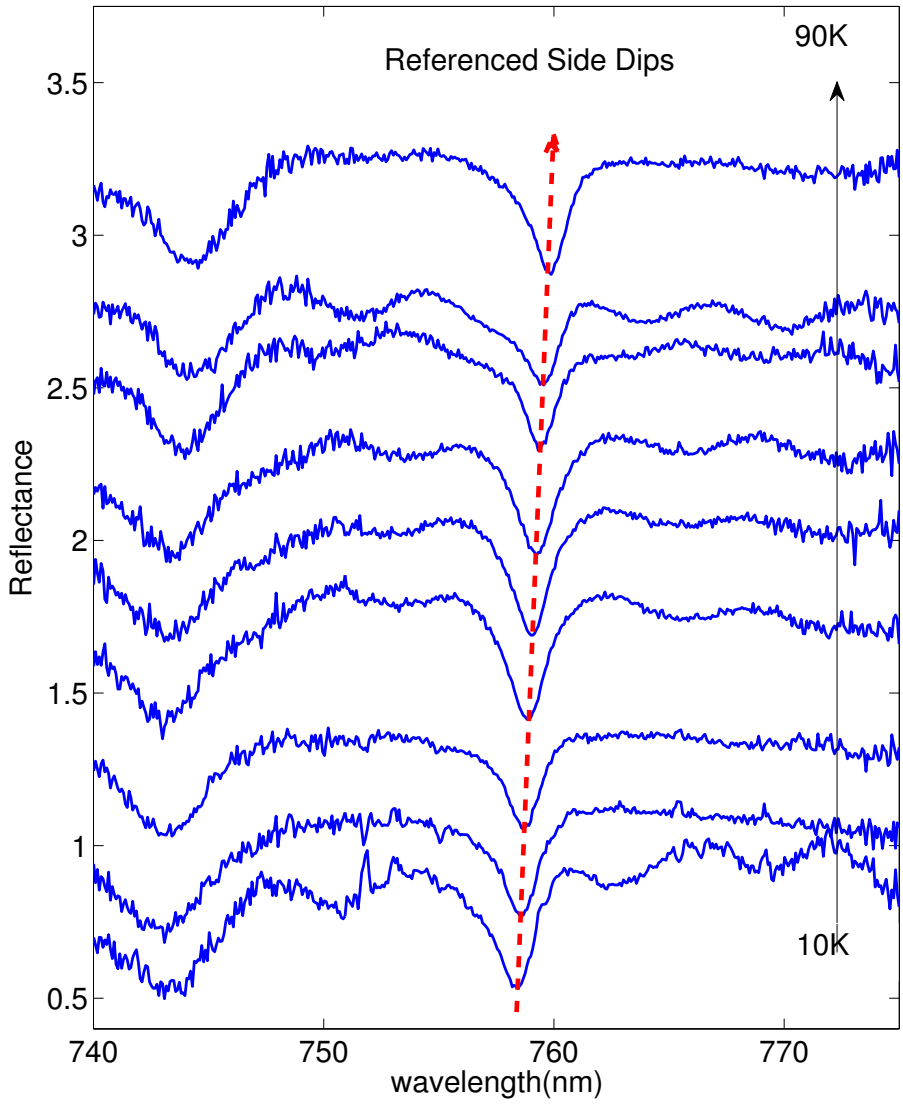

Figure 5.7: The reflection spectra from the planar part of the sample at temperatures from 10K to 90K

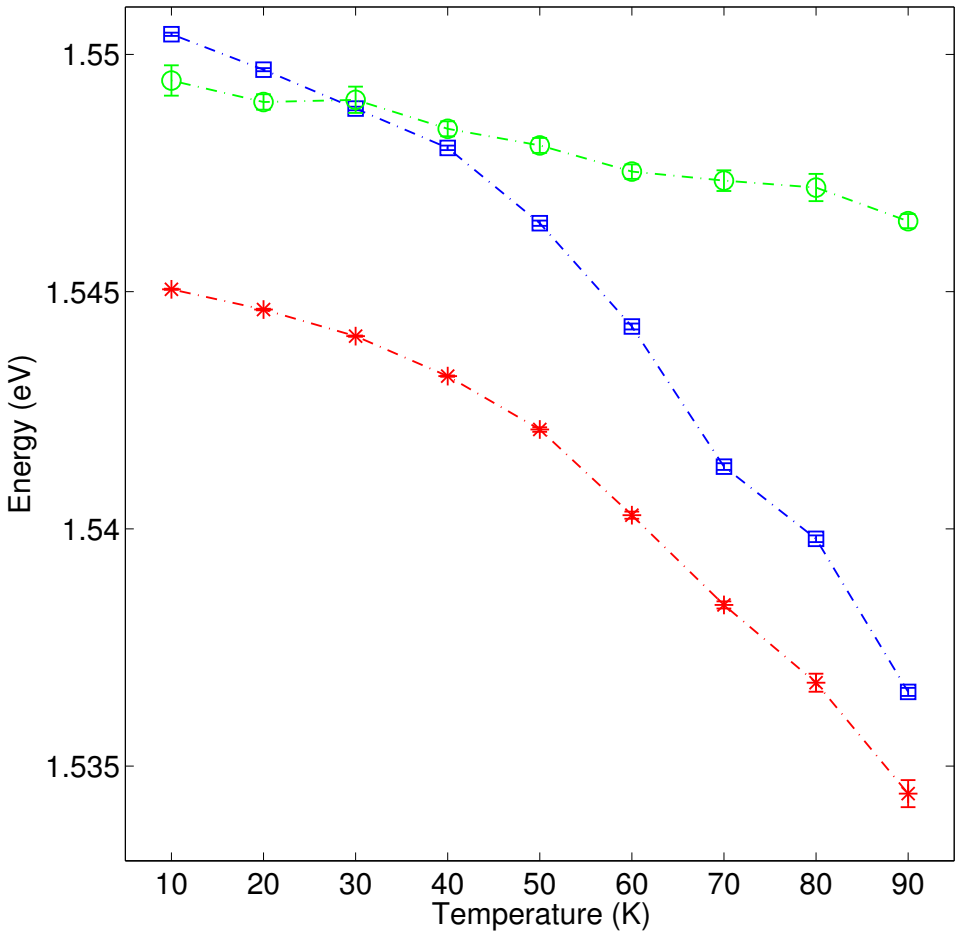

Figure 5.8: The summary graph of temperature dependence of the LP (stars), exciton (squares) and cavity resonances (circles).

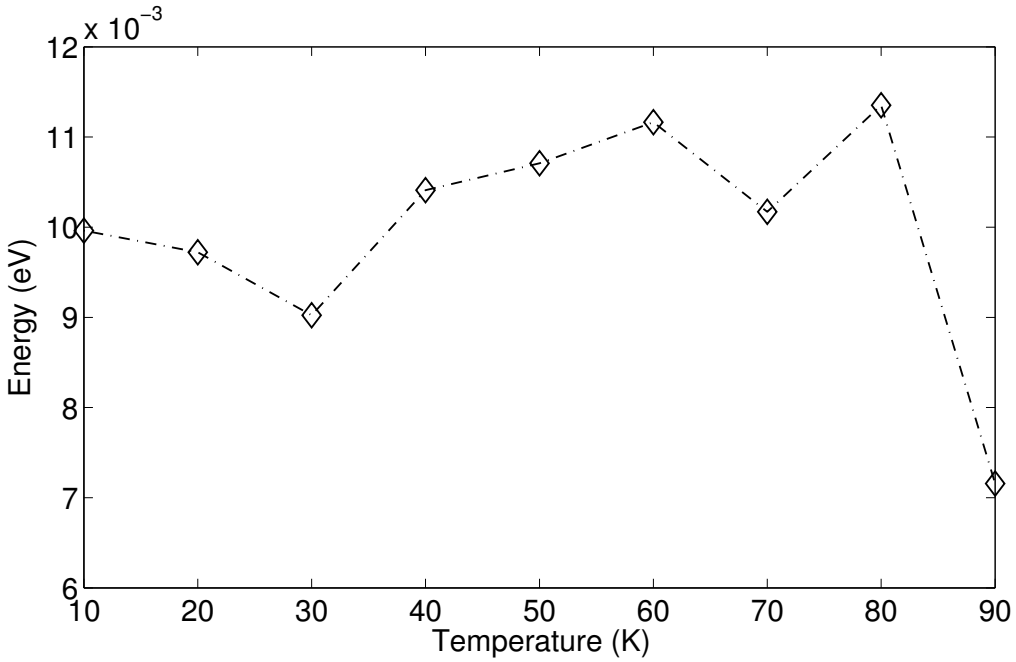

Figure 5.9: The calculated coupling strength at various temperatures from 10K to 90K

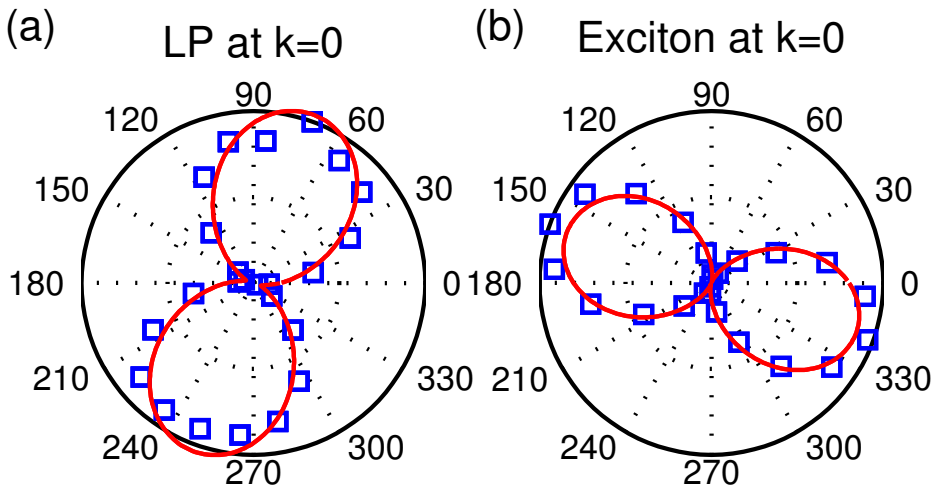

Figure 5.10: Polarizations of the polaritons and excitons in the hybrid-cavity polariton system. (a) Polar plots of the LP ground state intensity as a function of the angle of the linear polarization analyzer. The symbols represent the data. The solid lines fit to Equation 5.2, with a corresponding fitted linear degree of polarization of 91.9%. (b) Polar plot for the exciton emission intensity from within the SWG, corresponding to a fitted linear degree of polarization of 98.2%, with orthogonal polarization compared to (a)

photoluminescence intensity vs. the angle of linear polarization for the LPs and excitons at $k \sim 0$ within the SWG region, normalized by the maximum intensity. We fit the data with,

$$I = Acos(\theta - \Phi)^2 + B \tag{5.2}$$

where the fitting parameter w depends on the orientation of the device, A corresponds to linearly polarized light, and B corresponds to a nonpolarized background. Correspondingly, the degree of linear polarization is:

$$DOP = \frac{I_{max} - I_{min}}{I_{max} - I_{min}} = \frac{A}{A + 2B}. \tag{5.3}$$

We obtained $A_{LP} = 1.04 \pm 0.04$, $B_{LP} = 0.05 \pm 0.01$, $\Phi_{LP} = 71 \pm 1$ and $DOP = 91.9\%$ for the LPs, confirming that the LPs are highly TE-polarized. For the excitons, we obtained $A_{exc} = 0.891 \pm 0.001$, $B_{exc} = 0.0081 \pm 0.0002$, $\Phi_{exc} = 161 \pm 1 = \Phi_{LP} + 90$, $DOP = 98.2\%$, showing that the excitons are polarized orthogonal to the LPs. Such control of the polariton polarization has not been possible with conventional DBRDBR cavities and is unique to the SWG-based cavity.

5.4 Lasing in 0D SWG Polariton Device

In this section, we show that polariton lasing was achieved in the 0D hybrid cavity. We continued to use the same pumping condition as the previous PL optical characterization and continuously increased the excitation power. The PL signal

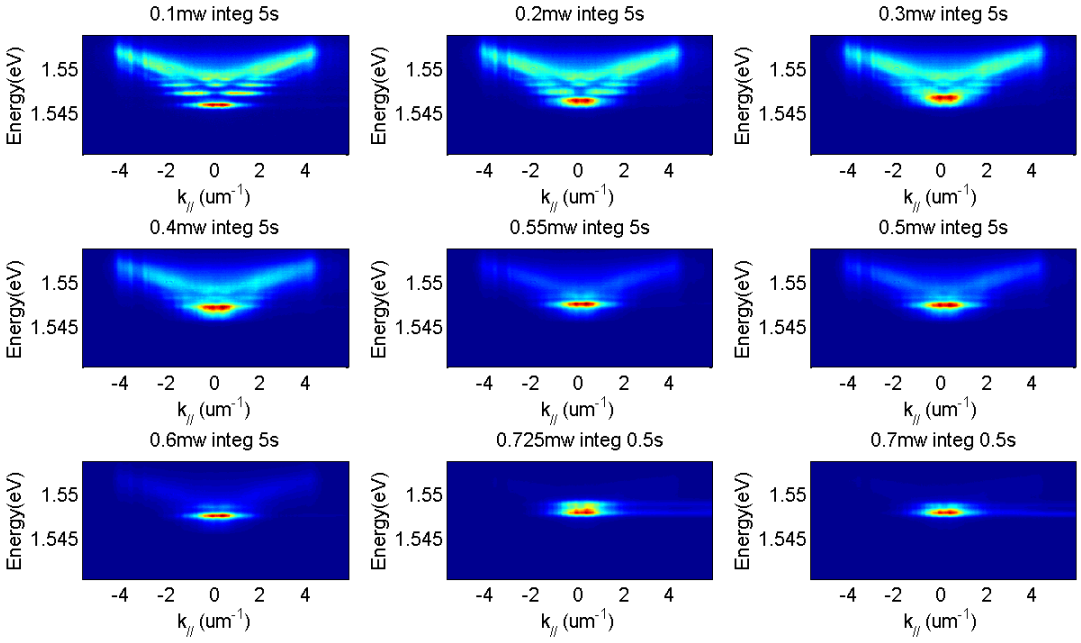

Figure 5.11: 0D SWG polariton device spectra with excitation power from 0.1mW to 0.7mW

from the device shifts from multiple discrete modes to single mode accompanying the increased PL intensity. This phenomena was captured in the following spectra figure at nine different pumping powers. (Figure 5.11)

The summary and analysis of the the lasing phenomena are presented in Figure 5.12. As shown in Figure 5.12(a), the emission intensity I from the LP ground state increases sharply with the excitation power P at a threshold of $P_{th} =\sim 5kW/cm^{-2}$, characteristic of the onset of lasing. Interestingly, the emission intensity I varies with P quadratically both below and well above the threshold, except at very low excitation densities. This result may arise because the energy separation between the discrete modes is larger than $k_BT \sim 0.8meV$. As a result, relaxation to the ground state through LP- phonon scattering is suppressed compared to LP - LP scattering.

Accompanying the transition, a sharp decrease in the LP ground state linewidth

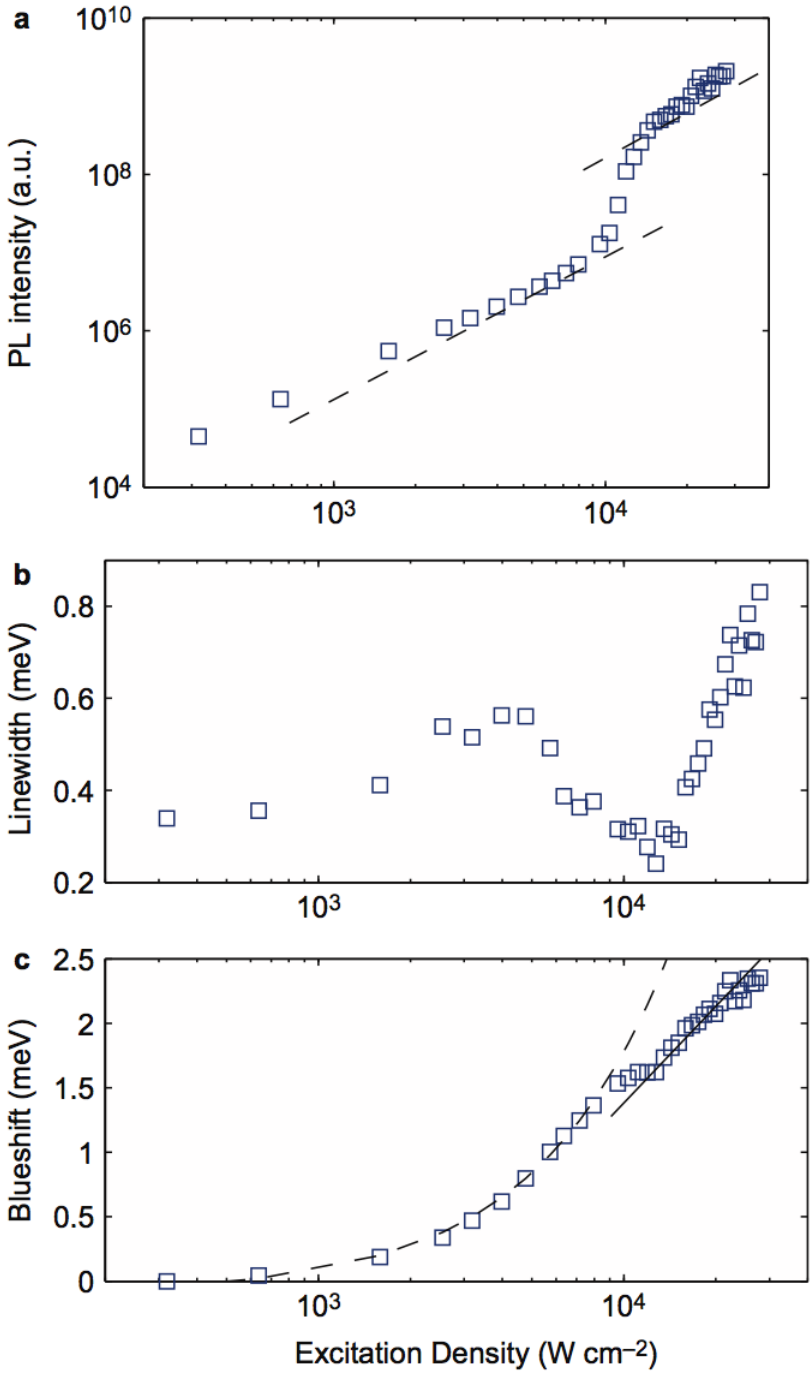

Figure 5.12: Lasing properties of the 0D polaritons. (a) Integrated intensity, (b) linewidth and (c) corresponding energy blueshift of the LP ground state vs. the excitation density. The dashed lines in (a) provide a comparison with quadratic dependence. The dashed lines in (c) display comparisons with the linear dependence below the threshold and logarithmic dependence above the threshold. 0D, zero-dimensional; LP, lower polariton; PL, photoluminescence.

was measured. The minimum linewidth of 0.24 meV may be primarily limited by the intensity fluctuation of the pulsed excitation laser [8]. The LP energy increased continuously with the excitation density due to excitonexciton interactions. The blueshift shows a linear dependence below the threshold, is suppressed near the threshold, and shows a logarithmic dependence above the threshold [52] [43]. The discrete energy levels are maintained across the threshold and remain distinct below the uncoupled cavity energy.

The establishment of polariton lasing confirms the quality of the 0D polariton system. The threshold density is smaller than or comparable to those measured in DBR - DBR pillar cavities [52] [77]. The linewidth reduction and blueshift are all within an order of magnitude of reported values in DBR - DBR planar or pillar microcavities [73] [52] [77]. Unlike DBR - DBR cavities, however, the polariton lasing demonstrated herein occurs with a *priori* defined polarization, independent of the excitation conditions.

CHAPTER VI

Magnetic Properties and Coherent Properties of 0D SWG Polariton Device

6.1 Magnetic Properties of 0D SWG Polariton Device

Since a polariton condensate or polariton lasing shares many similarities with a microcavity photon laser, it is important to establish criteria how to unambiguously distinguish the two phenomena. Here in this section, we utilize the interaction with external magnetic fields to quantify the matter content of a polariton laser which would not be possible for a photon laser due to the lack of the matter part.

When an external magnetic field is applied to a semiconductor exciton system, the energy of the exciton can be written as

$$E(B) = E_0 + \gamma_1 B + \gamma_2 B^2 + \ldots\ldots \tag{6.1}$$

Where E_0 is the exciton's original energy, B is the external magnetic field. The linear term of $\gamma_1 B$ is the Zeeman effect. It is corresponding to the two spin polarizations of the exciton state which can be detected and distinguished by light with two circular polarization in optical characterization. Since the SWG devices feature predefined linear polarization, we cannot observe the Zeeman splitting from the devices in external magnetic field.

In Equation 6.1, the second term $\gamma_1 B^2$ is diamagnetic energy shift. As can be seen is in quadratic relation with the external magnetic field intensity and can by simply characterized by the intrinsic material property, the diamagnetic coefficient γ_2. Since polariton is partially composed of exciton, the energy shift of the polariton is in proportion to the exciton component.

A different device from the one in Chapter **??** is used to demonstrate the diamagnetic properties of the polariton system. This device is with dimension $5\mu m \times 5\mu m$. The initial optical characterization, power dependent features and polariton lasing/condensation can be reproduced in this device which are also shown in Figure 6.1 and Figure 6.2.

Ti-Sapphire laser (spot size of $4\mu m$). The excitation wave- length of the laser is set to be about $\sim 80meV$ above the lower polariton energy, and the pulse width of the laser is about $\sim 4ps$ with a repetition rate of 82 MHz. The sample is held at $T = 6K$ in a helium flow cryostat. The selected device comprises a detuning between microcavity photon energy $\delta = E_{cavity} - E_{exc} = -7meV$.

In order to directly verify the persistence of the strong coupling above the lasing threshold, we study the interaction of the laser mode with the magnetic field (applied in Faraday configuration). In Figure 6.3, we plot spectra extracted from $k_{//} = 0$ for magnetic fields between $B = 0T$and $B = 5T$, recorded above the nonlinearity threshold at $P = 1.4P_{th}$. The asymmetric shape of the emission peak is due to the pulsed excitation scheme [20] as a result of the time integrated measurement. With increasing magnetic field, the peak energy of the system successively shifts towards higher energies. As we will show in the following, this shift can directly be connected to the diamagnetic shift of the QW exciton emission band, which is given by

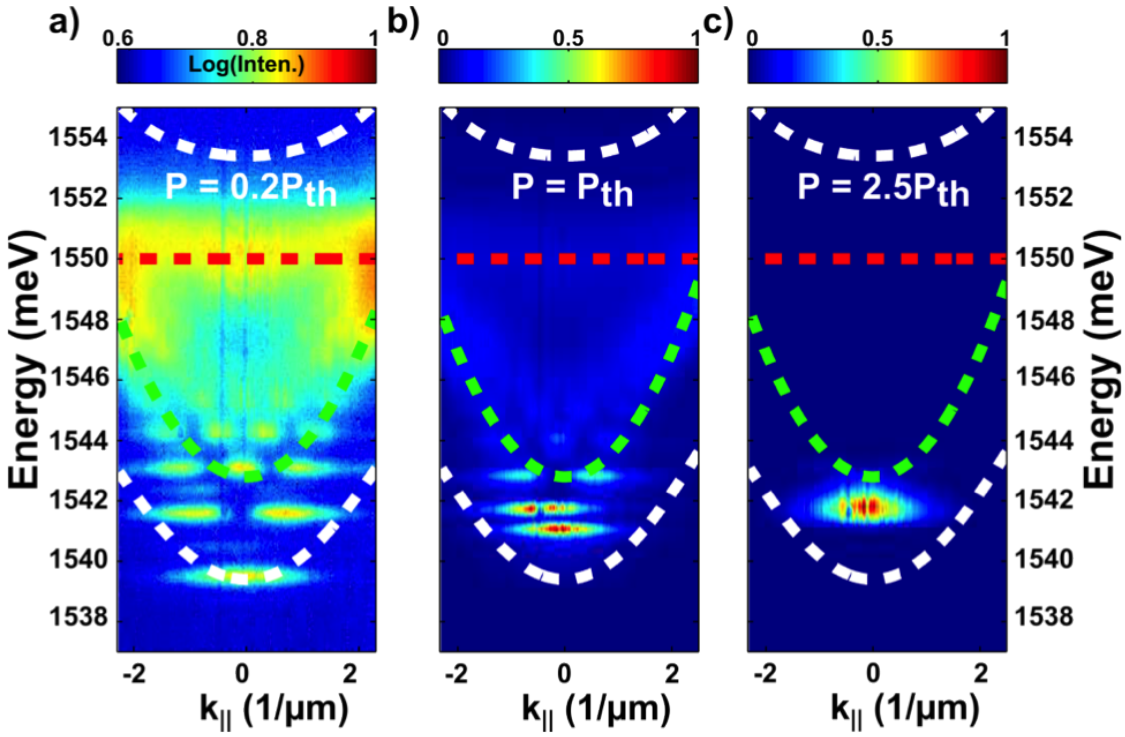

Figure 6.1: (a)(c) Energy-momentum dispersions of a $5\mu m$ large high index contrast grating structure at a detuning of $\delta E = 7meV$. The white dashed lines are indicating the lower and upper polaritons, the red dashed line the exciton, and the green dashed one the photon energy. (a) Well below the non-linearity threshold at $P = 0.2P_{th}$, the zero-dimensional resonances are clearly visible confirming the 3D confinement of the structure. (b) At the threshold $P = P_{th}$, the ground state energy is slightly blueshifted and becomes more and more intensive. Above threshold (c) at $P = 2.5P_{th}$ only the ground state is observable. The emission occurs well below the photon energy (green dashed line) indicating that strong coupling is preserved.

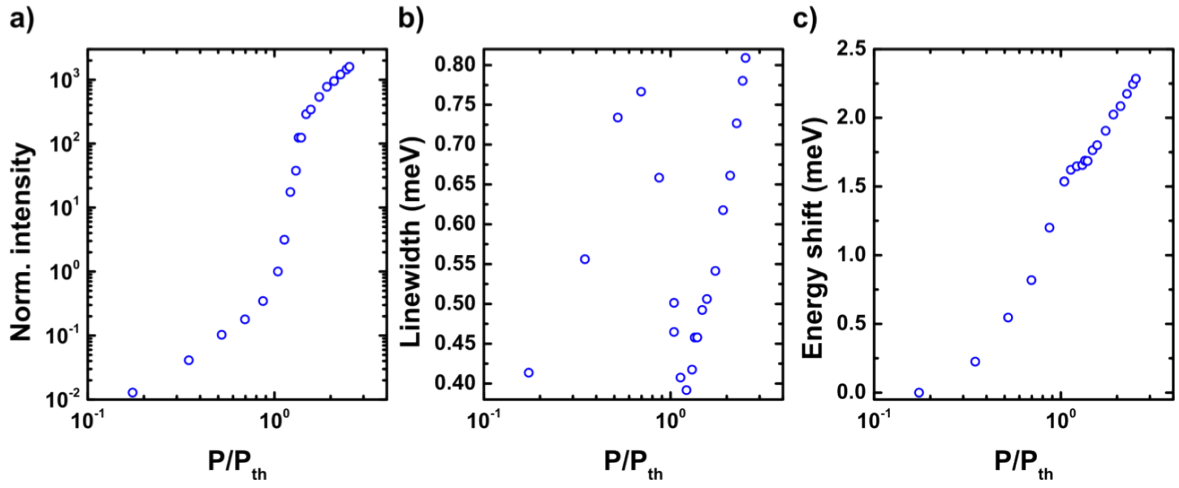

Figure 6.2: (a) Input-output curve and (b)power dependent linewidth trace of the ground state emission. Slightly above threshold, the linewidth narrows down to 0.391 meV (smaller than for low excitation powers). (c) Energy peak position versus excitation power. All the values are extracted from the momentum-space spectra by integrating around $k_{//} = 0$ with $k_{//} = \pm 0.15 \mu m^{-1}$

$$\Delta E_X = \kappa_X B^2 \tag{6.2}$$

Here, κ_X is the diamagnetic coefficient of the QW exciton. For comparison, the diamagnetic shift of the bare QW exciton, recorded under low excitation powers is shown in Figure 6.3(b). As expected, the QW exciton emission is also subject to a blueshift in the presence of a magnetic field, however, with a significantly larger magnitude. In contrast to a standard microcavity composed of two DBR segments, we can directly probe the uncoupled QW luminescence simply by moving the collection spot a few μm away from the SWG, hence allowing for a high degree of comparability. In Figure 6.4, we plot the peak position of both the emission features from the coupled and the uncoupled system as a function of the magnetic field. The diamagnetic coefficient of the QW exciton which amounts to $\kappa_{X,lowP} = 57 \mu eV/T^2$ is determined

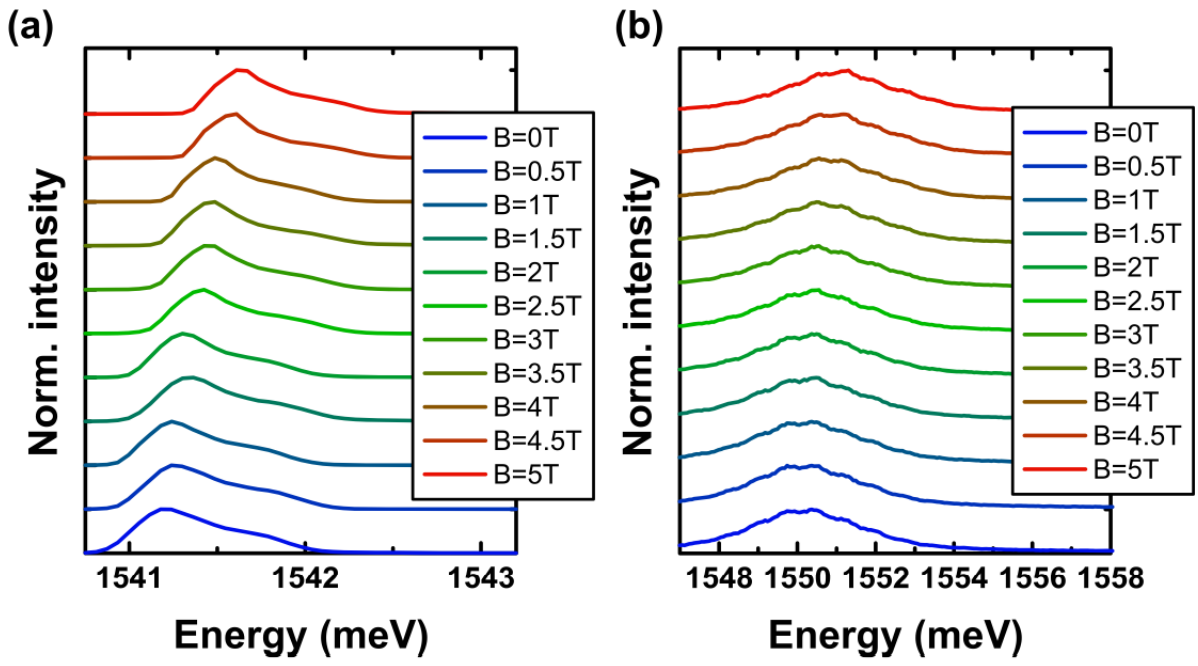

Figure 6.3: Line spectra from the momentum-space images for the dif-ferent magnetic fields from $B = 0T$ to $B = 5T$ at an excitation power of $P = 1.4P_{th}$ for (a) the polariton condensate and (b) the uncoupled QW exciton.

straight forwardly by fitting the data with Equation 6.2. In order to theoretically reproduce the diamagnetic shift of the polariton condensate, we have to extend the simple expression Equation 6.2 by including the effects of light-matter hybridization via a polariton Hopfield coefficient $|X(\kappa_X, B, E_{RS})|^2$. The latter characterizes the degree of light-matter hybridization in the system

$$\Delta E_{Dia,LP} = |X(\kappa_X, B, E_{RS})|^2 \kappa_X B^2 \tag{6.3}$$

For the detuning of our device d $\delta = -7meV$ and the Rabi- splitting of $E_{RS} = 12meV$, the matter part in our device amounts to $|X|^2 = 0.24$ at 0 T.

When a magnetic field is applied, the exciton-photon detuning changes, and the

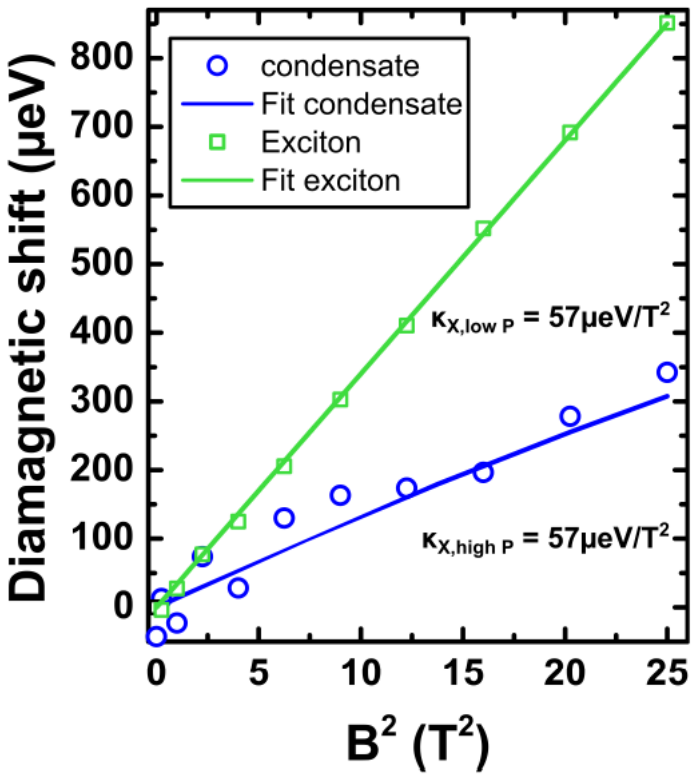

Figure 6.4: Comparison between the diamagnetic shift of the bare quantum well exciton (green squares) and the diamagnetic shift of the polariton condensate (blue dots).

Rabi-splitting increases as a result of an increased exciton oscillator strength[21]. Consequently, the Hopfield coefficient becomes a function of the magnetic field and reads

$$|X(\kappa_X, B, E_{RS})|^2 = \frac{1}{2}(1 + \frac{E_C - (E_X + \kappa_X B^2)}{\sqrt{(E_C - (E_X + \kappa_X B^2))^2 + (E_{RS}(B))^2}}) \tag{6.4}$$

By assuming approximately a linear increase of the Rabi- splitting from $E_{RS} = 12meV$ to $E_{RS} = 12.5meV$ between 0T and 5T, we can fit the data of the polariton condensates diamagnetic shift in Figure 6.4 by combining Equations 6.3 6.4.

This allows us to determine the diamagnetic coefficient κ_X of the QW exciton from the polariton condesate's diamagnetic shift at $P = 1.4P_{th}$ (see Figure 6.4, red solid line) to $\kappa_{X,highP} = 57\mu eV/T^2$ which is in perfect agreement with the bare exciton shift at low excitation power. This confirms that the model Equation 6.3 and the assumptions for the change of the detaining and the Rabi-splitting with magnetic field are well justified. More importantly, it directly evidences the matter contribution in our system and justifies the attribution to a polariton condensate. Indeed, for a polariton laser system close to the Mott transition, an increase of the diamagnetic coefficient with increasing exciton densities could be expected as a result of excitonic screening effects. Since our analysis confirms that such an effect can be neglected in our experiment, we conclude that our low dimensional SWG laser is not only operated in the strong light-matter coupling regime but also significantly below the transition to the weak coupling crossover.

6.2 Coherent Properties of the 0D SWG Polariton Device

In quantum optics, the statistical property and coherence property are characterized by using the correlation function. The photon statistical properties are characterized by using the second order correlation function. The second order correlation function with time delay τ is:

$$g^{(2)}(\tau) = \frac{< a^{\dagger}(0)a^{\dagger}(\tau)a(\tau)a(0) >}{< a^{\dagger}a >^2} \tag{6.5}$$

where $a^{\dagger}$ and a are the creation and annihilation symbol for particles. The second order correlation function with zero time delay can be subsequently written as:

$$g^{(2)}(0) = \frac{< (a^{\dagger})^2 a^2 >}{< a^{\dagger}a >^2} \tag{6.6}$$

The second order coherence properties of the polariton condensate or polariton laser has been extensively researched for the two dimensional polariton systems. [8][2]. Yet it has been suffering one major problems that none of these polariton condensates or polariton lasers are truly coherent with $g^{(2)}(0) = 1$. This has been shown with $g^{(2)}(0)$ signals not reaching 1 while the condensates happen or even $g^{(2)}(0)$ reaches 1, but subsequently deviate from 1 with higher excitation power for the system.

For our polariton system, it is tightly confined from all three directions. Hence, we have discretized modes for the polariton system. While we reach the lasing threshold, the polarities all condense to single ground state mode. This has been demonstrated from the previous optical characterization chapter and also in the magnetic property

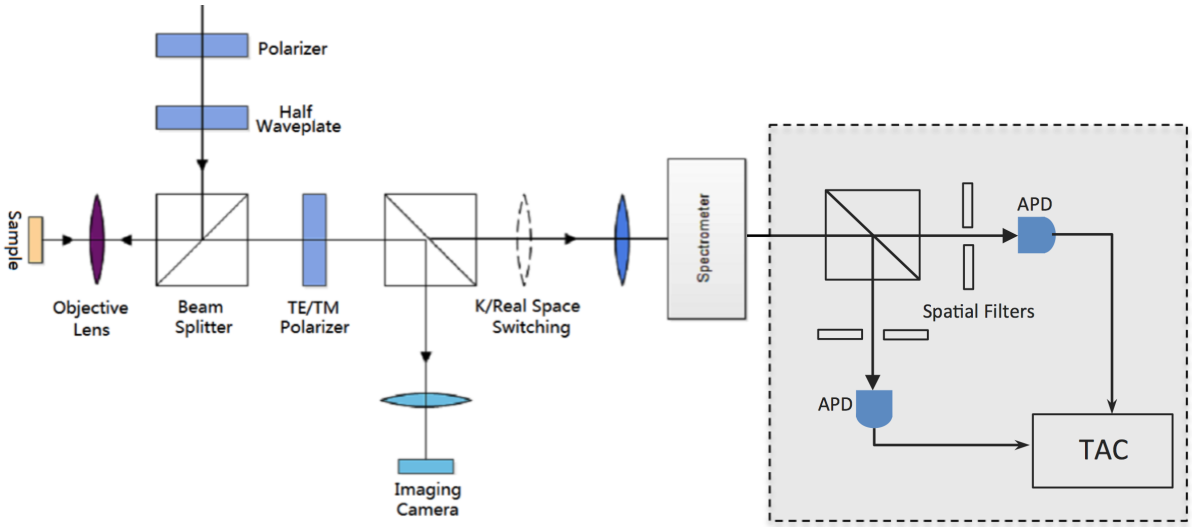

Figure 6.5: The updated optical characterization setup for $g^{(2)}(0)$ measurement. The dashed line shading area is the HB-T setup

section in this chapter. To further characterize this single mode lasing property, we also did the $g^{(2)}(0)$ measurement.

To realize the $g^{(2)}(0)$ measurement, we also use the Hanburry Brwon - Twiss (HB-T) set up with filtered polariton signal. Compared to the original optical characterization set up in Figure 5.2, the updated $g^{(2)}(0)$ set up utilizes the spectrometer to do the polariton ground state signal filtering in spectroscopy. Then the filtered signal is directed into two avalanche photon detectors (APD) with 40ps time resolution which are connected to the time-to-amplitude converter (TAC). The TAC is connected to multi-channel analyzer which records the photon counts in histogram between the start and stop time. This set up is shown in Figure 6.5

The $g^{(2)}(0)$ measurement results are shown in Figure 6.6. As can be seen, due to the thermal state property below threshold, emission with a bunching effect was expected with a maxmium of $g^{(2)}(0) = 1.35$ is measured. While the pumping power is above the threshold, $g^{(2)}(0)$ signal abruptly drops to 1, indicating a pure second

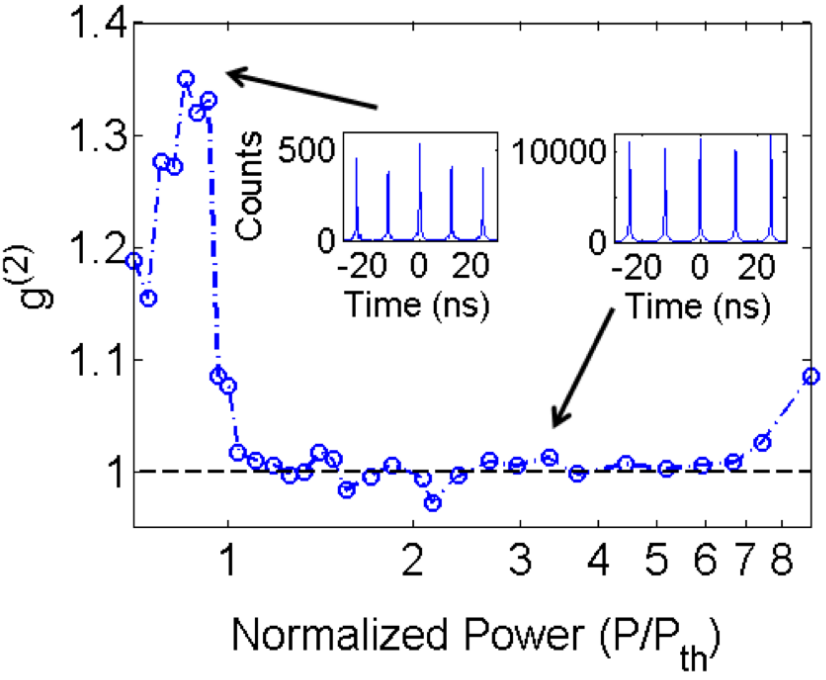

Figure 6.6: Second order correlation $g^{(2)}(0)$ as a function of normalized pumping power. Inset: The number of coincidence counts as a function of τ

order coherent state formed for lower polariton ground state while lasing. Because of the strong scattering processes between LPs at extreme high pumping power, $g^{(2)}(0)$ starts to increase.

In summary, based on this $g^{(2)}(0)$ measurement, we can see we have very good quality of a single mode LP laser from the 0D SWG-based polariton device, attributing to the tight confinement. The pure coherence of $g^{(2)}(0) = 1$ has been maintained for a large range of pumping power above the lasing threshold.

CHAPTER VII

Decoupled, Coupled and One Dimensional SWG Polariton Devices

The polariton system also provide an accessible venue for research on lattice physics [16] [33] and quantum optical circuits[32] [78] [34]. Along this line, we also construct de-coupled and couple polariton systems from the zero dimensional polariton quantum boxes.

The SWG-based polariton system not only can formulate the potential for the polariton systems, but also realize lower dimensional control. To realize the potential construction and probing an individual 0D system for a coupled-polariton system, here in this section, we introduce newly designed quasi-one dimensional SWG devices. These devices not only accomplish the effective potential control for the polariton system but also provide a 1D channel for polariton coupling.

7.1 Introduction: Surface Patterning Working Principle

To realize the coupling and dimensionality control for the confined polariton systems, we specifically designed surface patterns to surround the air-suspending gratings in different devices. These patterns will create different potentials for the cavity photons, through which we achieve the control for the polariton systems. For a

typical device surface pattern, it is composed of thorough-etched square holes and rectangular holes.

To create lower dimensional SWG-cavities, we first utilize the sudden change in the reflectance from the SWG region to the planar region surrounding it, which results in a large effective potential at the lateral boundaries of the SWG. To create additional potentials and to control the coupling among 0D SWG-cavities, we place through-etched long rectangular slots in the tether, which changes the boundary condition of the cavity and creates effectively potential barriers for the cavity modes. The potential is centered at the center of the slots, with its width and height controlled by the length of the slot. By arranging the positions and changing the lengths of the slots, we can create different effective potentials for the photon modes. In the strong-coupling regime, the photon potential is directly transcribed to the polaritons.

7.2 Uncoupled Polariton Systems

The first two devices have the same SWG of 7.5 μm in width and 30 μm in length, while different patterns in the tether create different potentials for the polaritons. In the first device, we create two separate 0D polariton quantum boxes by placing a pair of long slot of 8.5 μm in length, in the middle of both of the top and bottom tethers, as shown in the scanning electron microscopic (SEM) image in Fig 7.1(a). The resulting lower polariton (LP) modes were measured via spectrally resolved real space imaging, as shown in Fig 7.1(b). Two spatially separated groups LP modes were observed, with identical discrete energy levels. It suggests that the slots create a potential barrier, confining the LPs to two 0D quantum boxes on its two sides.

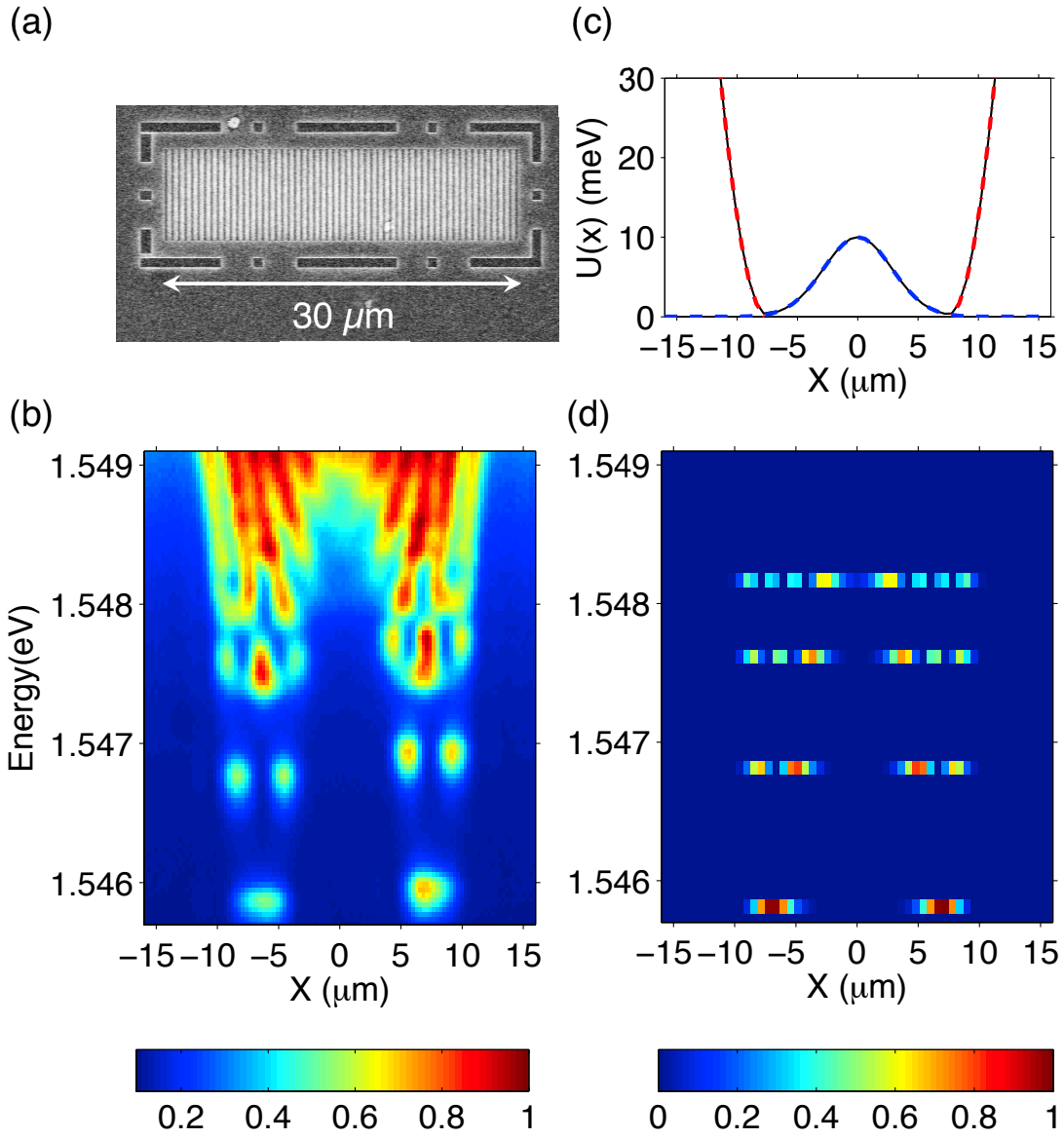

Figure 7.1: Two decoupled 0D polariton systems: (a) Device SEM image. (b) Real space spectroscopic characterization. (c) Effective photon potentials in the device. The black line − is the total potential. The blue dashed line indicates the Gaussian-shaped potential in the middle. The red dot-dashed line depicts the harmonic potential towards edges of the device. (d) Simulation results using the total photon potential.

We model the potential barriers created by the slots by Gaussian functions: $A * exp(\frac{x-x_0}{B})^2$. Here x is the position along the SWGs longer dimension measured from the center of the SWG. x_0 is given by the center of the slot. A and B correspond to height and width of the barrier, respectively, and are positively correlated with the width of the slot. For the long slot placed at the center of the wire, $x_0 = 0$, $A = 10$ meV and $B = 4$ μm. In addition, same as in Ref. [63], we model the effective harmonic potential at the two ends of the SWGs longer dimension as $U(x) = a(x-d)^2$. Here a=2meV, d=$\pm$7.2 μm, and. The total potential for the entire device is the sum of all the Gaussian barriers and edge harmonic potentials. The profile of each contributing potential and the total potential are plotted in Fig 7.1(c).

Using the total potential, we can first calculate the confined photon energy levels and the corresponding real space wave functions. Then the lower polariton energy levels can be calculated using Equation 3.22. The resulting polariton energy levels and the corresponding spatial wave functions are shown in Fig 7.1(d), which match very well the experimental results in Fig 7.1(b).

7.3 Coupled Polariton Systmes

In the second SWG device, we demonstrate coupling among three 0D polariton quantum boxes, using two closely spaced, narrower and shallower potential barriers instead of a wide one at the center. We achieve this with two shorter slots, 7 μm apart, as shown in the SEM image in Fig 7.2(a).

The resulting LP modes were shown by the spectrally resolved real-space images of the PL in Fig 7.2(b). Similar to the first device, the energy levels are discrete, showing the zero-dimensionality of each constituent quantum boxes. At the same

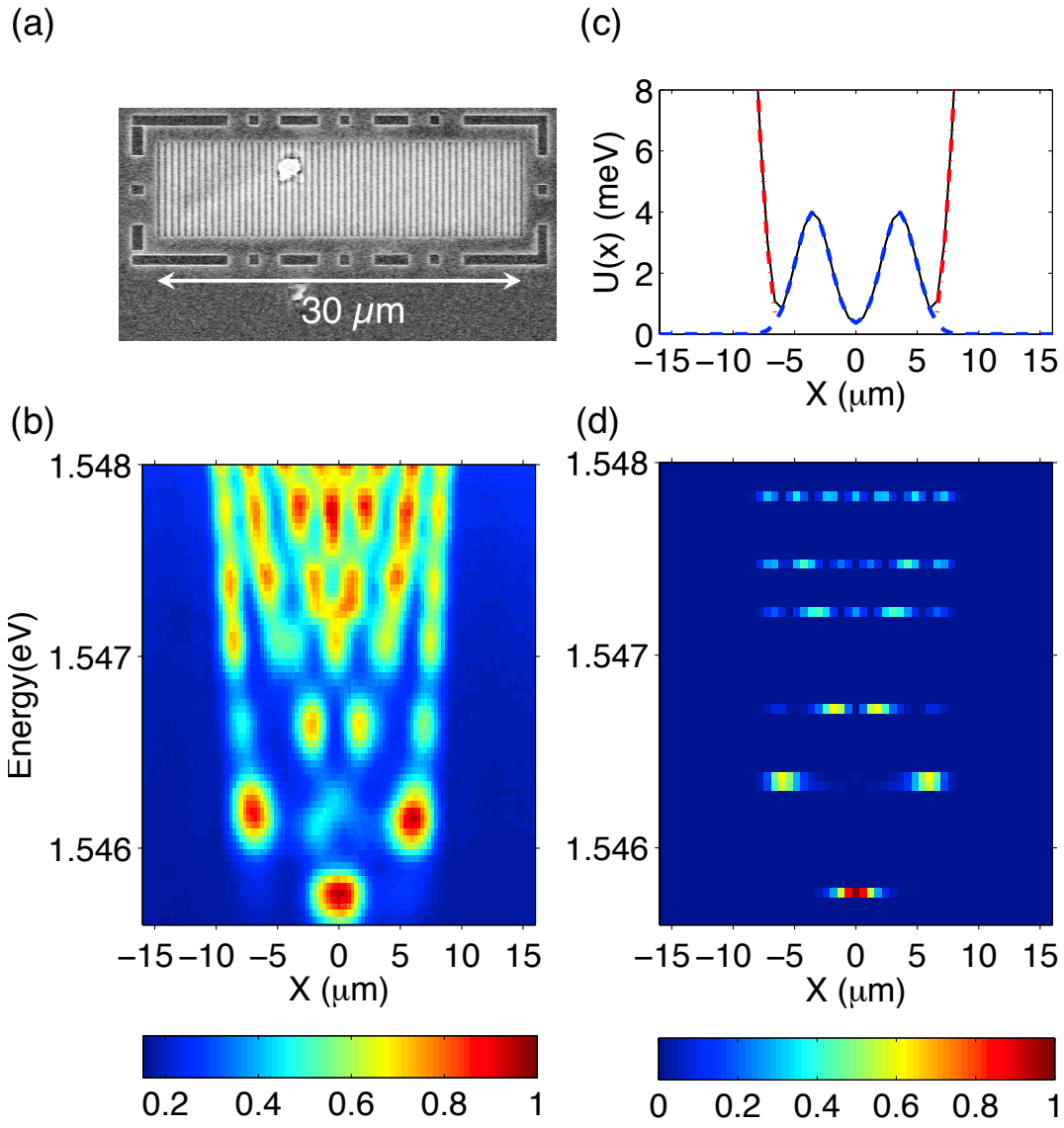

Figure 7.2: Coupled polariton systems from 0D polariton units: (a) Device SEM image. (b) Real space spectroscopic characterization. (c) Effective photon potentials: black line is the total potential; blue dashed line indicates the two shallow Gaussian barriers in the middle; The red dot-dashed line depicts the harmonic potential towards edges of the device. (d) Simulation results using the total photon potential.

time, unlike having separate groups of LPs in the first device, LPs show renormalized energy levels and distinct features resulting from coupling among the three quantum boxes, or, tunneling through the barriers. For example, there exists a common ground state at a lower energy than the ground states in the first device. The spatial wavefunction of the ground state doesnt have a node and peaks at the center of the device. The first and second excited states are very closely spaced in energy, different from either three uncoupled quantum boxes or an unmodulated quantum wire.

To model the potentials, we use the same method as for the first device. The same harmonic potentials are used towards the two ends of the wire. The same Gaussian function is use for the barriers created by the slots. The two main barriers are centered at $x_0 = \pm 3.5$ μm and with a smaller height and width given by $A = 4$ meV and $B = 2$ μm. Similar to Device 1, harmonic potential at the two ends of the SWG's longer dimension is $U(x) = a(x - d)^2$, with a=2 meV, d=$\pm$6.6 μm. Each of these potentials and the total potential are plotted in Fig 7.2(c). The calculated energy levels and corresponding wavefunction distributions based on the total potential are shown in Fig 7.2(d). Due to the shallower barrier and closer spacing of the potential wells, quantum tunneling between the potential wells is prominent. The ground state and the first several excited states of the coupled system match very well with the measured results in Fig 7.2(b).

In the first two devices, the same tether pattern is used at both the top and bottom of the SWG, which create potentials symmetric around the center of the SWG along its width. A higher potential barrier would require a longer slot, limiting the number of the potential barriers or the height of them for given length of the SWG-wire. Moreover, the height and width of the barrier are both fixed with a given slot width.

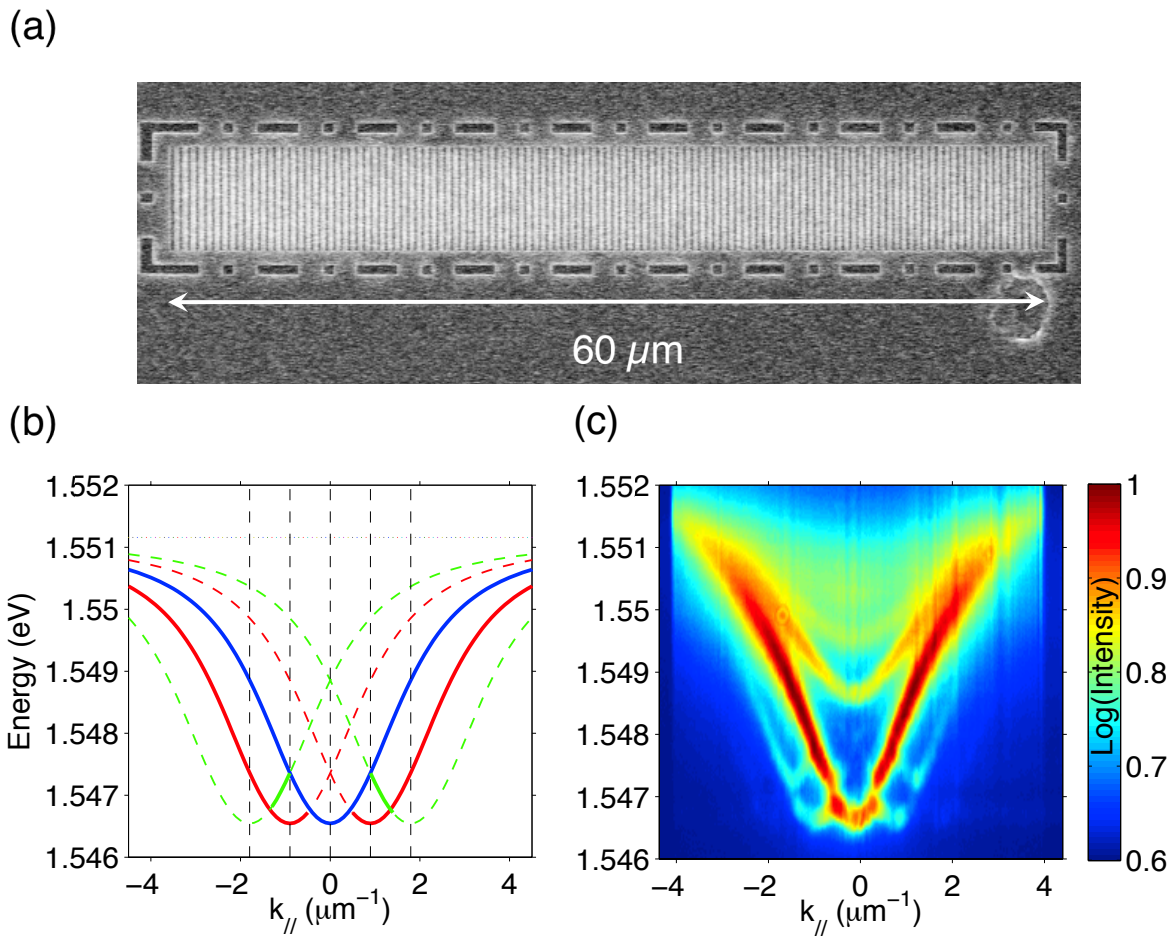

Figure 7.3: 1D polariton system: (a) Device SEM image. (b) Simulation results of dispersion relation in momentum space, based on device modulation periods of ∼7μm. (c) Momentum space spectroscopic characterization.

7.4 1D Polariton Lattice

We also implement a quasi-1D polariton lattice by extending the two coupled 0D polariton quantum boxes in the second device to eight coupled ones. We use a long SWG wire of 60 μm in length and create the periodic potential with periodic slot-pattern in the tether. The slots have a width of 3 μm, same as in the second device, and they are placed $\sim$ 7 μm apart. The SEM image of the device is shown in Fig 7.3(a). The energy-wavenumber dispersion of the LP modes is shown in Fig 7.3(c). Energy gaps can be identified at the edges of the 1st Brillouin zone

at $\pm\pi/7\mu m^{-1}$ and $2\pi/7\mu m^{-1}$, corresponding to the lattice constant of 7μm.Up to three LP dispersion curves can be measured in the repeated-zone scheme. At higher energies, additional branches are also observed due the one-dimensional nature of the wire. In Fig 7.3(c), we calculated the LP dispersion on a lattice in the extended zone scheme. The five vertical black dashed lines indicate the minima of the dispersion branches, with a period of $\sim 2\pi/7\mu m^{-1}$. Each crossing point of the dispersion branches corresponds to the edge of the Brillouin zones and separates different energy bands. The calculated dispersions compare well with the measurement.

7.5 Polariton Device with Arbitrary Potential Shapes

In the first two devices, the same tether pattern is used at both the top and bottom of the SWG, which create potentials symmetric around the center of the SWG along its width. A higher potential barrier would require a longer slot, limiting the number of the potential barriers or the height of them for given length of the SWG-wire. Moreover, the height and width of the barrier are both fixed with a given slot width. In this asymmetric device, we show that by combining different tether patterns at the top and bottom of the SWG, additional potential barriers can be created. Moreover, the barriers height can be adjusted independent from the width, enabling tall barriers with a narrow width. As shown in Fig 7.4(a), we place one long slot at the center of the top tether and two shorter slots at the bottom tether.

The resulting spectrally resolves spatial modes of the LPs are shown in Fig 7.4(b). The potentials are again modeled using the same method as before. Tentative potential modeling is demonstrated here. Since the bottom tether has the same pattern as in the first device, we use the same Gaussian potentials for the first device, but

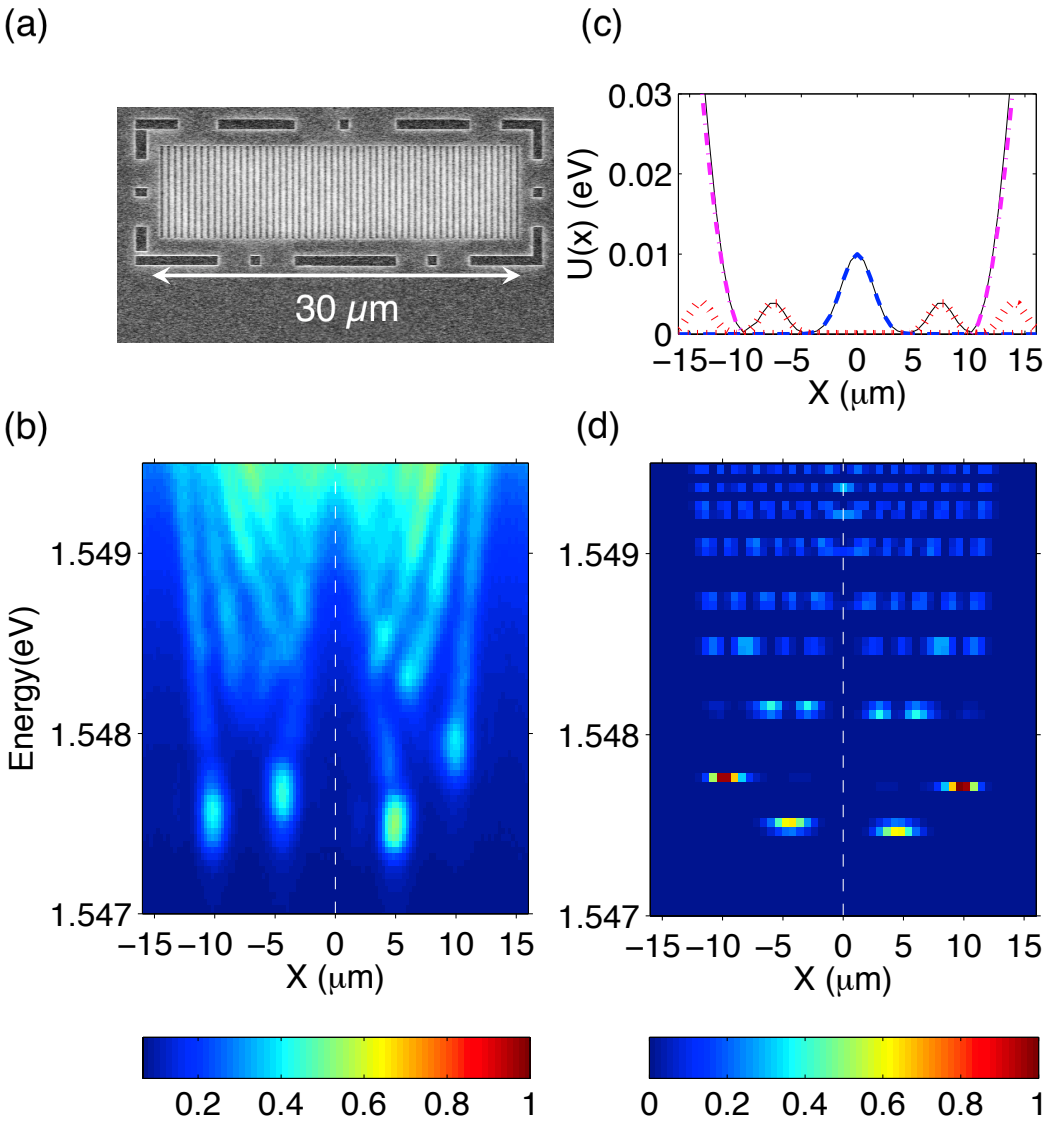

Figure 7.4: Coupling polariton system with designs of asymmetric surface patterns: (a) Device SEM image. (b) Real space spectroscopic characterization. (c) Effective photon potentials in the device. The black line − is the total potential. The blue dashed line indicates the Gaussian-shaped potential in the middle. The red dotted line is the Gaussian-shaped the potential with shorter bar-length. The magenta dash-dotted line depicts the harmonic potential towards edges of the device. (d) Simulation results using the total photon potential.

reducing the width B by half. Since the top two slots have the length between the longest slot in Device 1 and the shortest slot we see in Device 2, the A and B values chose to model these potentials will fall in between as well, A= 8meV and B= 3 μm. Compared to the symmetric devices 1 and 2, only one side was used, so these two values will also be reduced by half to A=4meV and B=1.5 μm. The total potential and constructing potentials are drawn in Fig 7.4(c) and simulation results are shown in Fig 7.4(d). The calculated results reproduce many of the major features of the measured results. In particular, the two spatially separated major branches on both sides of the device central axis are clearly seen. And the lowest energies match up as well.

CHAPTER VIII

Conclusion and Future Work

8.1 Conclusions

In this thesis, I have demonstrated the first series of hybrid cavities incorporating a mirror of sub-wavelength high contrast gratings. These cavities work at strong coupling regime which produce microcavity polaritons. Unique to SWG or HCG microcavity polaritons, they have pre-defined polarization. This adds extra control for the fundamental properties of polariton systems, which is impossible for the traditional DBR-DBR polaritons.

I have presented the dimensionality control using SWGs. The zero dimensional device in was demonstrated in Chapter V in which three-dimensional confinement was achieved. In Chapter VII, I have also introduced three devices which realized decoupled, coupled quantum-box polariton systems and Quasi-1D polariton systems, through different device surface patterning. I have introduced and characterized a quasi-one dimensional polariton device using the SWGs as well.

The zero dimensional system in Chapter V also presents prominent lasing properties. The signature nonlinear increase of the emission intensity, continuous energy blue shifting, and the decrease of the line-width at lasing were all clearly observed from the device.

By using the external magnetic field, I have demonstrated that the device lases at the strong coupling regime. The diamagnetic-shift observed from the zero dimensional device while lasing, clearly distinguish the polariton laser from the traditional photon laser. In addition, the 2nd order coherence characterization for the polariton laser further confirms the single mode lasing property, which was observed in polariton devices for the first time. Besides, the single-mode lasing maintained through a large range of pumping intensities up to 10 times of the excitation threshold.

The polariton devices using sub-wavelength grating mircocavities present efficient dimensionality and coupling control as well as macroscopic coherent states. Such properties are the essential components for solid-state quantum devices. SWG polariton devices presented in this thesis are building blocks for this ultimate goal.

8.2 Future Works

Due to the unique polarization properties of the SWG based polariton systems, we are able to realize the strong coupling in one particular linear polarization, while the cross-polarization still maintains at weak coupling regime. Such property provides the opportunity for direct probing of the exciton reservoir in the weak coupling regime simultaneously, while the properties in the strong coupling regime will not be disrupted. The origin of the energy shifting at high pumping density is expected to detect through the weakly coupled excitons.

As can be seen in Chapter VII, polariton systems with de-coupled and coupled properties were realized through the surface pattern design. In particular, the asymmetric surface pattern has extra freedom for control of the potential barriers. Further

investigation of the different surface designs, such as coupling strength or different modulation periods, will allow for various modifications of the polariton systems .

Since one way to control the cavity resonance for SWG device is through tuning the air gap below the gratings. We will be able to tune the cavity photon energy in one single device, if we can incorporate external mechanical control for the top layer of the device. So far the most promising way is through the static electrical field. Such properties of the device are expected to present more control for the polariton systems.

BIBLIOGRAPHY

BIBLIOGRAPHY

[1] Hui Deng and Yoshihisa Yamamoto. Exciton-polariton Bose-Einstein condensation. *Reviews of Modern Physics*, 82(2):1489–1537, May 2010.

[2] Hui Deng, Gregor Weihs, Charles Santori, Jacqueline Bloch, and Yoshihisa Yamamoto. Condensation of semiconductor microcavity exciton polaritons. *Science (New York, N.Y.)*, 298(5591):199–202, October 2002.

[3] J Kasprzak, M Richard, S Kundermann, a Baas, P Jeambrun, J M J Keeling, F M Marchetti, M H Szymaska, R André, J L Staehli, V Savona, P B Littlewood, B Deveaud, and Le Si Dang. Bose-Einstein condensation of exciton polaritons. *Nature*, 443(7110):409–14, September 2006.

[4] R Balili, V Hartwell, D Snoke, L Pfeiffer, and K West. Bose-Einstein condensation of microcavity polaritons in a trap. *Science (New York, N.Y.)*, 316(5827):1007–10, May 2007.

[5] Hui Deng, David Press, Stephan Götzinger, Glenn Solomon, Rudolf Hey, Klaus Ploog, and Yoshihisa Yamamoto. Quantum Degenerate Exciton-Polaritons in Thermal Equilibrium. *Physical Review Letters*, 97(14):146402, October 2006.

[6] Hui Deng, Glenn Solomon, Rudolf Hey, Klaus Ploog, and Yoshihisa Yamamoto. Spatial Coherence of a Polariton Condensate. *Physical Review Letters*, 99(12):126403, September 2007.

[7] J. Kasprzak, M. Richard, a. Baas, B. Deveaud, R. André, J.-Ph. Poizat, and Le Dang. Second-Order Time Correlations within a Polariton Bose-Einstein Condensate in a CdTe Microcavity. *Physical Review Letters*, 100(6):067402, February 2008.

[8] a. P. D. Love, D. N. Krizhanovskii, D. M. Whittaker, R. Bouchekioua, D. Sanvitto, S. Al Rizeiqi, R. Bradley, M. S. Skolnick, P. R. Eastham, R. André, and Le Si Dang. Intrinsic Decoherence Mechanisms in the Microcavity Polariton Condensate. *Physical Review Letters*, 101(6):067404, August 2008.

[9] K. G. Lagoudakis, B. Pietka, M. Wouters, R. André, and B. Deveaud-Plédran. Coherent Oscillations in an Exciton-Polariton Josephson Junction. *Physical Review Letters*, 105(12):120403, September 2010.

[10] Alberto Amo, Jérôme Lefrère, Simon Pigeon, Claire Adrados, Cristiano Ciuti, Iacopo Carusotto, Romuald Houdré, Elisabeth Giacobino, and Alberto Bramati. Superfluidity of polaritons in semiconductor microcavities. *Nature Physics*, 5(11):805–810, September 2009.

[11] a Amo, S Pigeon, D Sanvitto, V G Sala, R Hivet, I Carusotto, F Pisanello, G Leménager, R Houdré, E Giacobino, C Ciuti, and a Bramati. Polariton superfluids reveal quantum hydrodynamic solitons. *Science (New York, N.Y.)*, 332(6034):1167–70, June 2011.

[12] M. Abbarchi, a. Amo, V. G. Sala, D. D. Solnyshkov, H. Flayac, L. Ferrier, I. Sagnes, E. Galopin, a. Lemaître, G. Malpuech, and J. Bloch. Macroscopic quantum self-trapping and Josephson oscillations of exciton polaritons. *Nature Physics*, 9(5):275–279, April 2013.

[13] F. Tassone. Exciton-exciton scattering dynamics in a semiconductor microcavity and stimulated scattering into polaritons. *Physical Review B*, 22(16):389–10842, April 1999.

[14] D. Porras, C. Ciuti, J. Baumberg, and C. Tejedor. Polariton dynamics and Bose-Einstein condensation in semiconductor microcavities. *Physical Review B*, 66(8):085304, August 2002.

[15] Cristiano Ciuti, Gérald Bastard, and Iacopo Carusotto. Quantum vacuum properties of the intersubband cavity polariton field. *Physical Review B*, 72(11):115303, September 2005.

[16] Michael J. Hartmann, Fernando G. S. L. Brandão, and Martin B. Plenio. Strongly interacting polaritons in coupled arrays of cavities. *Nature Physics*, 2(12):849–855, November 2006.

[17] Pg Savvidis, Jj Baumberg, Rm Stevenson, Ms Skolnick, Dm Whittaker, and Js Roberts. Angle-resonant stimulated polariton amplifier. *Physical review letters*, 84(7):1547–50, February 2000.

[18] Jung-Hoon Song, Y. He, a. Nurmikko, J. Tischler, and V. Bulovic. Exciton-polariton dynamics in a transparent organic semiconductor microcavity. *Physical Review B*, 69(23):235330, June 2004.

[19] Taofiq PARAISO. Dynamics of Interactions of Confined Microcavity Polaritons. *Ph.D. Dissertation*, 2010.

[20] G. Bjork and Y. Yamamoto. Analysis of semiconductor microcavity lasers using rate equations. *IEEE Journal of Quantum Electronics*, 27(11):2386–2396, 1991.

[21] G Björk, a Karlsson, and Y Yamamoto. Definition of a laser threshold., August 1994.

[22] Hui Deng, Gregor Weihs, David Snoke, Jacqueline Bloch, and Yoshihisa Yamamoto. Polariton lasing vs. photon lasing in a semiconductor microcavity. *Proceedings of the National Academy of Sciences of the United States of America*, 100(26):15318–23, December 2003.

[23] Guillaume Malpuech, Aldo Di Carlo, Alexey Kavokin, Jeremy J. Baumberg, Marian Zamfirescu, and Paolo Lugli. Room-temperature polariton lasers based on GaN microcavities. *Applied Physics Letters*, 81(3):412, 2002.

[24] S. Christopoulos, G. von Högersthal, a. Grundy, P. Lagoudakis, a. Kavokin, J. Baumberg, G. Christmann, R. Butté, E. Feltin, J.-F. Carlin, and N. Grandjean. Room-Temperature Polariton Lasing in Semiconductor Microcavities. *Physical Review Letters*, 98(12):126405, March 2007.

[25] Gabriel Christmann, Raphael Butte, Eric Feltin, Jean-Francois Carlin, and Nicolas Grandjean. Room temperature polariton lasing in a GaNAlGaN multiple quantum well microcavity. *Applied Physics Letters*, 93(5):051102, 2008.

[26] Ayan Das, Junseok Heo, Marc Jankowski, Wei Guo, Lei Zhang, Hui Deng, and Pallab Bhattacharya. Room Temperature Ultralow Threshold GaN Nanowire Polariton Laser. *Physical Review Letters*, 107(6):066405, August 2011.

[27] Stephen Cohen-Kena, Stephan; Forrest. Room-temperature polariton lasing in an organic single-crystal microcavity. *Nature Photonics*, 4(April):371–375, 2010.

[28] Michael Slootsky, Yifan Zhang, and Stephen R. Forrest. Temperature dependence of polariton lasing in a crystalline anthracene microcavity. *Physical Review B*, 86(4):045312, July 2012.

[29] K S Daskalakis, S a Maier, R Murray, and S Kéna-Cohen. Nonlinear interactions in an organic polariton condensate. *Nature materials*, 13(3):271–8, March 2014.

[30] Christian Schneider, Arash Rahimi-Iman, Na Young Kim, Julian Fischer, Ivan G Savenko, Matthias Amthor, Matthias Lermer, Adriana Wolf, Lukas Worschech, Vladimir D Kulakovskii, Ivan a Shelykh, Martin Kamp, Stephan Reitzenstein, Alfred Forchel, Yoshihisa Yamamoto, and Sven Höfling. An electrically pumped polariton laser. *Nature*, 497(7449):348–52, May 2013.

[31] Pallab Bhattacharya, Bo Xiao, Ayan Das, Sishir Bhowmick, and Junseok Heo. Solid State Electrically Injected Exciton-Polariton Laser. *Physical Review Letters*, 110(20):206403, May 2013.

[32] T. Liew, a. Kavokin, and I. Shelykh. Optical Circuits Based on Polariton Neurons in Semiconductor Microcavities. *Physical Review Letters*, 101(1):016402, July 2008.

[33] Andrew a. Houck, Hakan E. Türeci, and Jens Koch. On-chip quantum simulation with superconducting circuits. *Nature Physics*, 8(4):292–299, April 2012.

[34] Iacopo Carusotto and Cristiano Ciuti. Quantum fluids of light. *Reviews of Modern Physics*, 85(1):299–366, February 2013.

[35] Jonathan Keeling, P. Eastham, M. Szymanska, and P. Littlewood. BCS-BEC crossover in a system of microcavity polaritons. *Physical Review B*, 72(11):115320, September 2005.

[36] Davide Rossini and Rosario Fazio. Mott-Insulating and Glassy Phases of Polaritons in 1D Arrays of Coupled Cavities. *Physical Review Letters*, 99(18):186401, October 2007.

[37] Iulia Buluta and Franco Nori. Quantum simulators. *Science (New York, N.Y.)*, 326(5949):108–11, October 2009.

[38] R. B. Balili, D. W. Snoke, L. Pfeiffer, and K. West. Actively tuned and spatially trapped polaritons. *Applied Physics Letters*, 88(3):031110, 2006.

[39] a. Rahimi-Iman, C. Schneider, J. Fischer, S. Holzinger, M. Amthor, S. Höfling, S. Reitzenstein, L. Worschech, M. Kamp, and a. Forchel. Zeeman splitting and diamagnetic shift of spatially confined quantum-well exciton polaritons in an external magnetic field. *Physical Review B*, 84(16):165325, October 2011.

[40] a. V. Larionov, V. D. Kulakovskii, S. Höfling, C. Schneider, L. Worschech, and a. Forchel. Polarized Nonequilibrium Bose-Einstein Condensates of Spinor Exciton Polaritons in a Magnetic Field. *Physical Review Letters*, 105(25):256401, December 2010.

[41] V. D. Kulakovskii, a. S. Brichkin, S. V. Novikov, C. Schneider, S. Höfling, M. Kamp, a. Forchel, and N. a. Gippius. Magnetic field control of polarized polariton condensates in rectangular microcavity pillars. *Physical Review B*, 85(15):155322, April 2012.

[42] Alex Hayat, Christoph Lange, Lee Rozema, Ardavan Darabi, Henry van Driel, Aephraim Steinberg, Bryan Nelsen, David Snoke, Loren Pfeiffer, and Kenneth West. Dynamic Stark Effect in Strongly Coupled Microcavity Exciton Polaritons. *Physical Review Letters*, 109(3):1–5, July 2012.

[43] Georgios Roumpos, Wolfgang H. Nitsche, Sven Höfling, Alfred Forchel, and Yoshihisa Yamamoto. Gain-Induced Trapping of Microcavity Exciton Polariton Condensates. *Physical Review Letters*, 104(12):126403, March 2010.

[44] G. Tosi, G. Christmann, N. G. Berloff, P. Tsotsis, T. Gao, Z. Hatzopoulos, P. G. Savvidis, and J. J. Baumberg. Sculpting oscillators with light within a nonlinear quantum fluid. *Nature Physics*, 8(2):1–5, January 2012.

[45] P. Cristofolini, a. Dreismann, G. Christmann, G. Franchetti, N. G. Berloff, P. Tsotsis, Z. Hatzopoulos, P. G. Savvidis, and J. J. Baumberg. Optical Superfluid Phase Transitions and Trapping of Polariton Condensates. *Physical Review Letters*, 110(18):186403, May 2013.

[46] C W Lai, N Y Kim, S Utsunomiya, G Roumpos, H Deng, M D Fraser, T Byrnes, P Recher, N Kumada, T Fujisawa, and Y Yamamoto. Coherent zero-state and pi-state in an exciton-polariton condensate array. *Nature*, 450(7169):529–32, November 2007.

[47] Na Young Kim, Kenichiro Kusudo, Congjun Wu, Naoyuki Masumoto, Andreas Löffler, Sven Höfling, Norio Kumada, Lukas Worschech, Alfred Forchel, and Yoshihisa Yamamoto. Dynamical d-wave condensation of excitonpolaritons in a two-dimensional square-lattice potential. *Nature Physics*, 7(9):681–686, June 2011.

[48] N Y Kim, K Kusudo, a Löffler, S Höfling, a Forchel, and Y Yamamoto. Excitonpolariton condensates near the Dirac point in a triangular lattice. *New Journal of Physics*, 15(3):035032, March 2013.

[49] Na Young Kim, Kenichiro Kusudo, Andreas Löffler, Sven Höfling, Alfred Forchel, and Yoshihisa Yamamoto. ¡Span Class="Aps-Inline-Formula"¿¡Math¿¡Mi¿F¡/Mi¿¡/Math¿¡/Span¿-Band Condensates in Exciton-Polariton Lattice Systems. *Physical Review B*, 89(8):085306, February 2014.

[50] a. Baas, O. El Daïf, M. Richard, J.-P. Brantut, G. Nardin, R. Idrissi Kaitouni, T. Guillet, V. Savona, J. L. Staehli, F. Morier-Genoud, and B. Deveaud. Zero dimensional exciton-polaritons. *Physica Status Solidi (B)*, 243(10):2311–2316, August 2006.

[51] O. El Daif, a. Baas, T. Guillet, J.-P. Brantut, R. Idrissi Kaitouni, J. L. Staehli, F. Morier-Genoud, and B. Deveaud. Polariton quantum boxes in semiconductor microcavities. *Applied Physics Letters*, 88(6):061105, 2006.

[52] Daniele Bajoni, Pascale Senellart, Esther Wertz, Isabelle Sagnes, Audrey Miard, Aristide Lemaître, and Jacqueline Bloch. Polariton Laser Using Single Micropillar GaAs-GaAlAs Semiconductor Cavities. *Physical Review Letters*, 100(4):1–4, January 2008.

[53] Lydie Ferrier, Esther Wertz, Robert Johne, Dmitry Solnyshkov, Pascale Senellart, Isabelle Sagnes, Aristide Lemaître, Guillaume Malpuech, and Jacqueline Bloch. Interactions in Confined Polariton Condensates. *Physical Review Letters*, 106(12):1–4, March 2011.

[54] Marta Galbiati, Lydie Ferrier, Dmitry Solnyshkov, Dimitrii Tanese, Esther Wertz, Alberto Amo, Marco Abbarchi, Pascale Senellart, Isabelle Sagnes, Aristide Lemaître, Elisabeth Galopin, Guillaume Malpuech, and Jacqueline Bloch. Polariton Condensation in Photonic Molecules. *Physical Review Letters*, 108(12):1–5, March 2012.

[55] E. Wertz, L. Ferrier, D. D. Solnyshkov, R. Johne, D. Sanvitto, a. Lemaître, I. Sagnes, R. Grousson, a. V. Kavokin, P. Senellart, G. Malpuech, and J. Bloch. Spontaneous formation and optical manipulation of extended polariton condensates. *Nature Physics*, 6(11):860–864, August 2010.

[56] T. Jacqmin, I. Carusotto, I. Sagnes, M. Abbarchi, D.D. Solnyshkov, G. Malpuech, E. Galopin, a. Lemaître, J. Bloch, and a. Amo. Direct Observation of Dirac Cones and a Flatband in a Honeycomb Lattice for Polaritons. *Physical Review Letters*, 112(11):116402, March 2014.

[57] Michael C.Y. Huang, Y. Zhou, and Connie J. Chang-Hasnain. A surface-emitting laser incorporating a high-index-contrast subwavelength grating. *Nature Photonics*, 1(2):119–122, February 2007.

[58] Michael C. Y. Huang, Ye Zhou, and Connie J. Chang-Hasnain. A nanoelectromechanical tunable laser. *Nature Photonics*, 2(3):180–184, February 2008.

[59] Robert Magnusson and Mehrdad Shokooh-Saremi. Physical basis for wideband resonant reflectors. *Optics express*, 16(5):3456–62, March 2008.

[60] Ye Zhou, Michael Moewe, Johannes Kern, Michael C. Huang, and Connie J. Chang-Hasnain. Surface-normal emission of a high-Q resonator using a subwavelength high-contrast grating. *Optics Express*, 16(22):17282, October 2008.

[61] Vadim Karagodsky, Forrest G Sedgwick, and Connie J Chang-Hasnain. Theoretical analysis of subwavelength high contrast grating reflectors. *Optics express*, 18(16):16973–88, August 2010.

[62] Christopher Chase, Yi Rao, Werner Hofmann, and Connie J Chang-hasnain. 1550 nm high contrast grating VCSEL. 7615(15):15461–15466, 2010.

[63] Bo Zhang, Zhaorong Wang, Sebastian Brodbeck, Christian Schneider, Martin Kamp, Sven Höfling, and Hui Deng. Zero-dimensional polariton laser in a subwavelength grating-based vertical microcavity. *Light: Science & Applications*, 3(1):e135, January 2014.

[64] J. Fischer, S. Brodbeck, B. Zhang, Z. Wang, L. Worschech, H. Deng, M. Kamp, C. Schneider, and S. Höfling. Magneto-exciton-polariton condensation in a sub-wavelength high contrast grating based vertical microcavity. *Applied Physics Letters*, 104(9):091117, March 2014.

[65] Zhaorong Wang, Bo Zhang, and Hui Deng. Engineering Dispersion Relation of Photons in Vertical Cavity using High-Contrast Gratings. *CLEO: 2014, OSA Technical Digest, (Optical Society of America, 2014), paper STu2O.6.*, (1):2–3, 2014.

[66] O. Kyriienko, E. a. Ostrovskaya, O. a. Egorov, I. a. Shelykh, and T. C. H. Liew. Bistability in microcavities with incoherent optical or electrical excitation. *Physical Review B*, 90(12):125407, September 2014.

[67] a. Amo, T. C. H. Liew, C. Adrados, R. Houdré, E. Giacobino, a. V. Kavokin, and a. Bramati. Excitonpolariton spin switches. *Nature Photonics*, 4(6):361–366, April 2010.

[68] H. Rahimpour Soleimani, S. Cronenberger, O. Cregut, J.-P. Likforman, M. Gallart, T. Ostatnicky, P. Gilliot, and B. Honerlage. Study of exciton-polariton spin dynamics. *Applied Physics Letters*, 85(22):5263, 2004.

[69] I. a. Shelykh, R. Johne, D. D. Solnyshkov, and G. Malpuech. Optically and electrically controlled polariton spin transistor. *Physical Review B*, 82(15):153303, October 2010.

[70] a. Larionov, V. Kulakovskii, S. Höfling, C. Schneider, L. Worschech, and a. Forchel. Polarized Nonequilibrium Bose-Einstein Condensates of Spinor Exciton Polaritons in a Magnetic Field. *Physical Review Letters*, 105(25):1–4, December 2010.

[71] O. Kyriienko, T.C.H. Liew, and I.a. Shelykh. Optomechanics with Cavity Polaritons: Dissipative Coupling and Unconventional Bistability. *Physical Review Letters*, 112(7):076402, February 2014.

[72] Charles Kittel. *Introduction to solid state physics*. 2005.

[73] C Weisbuch, M Nishioka, a Ishikawa, and Y Arakawa. Observation of the coupled exciton-photon mode splitting in a semiconductor quantum microcavity., December 1992.

[74] S M Sze. *Semiconductor Devices: Physics and Technology*. 2006.

[75] M. de Lima, M. van der Poel, P. Santos, and J. Hvam. Phonon-Induced Polariton Superlattices. *Physical Review Letters*, 97(4):045501, July 2006.

[76] K. Winkler, C. Schneider, J. Fischer, A. Rahimi-Iman, M. Amthor, A. Forchel, S. Reitzenstein, S. Hofling, and M. Kamp. Electroluminescence from spatially confined exciton polaritons in a textured microcavity. *Applied Physics Letters*, 102(4):041101, 2013.

[77] a. S. Brichkin, S. I. Novikov, a. V. Larionov, V. D. Kulakovskii, M. M. Glazov, C. Schneider, S. Höfling, M. Kamp, and a. Forchel. Effect of Coulomb interaction on exciton-polariton condensates in GaAs pillar microcavities. *Physical Review B*, 84(19):195301, November 2011.

[78] T. C. H. Liew, a. V. Kavokin, T. Ostatnický, M. Kaliteevski, I. a. Shelykh, and R. a. Abram. Exciton-polariton integrated circuits. *Physical Review B*, 82(3):033302, July 2010.